Application of 3D seismics to enhance mapping of potholes in the western Bushveld Complex, South Africa

By

Lebogang Tshepiso Charmaine Sehoole

Supervisor(s):

Prof Musa Manzi and Dr Steve Ergong Zhang

A thesis submitted to the

Faculty of Science, University of the Witwatersrand

in fulfilment of the requirements for the degree of

Master of Science

School of Geosciences

University of the Witwatersrand

Johannesburg, 2019

Declaration

I declare that this dissertation is my own, unaided work. It is being submitted for the Degree of Master of Science at the University of the Witwatersrand, Johannesburg. It has not been submitted before for any degree or examination in any other University.

_____

Lebogang Tshepiso Charmaine Sehoole

24th day of **July** 20**19**, at **The University of the Witwatersrand, Johannesburg.**

Abstract

The ~2.06 Ga Bushveld Complex in South Africa is widely known as the world's largest layered igneous intrusion. The Bushveld Complex hosts the world's largest platinum and chromium deposits. The two of the major economic platinum-bearing ore bodies (known as reefs) are the Merensky and the Upper Group-2 (UG-2) reefs, which are located at depths between 500 m and 1.5 km below surface. Mining operations on these horizons are often complicated by the presence of geological features such as faults, dykes, potholes and iron-rich ultramafic pegmatite (IRUP) bodies. This emphasises the importance of characterising these features and predicting their occurrence.

In this study, the 3D reflection seismic method is employed to delineate these structures (mainly potholes) within the Western Bushveld Complex, South Africa. Potholes are slump structures that disturb mining processes and ultimately decrease the mining productivity. Various state-of-the-art techniques were used to identify and analyse potholes, including (i) horizon-based seismic attributes, (ii) complex-trace attributes, (iii) 3D volumetric attributes, (iv) difference-of-two-surfaces, and (v) geostatistical methods. The seismic techniques complimented each other in detecting and identifying approximately 43 potholes, which were then used for geostatistical analysis. The results suggest that pothole structures are asymmetric and are often associated with faults. This study also reveals that a majority of the potholes imaged in the seismic data have propagated between the Merensky Reef and the UG-2 levels, i.e., MR and UG-2 are affected by the same potholes. These potholes are randomly distributed and exhibit some clustering. A k-mean cluster analysis was implemented and revealed two clusters that are present in the study area. The various hypotheses on the formation of potholes are investigated. This study rules out some of the hypotheses for the formation of potholes and

proposed that the potholes might have formed from multiple mechanisms as opposed to just one. Statistical analyses suggest a positive linear relationship between the pothole depth and the pothole diameter, indicating that the pothole may have grown in width and depth at the same time.

Acknowledgements

To God Almighty, thank you so much for carrying me to the finish line and the strength to carry on when I didn't think I had it in me.

I would like to thank my supervisors, Dr. Musa Manzi and Dr Steve Ergong Zhang, for their support, guidance and willingness to review my work and provide me with feedback. I would also like to thank Dr. Stephanie Enslin-Scheiber; your input was invaluable. An extra thank you to Musa Manzi for always going beyond his call of duty to make sure I was physically, emotionally and mentally healthy.

I wish to express my appreciation to Lonmin Platinum for availing the 3D seismic data in the Western Bushveld. Many thanks to DUG Insight seismic and geological interpretation software as well as Schlumberger for granting licences for Petrel, a seismic interpretation and modelling software. I would also like to thank the Wits Seismic Research Centre, funded by Shell SA Ltd. and CGG, for providing research facilities to conduct my research.

I would like to acknowledge and express my greatest appreciation towards the financial support I received throughout my MSc. This includes SVK Education Trust and CIMERA (Centre of Excellence for Integrated Mineral and Energy Resource Analysis).

To my family, thank you for always encouraging me and showing interest in the progress of the project. I kept me on my toes and pushing to get my work done. I would like to thank my friends Shalene Selkirk, Tamara Makhateng, the "Gents", for providing me with much needed breaks during my most stressful times, and for always encouraging and motivating me to finish my degree. A very big thank

you to my friend Vuyolwethu Mahlalela for always being a phone call away and eager to help me with anything and everything, you truly are very special to me.

Last but definitely not least, I wish to convey my heart-felt gratitude towards my life partner Siyabonga Nkabinde. This MSc is as a result of his continued patience, love and encouragement. Thank you so much for your support.

Table of Contents

List of Figures

List of Tables

1 INTRODUCTION

The Bushveld Complex, located in the northern part of South Africa, is widely known as the world's largest layered igneous intrusion (McCarthy and Rubidge, 2005). The ~2.06 Ga Bushveld Complex hosts the world's largest platinum and chromium deposits (Free, 2001; McCarthy and Rubidge, 2005). The platinum is associated with the sequence of rocks known as the Rustenberg Layered Suite with the bulk of the deposits hosted within the Critical Zone. This principally comprises orthopyroxenites and chromitites within the Lower Critical Zone with the appearance of norites and anorthosites within the Upper Critical Zone. The economic resources, platinum-group elements (PGEs) are found in stratiform horizons, locally referred to as 'reefs'. The Merensky Reef (MR) and the Upper Group-2 (UG-2) are two of the major economic platinum-bearing horizons of the Bushveld Complex.

The extraction of minerals from these horizons at great depths (~0.5-2.0 km) is complicated by the presence of geological features such as faults, dykes, potholes and iron-rich ultramafic pegmatite (IRUP) bodies. This emphasises the importance of characterising these features and predicting their occurrence. The success of reflection seismic method in the Witwatersrand Basin in imaging deep seated gold-bearing horizons in the 1990s gave anticipation that the same success could be achieved in the Bushveld Complex in mapping platinum horizons and delineating the obstructing geological features (Campbell, 1990; Durrheim and Maccelari, 1991; Odgers et al., 1993; Campbell, 1994; Davison and Chunnett, 1999; Stevenson et al., 2003). The main objective of this study is to use 3D seismic reflection method and 3D seismic attributes to delineate these geological features with emphasis on pothole structures.

In the early 1980s Anglo American successfully conducted high-resolution 2D reflection seismic surveys in the Bushveld Complex for deep crustal studies and mine planning and designs. The surveys revealed that: (i) the granites of the Lebowa Granite Suite are "seismically transparent"; (ii) the upper zone is layered in a recurring manner; (iii) the main zone has lower amplitude reflectors; (iv) the critical zone has higher amplitude, layered reflectors; (Trickett et al., 2009). Between 1985 and 1986, Northam Platinum Mine conducted a 2D reflection seismic survey in the north-western limb of the Bushveld Complex and the results showed that the seismic reflection method could be used to map different reef facies, the extent of potholes, and chaotic seismic reflections within the seismic section if correct acquisition parameters are used (Miningtek CSIR, 1997; Stevenson et al., 2003; Trickett et al., 2009).

In 1993, Lonmin Platinum Mine conducted their first ever high-resolution 3D reflection seismic survey covering its Karee Mine. This survey was followed by the 2008 Lonmin 3D seismic survey, which overlapped with the 1999 3D seismic survey. The 2008 3D seismic data were interpreted by Trickett et al. (2009) and their results showed high and continuous reflections at the UG-2 interface and the IRUPs (Trickett et al., 2009) (Figure 1.1) The potholes are recognised by a change of dips along the seismic horizons and IRUPs are seen as slumps in the seismic section associated with low amplitude reflections (Figure 1.1).

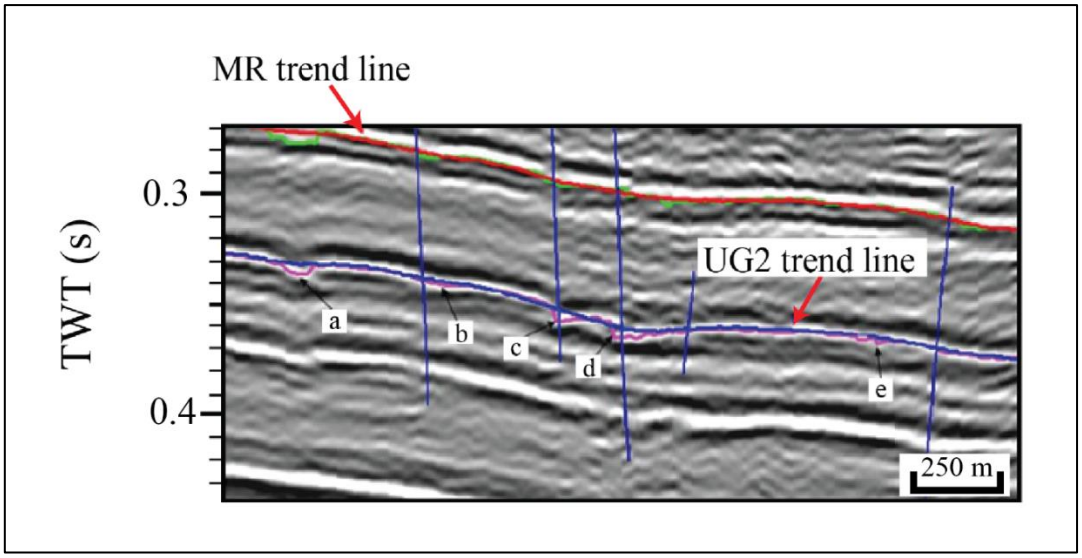

Figure 1.1. *Seismic section extracted from the Lonmin 2008 3D seismic survey. Section identifies slump structures (a to e) within the UG-2. Navy line shows trend line of UG-2 horizon, pink line indicates residual and potholes. Merensky Reef (MR) trend line is shown in red and green shows the slump structures (modified from Trickett et al., 2009).*

Potholes and IRUP bodies are the least understood geological features found in the Bushveld Complex as their origins and distributions are unknown. Trickett et al. (2009) showed that IRUP bodies and potholes were responsible for ~ 15% losses when extracting minerals within the target bodies of the Western Bushveld. The IRUP bodies and potholes are thought to exist as clusters that have a lateral variation in size, from metres to hundreds of meters (Trickett et al., 2009). Campbell (2011) and Trickett (2009) suggested that IRUP bodies and potholes are often related.

1.1 AIMS AND OBJECTIVES

The project aims to identify potholes within the Western Limb of the Bushveld Complex, investigate the spatial distribution, and development of potholes using 3D reflection seismic data sourced from Lonmin Platinum, which were acquired and processed in 1993 by Compagnie Générale de Géophysique (CGG). The primary goal of the 1993 3D seismic survey

was to image the Merenskey Reef (MR) and UG-2 Chromitite Reef (UG-2) and their associated potholes at depths greater than 500 m below surface.

Our detailed objectives are to:

(i) Locate the UG-2 and Merensky Reef (MR) horizons, faults and potholes.

(ii) Determine the smallest pothole size that can be detected and resolved within the Lonmin 3D seismic data.

(iii) Determine the lateral resolution limit between adjacent potholes that can be detected within the data.

(iv) Statistically analyse the correlation between the size and distribution of potholes.

(v) Examine possible relationships between potholes and other geological features (e.g. faults) to hypothesize on the formation mechanism(s) of potholes.

1.2 HYPOTHESIS

The potholes are likely to be found in faulted areas. The spatial distribution of the potholes will show that the smaller potholes are clustered near each other while the larger potholes are more isolated in relation to other potholes.

1.3 LOCATION OF STUDY AREA

The study area (Figure 1.2) is in the Western Limb of the Bushveld Complex (UTM coordinates, Zone 35 S: 554338.26 mE; 7161300.93 mN) near Rustenburg, 100 km north of Johannesburg. The study area is approximately 67.84 km^2.

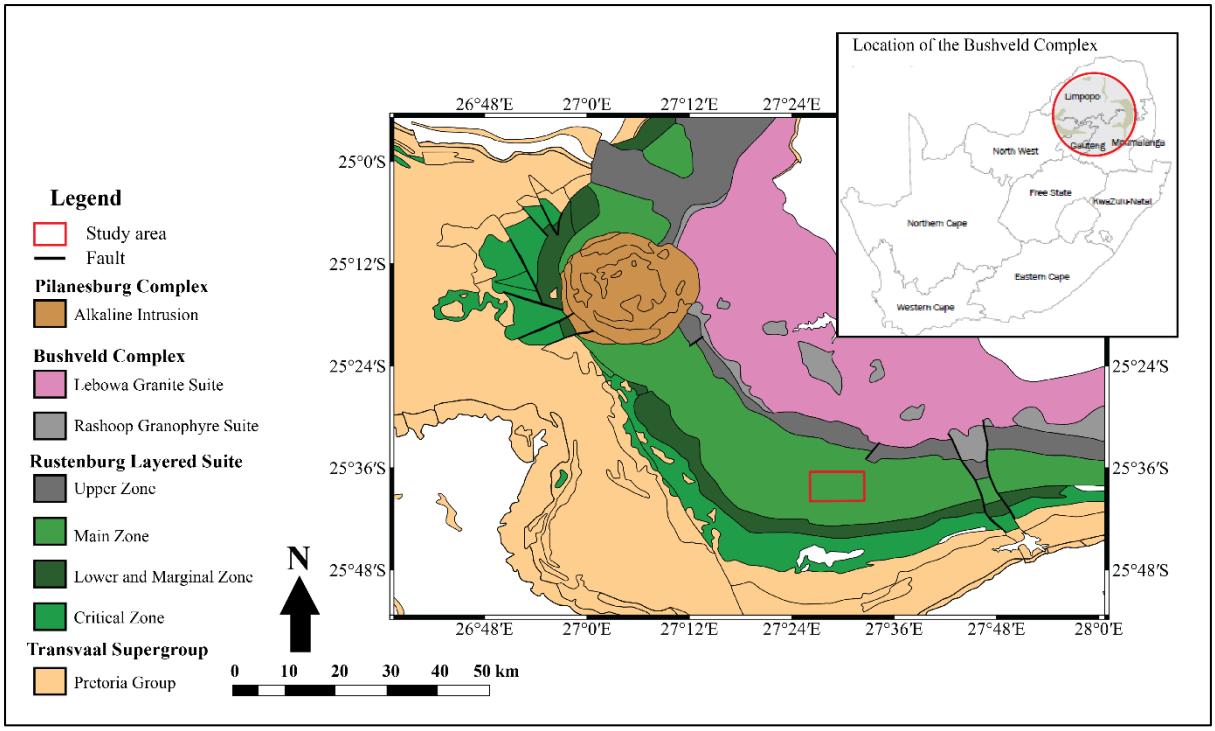

Figure 1.2. *Simplified geological map of the Western Limb Bushveld with the study area marked in red (modified from SACS 1980).*

2 GEOLOGICAL BACKGROUND

2.1 BUSHVELD COMPLEX

The Palaeoproterozoic (2.5 – 1.6 Ga) Bushveld Complex is of great interest to scientists and explorationists due to its rich ore deposits of platinum, palladium, rhodium, chromium and vanadium (Kinnaird, 2005; McCarthy and Rubidge, 2005; Hunt, 2006; Cawthorn, 2010). The Bushveld Complex is composed of four limbs, the northern, eastern, western and southern limbs, which occupy a total surface area of about 65 000 km^2 (Hunter, 1978; Uken, 1998; Hunt, 2006). The eastern limb extends from Marble hall to Lydenburg and the western limb extends from Warmbaths to Zeerust. While the northern limb is located in Mokopane (Potgietersrus) and the southern limb extends from Groblersdal to Bethal. Since the southern limb of the Bushveld Complex does not outcrop anywhere, the lateral extent of its limb was determined using borehole and gravity data (Hunt, 2006).

The Bushveld Complex is divided into three major plutonic suites: The Rashoop granophyre suite; the Rustenburg layered suite; the Lebowa granite suite (SACS, 1980; Uken, 1998; Hunt, 2006; Lenhardt and Eriksson, 2012) and a 'roof' (the Rooiberg Group) of the major plutonic suites.

2.1.1 Rooiberg Group

The Rooiberg Group is a ~3 km thick lava succession, consisting of rhyolite, dacite, basaltic andesite and tuff (with the presence of minor shales and greywacke) (Lenhardt and Eriksson, 2012). The Rooiberg Group is a volcanic succession that was formed by the deposition of two distinct volcanic lava episodes ~2.061 Ga (Walraven 1987; Harmer and Armstrong, 2000; Kinnaird, 2005). The volcanic lavas that characterised the first episode were basaltic, while the volcanic lavas of the second episode were predominantly rhyolitic. The rhyolitic lavas of the

second episode were more extensive and thicker than the basaltic lavas of the first episode (McCarthy and Rubidge, 2005). The Rooiberg Group unconformably overlies the Transvaal Supergroup (Cheney and Twist, 1991; Kinnaird, 2005). The group is associated with four formations; the Dullstroom, Damwal, Kwaggasnek and Schrikkloof Formations, with the Dullstroom Formation at the bottom and the Schrikkloof at the top (Uken 1998; Kinnaird, 2005; Lenhardt and Eriksson, 2012). Continued magmatic activity led to the deposition of the Rustenburg Layered Suite of the tripartite Bushveld Complex, which disturbed the setting of the Rooiberg Group. The deposition of the Rustenburg Layered Suite caused the separation of the Dullstroom Formation from the rest of the formations of the Rooiberg Group, allowing the formations to act as the roof of the Bushveld Complex (Kinnaird, 2005; Hunt, 2006; Lenhardt and Eriksson, 2012).

2.1.2 Rashoop Granophyre Suite

The Rashoop Granophyre Suite exists between the Rustenburg Layered Suite and the lower Rooiberg Group as an intrusive sheet (Kinnaird, 2005). The suite is granitic in composition and is thought to have formed due to partial melting of the lower crust (Walraven, 1982; Hunt, 2006). The Rashoop Granophyre Suite can be divided into three units according to their texture: the Stavoren Granophyre, the Zwartbank Pseudogranophyre, and the Rooi Granite Porphyry (SACS, 1980; Hunt, 2006).

2.1.3 Rustenburg Layered Suite

The Rustenburg Layered Suite (Figure 2.1) is located between the Rooiberg felsite and the Rashoop Granophyre Suite as sills within the Transvaal Supergroup (Kinnaird, 2005). It is best exposed in the eastern limb of the Bushveld Complex (Von Gruenewaldt et al., 1985). The Layered Suite is subdivided into the upper, main, critical, lower and marginal zone (Uken, 1998; Kinnaird, 2005; Hunt, 2006).

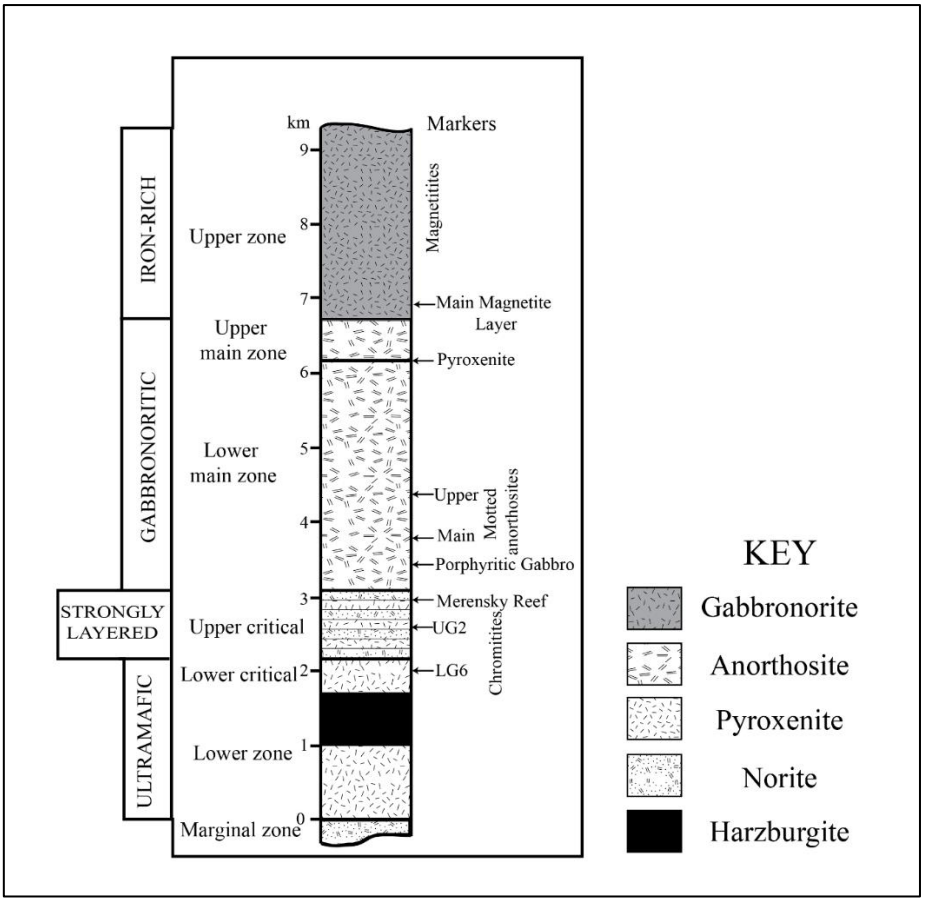

Figure 2.1. *Vertical section of the Rustenburg layered suite from the eastern limb of the Bushveld Complex showing the main zones. On the left of the stratigraphic column is the main geology make-up of the specific layer and on the right the arrows show the marker layers (modified from Mitchell and Scoon, 2007).*

Lower and Marginal Zone

The lower zone, best exposed in the Olifants River trough of the north-eastern Bushveld, consists of alternating layers of bronzitite, harzburgite and dunite (Von Gruenewaldt et al., 1985; Uken, 1998; Kinnaird, 2005; Hunt, 2006). The zone reaches a thickness of about 1.3 km in some areas of the Bushveld Complex and can be subdivided into three pyroxenite zones: the top zone, middle zone and bottom zone. The top and bottom zones consist mainly of pyroxenite and the middle zone consist mainly of harzburgite (Cawthorn et al., 2002; Kinnaird, 2005).

The Marginal zone is not a continuous zone along the Bushveld Complex, however where present, its thickness can vary from zero to hundreds of metres (Kinnaird, 2005). The marginal zone comprises the norites, pyroxenites, and ultramafic rocks, all of which are fine-grained and vary in texture (Uken, 1998; Kinnaird, 2005).

Critical Zone

The critical zone, located above the lower zone, hosts the largest concentration of platinum group elements (PGEs) (Schouwstra and Kinloch, 2000). This zone is characterised by a prominent layering of PGEs deposits. The critical zone, ~1.5 km thickness, is present in both the eastern and western limbs of the Bushveld Complex (Kinnaird, 2005; Hunt, 2006). This zone can be further divided into the lower group that consists of feldspathic pyroxenite and the upper group comprising norites, leuconorites, and anorthosites (Uken, 1998; Kinnaird, 2005). The Merensky Reef, which hosts most of the PGEs mineralization, terminates the critical zone and acts as a boundary between the critical and main zone (Kinnaird, 2005; Hunt, 2006). The critical zone is of utmost importance to this project because it is a layer that is associated with strong continuous seismic reflection. The strong reflections are a result of the alternating layering of the pyroxenite and anthorthosite layers present in the zone. The significant contrast in acoustic impedance (product of seismic velocity and bulk density) is mainly caused by the variation in densities of the two rock layers. This is an indicator of the potential success in using the seismic reflection method to identify the platinum-bearing horizons in the Bushveld Complex.

Main Zone

The main zone has a thickness greater than 3 km and it comprises gabbronorite with some anorthosite and pyroxenite bands (Uken 1998; Kinnaird, 2005). The zone has moderate layering that is considered to have formed from the re-distribution of crystals in the magma

chamber during solidification process of the emplaced magma (Kinnaird, 2005). The layered sequences are continuous along strike for about 80 km in the eastern Bushveld Complex and approximately 20 km in the western Bushveld Complex.

Upper Zone

The upper zone hosts 25 magnetite layers in the eastern limb of the Bushveld Complex that are classified into four groups (Kinnaird, 2005; Hunt, 2006). The zone is banded and dominated by gabbros. The ~2 m thick magnetite layer, located near the base of the upper zone, is a source of most of the vanadium ore that is mined in South Africa (Kinnaird, 2005).

2.1.4 Lebowa Granite Suite

The Lebowa Granite Suite is a 1.5 to 3.5 km thick igneous intrusion that intruded between the Rooiberg Group and the Rashoop Granophyre Suite as sheets (Kinnaird, 2005; Hunt, 2006). The granites were then cooled as they encountered the granophyre, as indicated by the presence of the zone of quartz-feldspar pegmatite (Hunt, 2006). The suite can be divided into seven facies that are identified by colour, texture and grain size (Kinnaird, 2005). The main granites of the suite are high in potassium and contain magnetite (Hunt, 2006).

3 SEISMOLOGY

3.1 BACKGROUND

The first active seismic experiments were conducted by Robert Mallet in 1857 while he was studying the damage caused by an earthquake near Naples. Robert Mallet experimented with artificial earthquakes to measure the time of transmission of seismic waves generated by an explosion. From this experiment he concluded that the seismic waves generated by earthquakes radiate from a central focus. He further postulated that the epicentre of earthquakes can be located by projecting these waves backwards towards the source and that observatories could be built to monitor earthquakes' activity (Shearer, 2009). However, it was in the 1900s that B.B. Galitzen created a seismograph that made use of a moving pendulum to generate an electric current in a coil; a method that is still in use today (Shearer, 2009). In the same year R. Oldham identified that there were compressional (P-), shear (S-), and surface waves in the earthquake records (Shearer, 2009).

In the 1920s, the seismic reflection method using an artificial source (e.g. explosions) was first developed for the 'soft' rock environment to explore for oil and gas in the shallow crust (Shearer, 2009). However, today the seismic method is also used in the 'hard' rock environments to explore for deep seated minerals (e.g. Milkereit et al., 1996, 2000; Pretorius et al., 2000; Trickett et al., 2004; Malehmir and Bellefleur, 2009; Malehmir et al., 2012).

Types of seismic waves

Seismic waves can be classified into two main groups of elastic waves with the first group consisting of waves that propagate within the rock that are called body waves (Durrheim and Linzer, 2014). There are two types of body waves, primary waves (P-waves) that move in a compressional motion like sound waves (Shearer, 2010) (Figure 3.1a) and secondary waves

(S-waves) that are also known as shear waves. In any given media, shear waves are often slower than P-waves and the media moves in a transverse motion to the direction of propagation (Schuster, 2007) (Figure 3.1b). S-waves can only travel through solids and often have more energy than P-waves.

The second group of waves are surface waves; these waves are restricted to the boundary between air and rock on the surface. Surface waves are divided into two subgroups, Rayleigh waves and Love waves (Schuster, 2007). Rayleigh waves propagate through a medium in an elliptical motion with neither transverse nor perpendicular motion but more like the motion of surface ocean waves (Durrheim and Linzer, 2014) (Figure 3.2a). Love waves, on the other hand, occur when horizontally polarised S-waves are trapped in the low-velocity zone on the surface (Durrheim and Linzer, 2014) (Figure 3.2b).

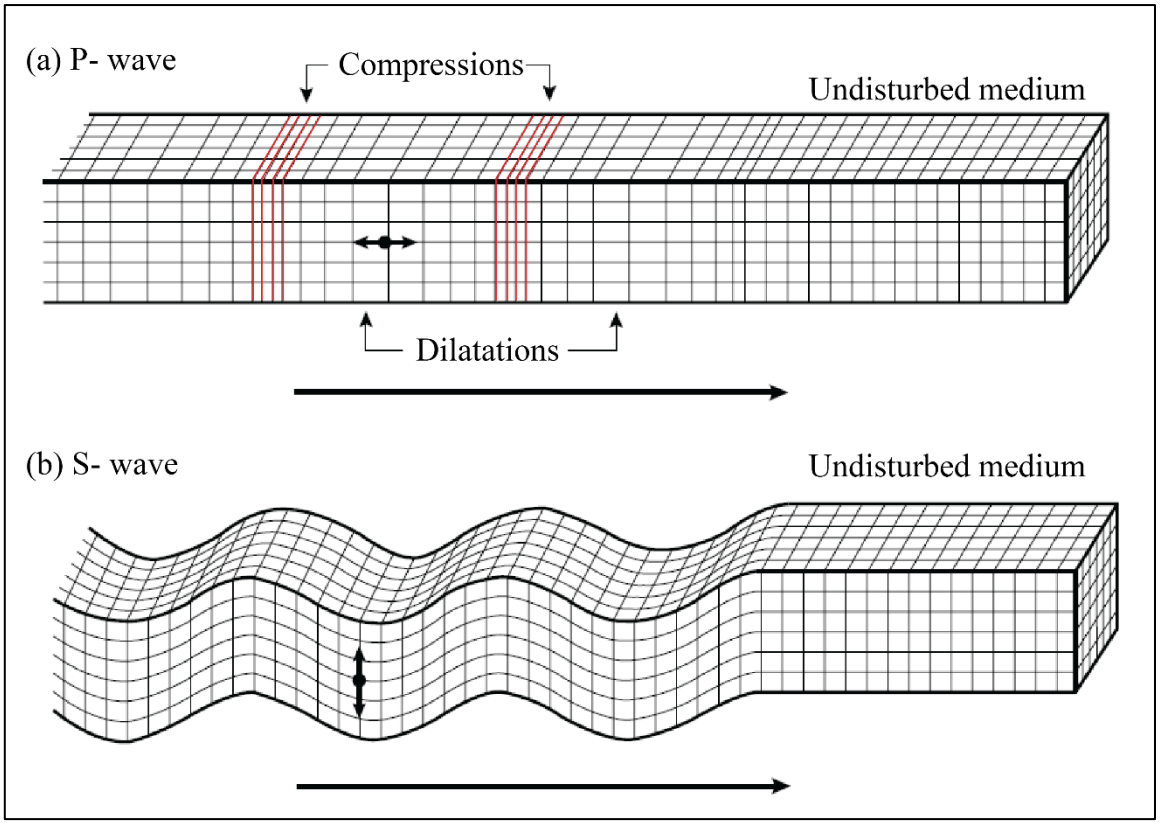

Figure 3.1. *Diagram illustrating Body waves. (a) P-wave motion and (b) S-wave motion (modified from Bolt, 1982; Kearey et al., 2002).*

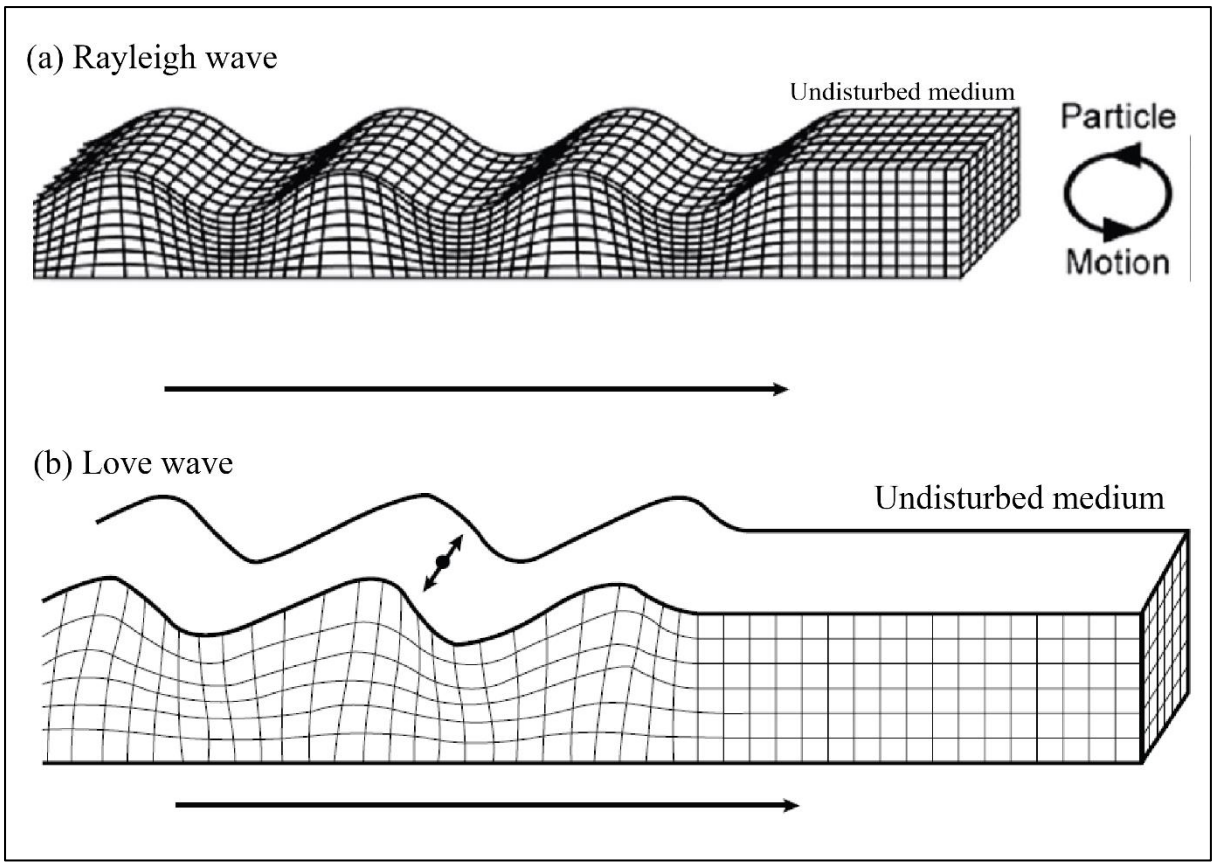

***Figure 3.2**. Diagram illustrating Surface waves. (a) Rayleigh wave motion and (b) Love wave motion (modified from Bolt, 1982; Kearey et al., 2002; Quora, 2018).*

The properties of rocks, such as the bulk density and elasticity, control the velocities of P-waves and S-waves (Durrheim and Linzer, 2014). Mathematically, the P-wave and S-wave velocities are given by:

$$V_p = \sqrt{\frac{K+\frac{4}{3}\mu}{\rho}} \quad (1)$$

and,

$$V_s = \sqrt{\frac{\mu}{\rho}} \quad (2)$$

where V_p is the P-wave velocity, V_s is the S-wave velocity, K is the bulk modulus (the incompressibility of a material), ρ is the bulk density of the rock mass and μ the shear (or rigidity) modulus (Shearer, 2010).

3.2 ACQUISITION

In seismic exploration, a seismic wave is an acoustic wave in the ground, produced by an energy source that physically perturbs the ground (e.g. dynamite, sledgehammer, and vibroseis). The seismic reflection method deals with the physical protuberances that arrive after the initial ground motion. The seismic reflection method (Figure 3.3) involves analysing the elastic waves reflected off the subsurface layers (Burger, 1992) and determining information about the subsurface from the amplitude and the shape of the wave. When a seismic wave reaches the boundary between two materials, such as two different types of rocks with different acoustic impedances z_1 and z_2 (see equation 3), some of its energy gets reflected towards the ground surface where it is recorded. Mathematically, the acoustic impedance is given by:

$$z = v\rho, \tag{3}$$

where v is the seismic velocity and ρ is the bulk density (Kearey et al., 2002). The ratio of the amplitude of the displacement of a reflected wave to that of the incident wave is termed the Reflection coefficient (R). The Reflection coefficient can be derived from the acoustic impedance and is given by:

$$R = \frac{Z_2 - Z_1}{Z_2 + Z_1} \tag{4}$$

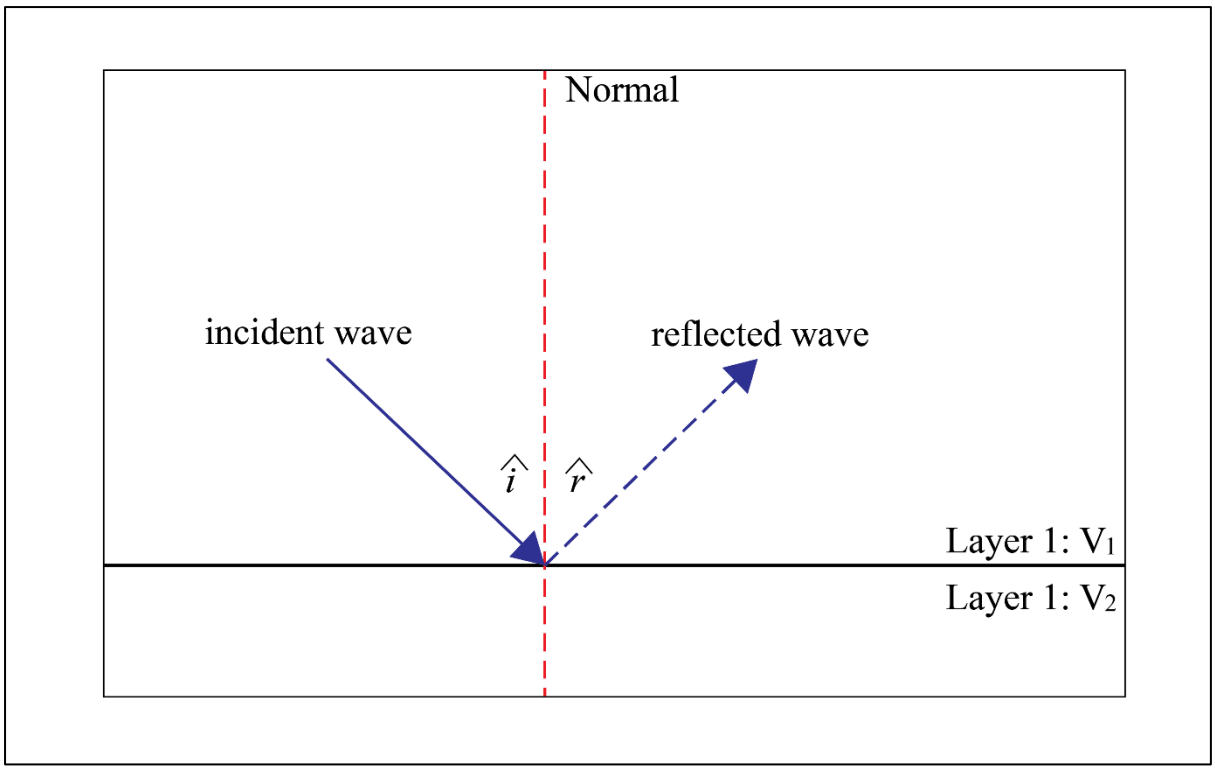

***Figure 3.3**. Diagram illustrating an incident wave that is being reflected at the boundary where the angle $\hat{\imath} = \hat{r}$(modified from Kearney et al., 2002).*

In this study, there are two significant economic horizons that are delineated using the 3D seismic method; these are the Merensky Reef (MR) and Upper Group 2 (UG-2) horizons (Figure 1.1). The MR is indirectly imaged by the seismic method because of the low acoustic impedance contrast between the hanging wall anorthosite (bulk density of 2.75 g/cm^3 and P-wave velocity ranging from 6500 m/s to 7000 m/s giving an acoustic impedance range of 17875 to 19250), and the pyroxenites (density of 3.15 g/cm^3 and P-wave velocity ranging from 6500 m/s to 7000 m/s giving an acoustic impedance range of 20475 to 22050) (Campbell, 2011). The UG-2, on the other hand, is seismically imaged due to a major acoustic impedance between the dense chromitite (bulk density of 4.8 g/cm^3 and P-wave velocity ranging from 6500 m/s to 7000 m/s giving an acoustic impedance range of 31200 to 33600) and the less dense norite or anorthosite (density of 2.9 g/cm^3 and P-wave velocity ranging from 6500 m/s to 7000 m/s giving an acoustic impedance range of 18850 to 20300). Therefore, the large acoustic

impedance contrast is controlled by the bulk density variations within the target strata, rather than by seismic velocity, as the seismic velocities do not vary significantly. The 3D seismic data covering the Lonmin platinum mine were acquired and processed in 1993 by Compagnie Générale de Géophysique (CGG). There is limited information available on the observer's reports on the acquisition and processing workflow conducted by CGG, and, thus, this thesis doesn't provide the full details. A few of the parameters are summarised by Larroque et al. (2002).

Aspects of the seismic design that were appropriate for assessing the resolution at primary target depths include the source and receiver line increments (SLI, RLI); source and receiver station intervals (SI, RI) along acquisition lines; source and receiver arrays; and a dominant frequency. Although a detailed description of the survey parameters is beyond the scope of this thesis, the following parameters are relevant for the resolution of the legacy data: The dense acquisition (SLI: 150 m, SI: 15 m, RLI: 120 m, RI: 7 m, sweep frequency: 24s, 10-160 Hz) using the Sercel SN 388 24-bit system (recorder) at a sampling rate of 1 ms and a 40,000 pound peak force of two vibrators ensured good signal strength and high quality of the seismic data.

A 7.5×7.5 m^2 bin size was chosen to avoid spatial aliasing up to a stratigraphic dip of 20°, based on interval velocity of 6500 m/s and a maximum frequency of 160 Hz (the upper limit of the sweep used in the survey). A maximum shot-receiver offset of 1332 m was chosen to provide full-fold coverage over the range of MR and UG-2 target depths between 500 m and 1200 m. The nominal fold of coverage was 30 and this was recorded with no increase in costs relative to the earlier surveys due to the ability of the instrumentation to deal with larger numbers of receivers. Due to the small bin size and the medium fold coverage, the density of

shot points per km^2 attained 900 Vibrator Points (VP)/km^2. The migration aperture varied depending on the target depth and dip. The dip migration aperture (margin) was designed so that it could provide full-fold coverage of the subsurface target area after migration. For example, the diffraction migration aperture of 728 m (at 2000 m MR target depth with 20˚ dip) was chosen to provide 75% of diffraction energy at predicted major fault cut-offs.

Seismic resolution

Seismic resolution is defined as the smallest spatial detail resolvable with a given set of conditions (Sheriff, 2002; Chopra et al., 2006; Yilmaz, 2008; Herron, 2011). The ability to resolve a feature in the seismic data is dependent on the dominant frequency of the reflected wave, the seismic velocity and the phase of the wave (Miller et al., 1995; Yilmaz, 2008). The dominant frequency for the 1993 Lonmin 3D seismic data observed during seismic processing is 65 Hz. Seismic resolution can be represented by both a vertical and a lateral resolution. Resolution limit is the minimum separation distance resolvable (Sheriff, 2002). The vertical resolution limit can be expressed in terms of the dominant wavelength, which is controlled by seismic wave velocity and the predominant frequency:

$$\lambda = \frac{v}{f}, \tag{6}$$

where v is velocity and f is the dominant frequency. The dominant wavelength of the 3D seismic data used in this project is ~ 92 m assuming a P-wave velocity of 6000 m/s (the mean velocity observed during processing), zero-phase wavelet and a dominant frequency of 65 Hz.

Geophysicists consider a quarter of the dominant wavelength, e.g. Rayleigh's criterion, to be an acceptable vertical resolution limit (Sheriff and Geldart, 1983; Kearey et al., 2002; Yilmaz, 2008; Miller et al., 1995; Chopra et al., 2006). However, the vertical resolution limit for the seismic data with high signal-to-noise ratio (SNR) can be closer to one-eighth of the dominant

wavelength (e.g. Malehmir et al., 2012 and Manzi et al.,2014, 2017), which is defined by Widess criterion (Widess, 1973). Therefore, the vertical resolution limit of the data using a quarter and one-eighth of the dominant wavelength criteria is given by 23 m and 11 m, respectively. This implies that geological features with thickness less than 23 m (e.g. apparent thickness) cannot be resolved on the conventional pre-stack time migrated seismic sections. However, the use of volume and horizon-based seismic attributes has the ability to enhance the detection of features smaller than the resolution limit (e.g. Manzi et al., 2012).

The lateral resolution is described by the ability to resolve two laterally displaced features as two distinct adjacent features. The lateral resolution limit depends mainly on the width or size of the first Fresnel zone (Figure 3.4) (the area of a reflector from which most of the energy of a reflection is returned and arrival times differ by less than half a period from the first break), (Sheriff, 2002; Yilmaz, 2008; Herron, 2011). The Fresnel zone is defined by the wavelength and frequency.

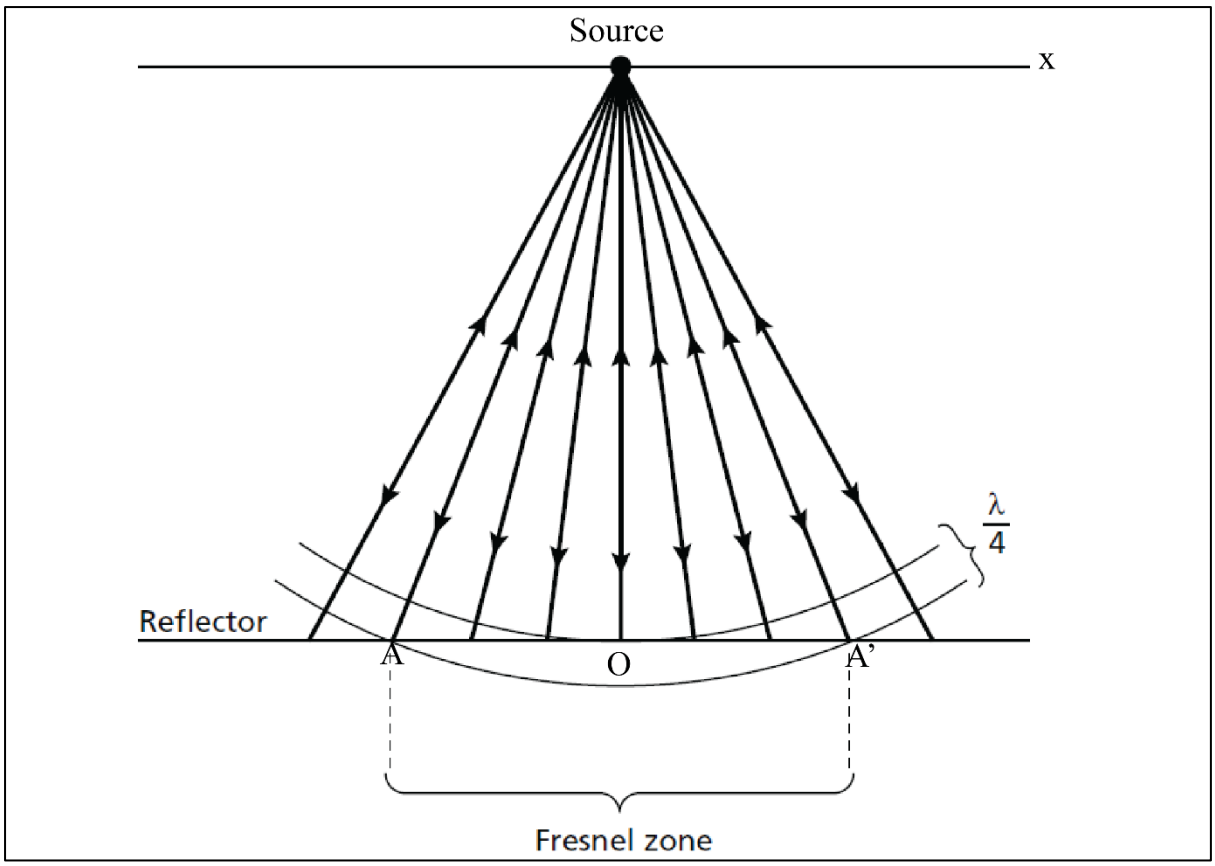

***Figure 3.4**. Definition of the Fresnel zone (AA') (modified from Kearey et al., 2002; Yilmaz, 2008).*

From the Fresnel zone criterion, the lateral resolution is approximately the dominant wavelength (e.g. 93 m for these data) for the unmigrated 3D seismic data (e.g. Manzi et al., 2014). However, for the migrated 3D seismic data the horizontal resolution is dependent on the bin size (7.5 m) This means that any geological features (e.g. faults, potholes and their associated diameters) with spacing less than 7.5 m will not be identified or resolved as two separate features using conventional seismic interpretation methods. However, seismic attributes can be used to enhance the detection of the smallest potholes with diameters below horizontal seismic resolution limit (i.e. 7.5 m for these data).

3.3 PROCESSING

The Lonmin 3D seismic dataset was passed through the standard workflow including field pre-processing and full processing by CGG. Field processing, which provides brute stacks with elevation corrections, was done to evaluate the quality of the data, estimate the signal to noise ratio (S/N), and detect and remove bad and noisy traces. Full processing improved the SNR ratio through various pre-stack operations such as trace editing, gain recovery, linear noise removal, surface-consistent "spiking" deconvolution, zero phase spectral whitening, trace balancing, velocity picking and a 35% stretch mute. Subsequent processing steps included the application of refraction statics, normal move-out correction, 3D Kirchhoff DMO correction, stacking, final datum shift to 1500 m above sea level, 3D finite difference depth migration, velocity analysis, and eventually a full Prestack time migration using 3D Kirchhoff algorithm was implemented.

Velocity analysis and migration have been described in greater detail since they play a major role in interpreting the data. In seismic data processing, it is important that the geometry of the survey is defined correctly to avoid incorrect processing at a later stage (e.g. producing incorrect velocity estimates) (Yilmaz, 2008).

3.3.1 Velocity analysis

To obtain spatially accurate seismic data, a good velocity analysis during processing should be carried out. Velocity analysis involves finding velocities that are associated with the hyperbola that best fits the common midpoint (CMP) data (Sheriff, 2002). The CMP is the point where different traces intersect (Figure 3.5) (Sheriff, 2002). In the processing stages the CMP is first located, data are sorted and a Normal Moveout (NMO) correction is then applied. NMO corrects for the varying source and receiver offsets on the arrival time of reflections (Sheriff,

2002). The NMO allows all the traces to be moved to the same level, e.g. time zero, t(0). The CMP traces are then stacked to increase the signal-to-noise ratio. There are two main types of velocity fields that are often used at the processing stages: the NMO velocity and the stacking velocity. The NMO velocity for dipping reflectors depends mostly on the dip angle and has a hyperbolic function (Kearey et al., 2002; Yilmaz, 2008) given by:

$$t^2(x) = t^2(0) + \frac{x^2}{v_{NMO}^2} \tag{7}$$

where $t^2(0)$ is the observed two-way zero offset time, x is the distance between the source and the receiver, and V_{NMO} is the NMO velocity. The stacking velocity is the velocity field used to stack the traces in a CMP gather (Yilmaz, 2008). The stacking velocity is represented in the hyperbolic form as

$$t_{stk}^2(x) = t_{stk}^2(0) + \frac{x^2}{v_{stk}^2} \tag{8}$$

where t_{stk} is the best stacking path, $t_{stk}(0)$ is the two-way zero-offset time associated with the best fit hyperbola, x is the distance between the source and receiver, and V_{stk} is the stacking velocity.

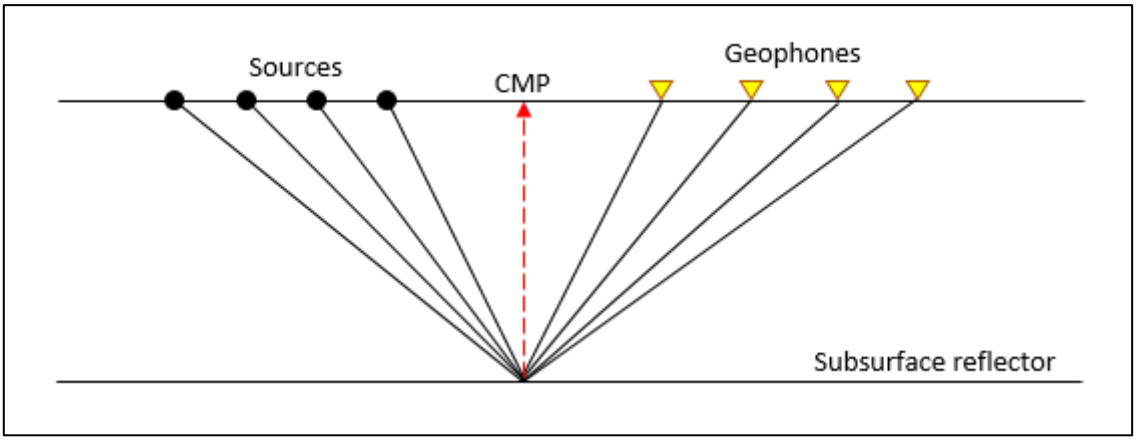

***Figure 3.5**. Common Midpoint (CMP) of a horizontal layer.*

3.3.2 Migration principles

Migration is a process by which seismic events are repositioned in either space or time to their correct subsurface location rather than the location recorded at the surface (Chun and Jacewitz, 1978). Migration allows for dipping events to move to their correct positions, collapses diffractions and increases spatial resolution (Gazdag and Sguazzero, 1984; Yilmaz, 2008). Once a seismic section has been migrated, reflections steepen, shorten, move in the up-dip direction, migration unties 'bowties' in the seismic data and turns them into synclines (Yilmaz, 2008). There are many migration techniques that are used in the processing of seismic data. Migration can be done in time domain, depth domain, before stacking (pre-stack migration) or after stacking (post-stack migration) of the seismic traces. As mentioned earlier, pre-stack time domain migration was carried out on the 3D seismic data by Compagnie Générale de Géophysique (CGG), producing a final pre-stack time migrated (PSTM) volume that is interpreted in this project.

3.3.3 Migration algorithms

Migration algorithms are classified into three classes based on (i) the integral solution to the scalar wave equation – Kirchhoff migration, (ii) the finite-difference solution and (iii) the frequency-wavenumber operation. Chun and Jacewitz (1978), Claerbout (1985), Gardner (1986), Whitmore et al. (1988), and Yilmaz (2001) give comprehensive detail on the above-mentioned algorithms, however this dissertation only provides a few relevant concepts that are related to this study. A wide range of migration techniques are used in the industry because there is not one technique that meets all the requirements needed to provide accurate subsurface images and still be cost effective (Yilmaz, 2008).

3.3.3.1 Kirchhoff migration

Kirchhoff migration is classified as migration by integrating, summing and weighting the input energy along diffraction curves and placing the results at the crests of the diffraction curves

(Sheriff, 2002). Kirchhoff migration works well in rectifying dip angles up to 90°, however, it is unable to handle major lateral velocity variations (Yilmaz, 2008). The Kirchhoff equation that is used in the migration process is an integral form of the wave equation expressing the wave function ψ_p at the point P in terms of the sum (integral) of contributions from a surface enclosing the given point and its normal derivative (Schlumberger, 2015; Sheriff, 2002). Assuming a 2D acoustic, constant density, the wave equation is given by:

$$\frac{\partial^2\psi}{\partial x^2} + \frac{\partial^2\psi}{\partial z^2} - \frac{1}{V^2}\frac{\partial^2\psi}{\partial t^2} = 0 \qquad (9)$$

where $\psi = \psi(x, z, t)$ is the pressure wavefield, x is the horizontal distance, z is the depth and t is a function of time (Hale, 1992). The Kirchhoff integral can be expressed as follows:

$$\psi(x,z,t) = \frac{z}{\pi}\int\left[\frac{1}{r^3} - \left(\frac{2}{Vr^2}\right)\left(\frac{\partial}{\partial t}\right)\psi(x',0,t+\tau)\right]dx' \qquad (10)$$

where x' is the horizontal position of the data recorded at the surface (e.g. z=0), τ is the two-way time (2r/V) (V is the velocity) and r is the distance from x' to x (Hale, 1992; Sheriff, 2002).

The width of the aperture and the dip to migrate seismic events are important parameters of the Kirchhoff migration (Yilmaz, 2008). The migration aperture used for these data varied depending on the target depth and dip. The dip migration aperture (margin) was designed so that it could provide full-fold coverage of the subsurface target area after migration. For example, the diffraction migration aperture of 728 m (at 2000 m MR target depth with 20˚ dip) was chosen to provide 75% of diffraction energy at predicted major fault cut-offs.

3.3.3.2 Finite difference migration

Finite differences migration approximates derivatives by taking the difference of the function at two points (Sheriff, 2002); this method tries to solve the wave equation subject to contextual boundary conditions (Gazdag and Sguazzero, 1984). The finite-difference algorithm can

resolve all types of velocity variations but has different degrees of dip estimates (Yilmaz, 2008). The finite difference equation is given by:

$$\frac{P(t+\Delta t)-P(t)}{\Delta t}\Delta = aP(t) \quad (11)$$

where $P(t + \Delta t)$ is the explicit operator, Δt an arbitrary increment of time, a the matrix coefficient and P the scalar wave equation. The depth step size is an important parameter to the finite difference migration method (Yilmaz, 2008).

3.3.3.3 Frequency-wavenumber (f-k) migration

Frequency-wavenumber migration transforms the data into the frequency-wavenumber domain along radial lines (Gazdag, 1978; Yilmaz, 2001). The steepness of the dip determines how close the radial line is to the wavenumber axis (e.g. the closer the radial lines are to the wavenumber, the steeper the dip) (Yilmaz, 2001). The mathematical expression of the migration method in the frequency-wavenumber domain can be written as:

$$\bar{F}(k_x, k_z) = \frac{k_z}{\sqrt{k_x^2+k_z^2}} F(k_x, \sqrt{k_x^2 + k_z^2}) \quad (12)$$

The transform of the migrated function is $\bar{F}$ and F is the 2-D Fourier transform of the original section (Chun and Jacewitz, 1981; Yilmaz, 2001). $\frac{k_z}{\sqrt{k_x^2+k_z^2}}$ is the scaling factor where k_z represents the horizontal events mapped along the k_z-axis and k_x represents vertical events mapped along the k_x-axis after the phase-shift (Yilmaz, 2001). The frequency-wavenumber algorithm is limited in the ability to resolve velocity variations (more so in the lateral direction) (Yilmaz, 2008). In frequency-wavenumber migration, the scaling factor is important (Yilmaz, 2008).

3.3.3.4 Post-stack versus pre-stack time migration

In post-stack migration, the traces obtained from the computation of the CMP are stacked and then migrated (Gardner, 1985; Sheriff, 2002). Post-stack migrations have shorter computation times and often have a high signal-to-noise ratio, resulting in a more stable migration. On the other hand, pre-stack migrations allow for individual traces to be migrated before they are stacked (Gardner, 1985), which can better handle strong lateral velocity gradients and are tolerant of incorrect moveout assumptions (Sheriff, 2002). This method is more computationally intensive, but it works well for more complex geological environments. Figure 3.6 provides a good example of the differences between pre-stack depth migration and post-stack depth migration in a structurally complex environment.

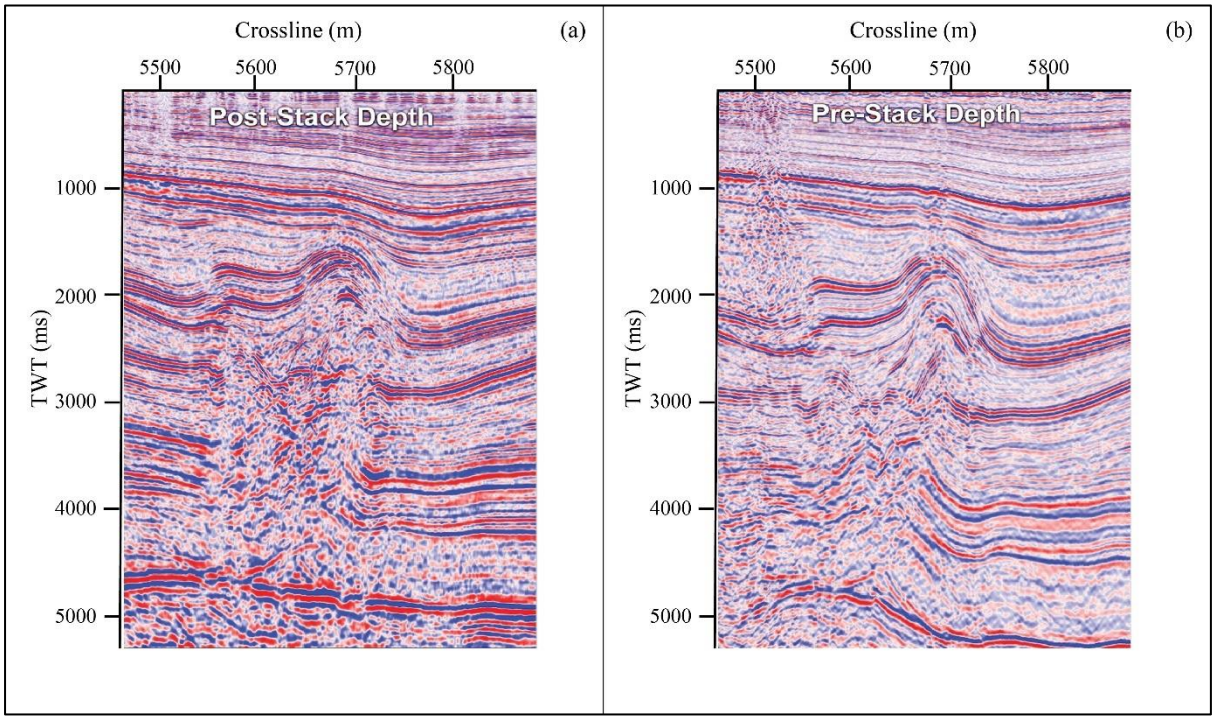

***Figure 3.6**. Example of post-stack migration (a) and pre-stack migration (b) of the same section, where the dipping layer is mapped better in pre-stack migration than in post-stack migration (modified from Paradigm, 2013).*

3.4 INTERPRETATION

Once the data are processed they are interpreted to infer the geology at the subsurface of the Earth. Interpretation methods differ based on the aims of the projects; they involve mapping of geological structures, carrying out a seismic sequence analysis and a seismic facies analysis (Van der Kurk, 2005). The interpretation of a seismic section is highly dependent on the quality of the processing done on the seismic data. At times, seismic attributes are used to help improve the quality of the seismic interpretation. Seismic attributes are tools that can enhance geological features (e.g. potholes, faults and possibly dykes).

3.4.1 Potholes

Potholes are decameter- to hectometre-scaled (diametrically), often near-circular, vertically-extended (Stevenson et al., 2003) slump structures that can disturb mining designs and ultimately decrease the production rate (Stevenson et al., 2003; Van Schoor, 2005; Campbell, 2011). Their depth extent ranges from 1 to 100 m (Trickett et al., 2004; Campbell, 2006; Scheiber-Enslin and Manzi, 2018). Stevenson et al. (2003) attributed the formation of these slump structures to the reef crosscutting its "own unlithified footwall." Potholes cause problems for mine planning and designs because they cause a sudden change in (i) the dip of the strata, (ii) the composition of the hanging and footwall strata, and (iii) an increase in the number of joints and fractures within the area (Stevenson et al., 2003). Potholes have a strong correlation between their abundance and the thickness of the reef, with thinner reefs having more potholes (Viljoen, 1994; Stevenson et al., 2003). Potholes can also be found in the vicinity of the IRUP bodies (Figure 3.7) (Viljoen et al., 1986a; Viljoen and Hieber, 1986; Campbell, 2011).

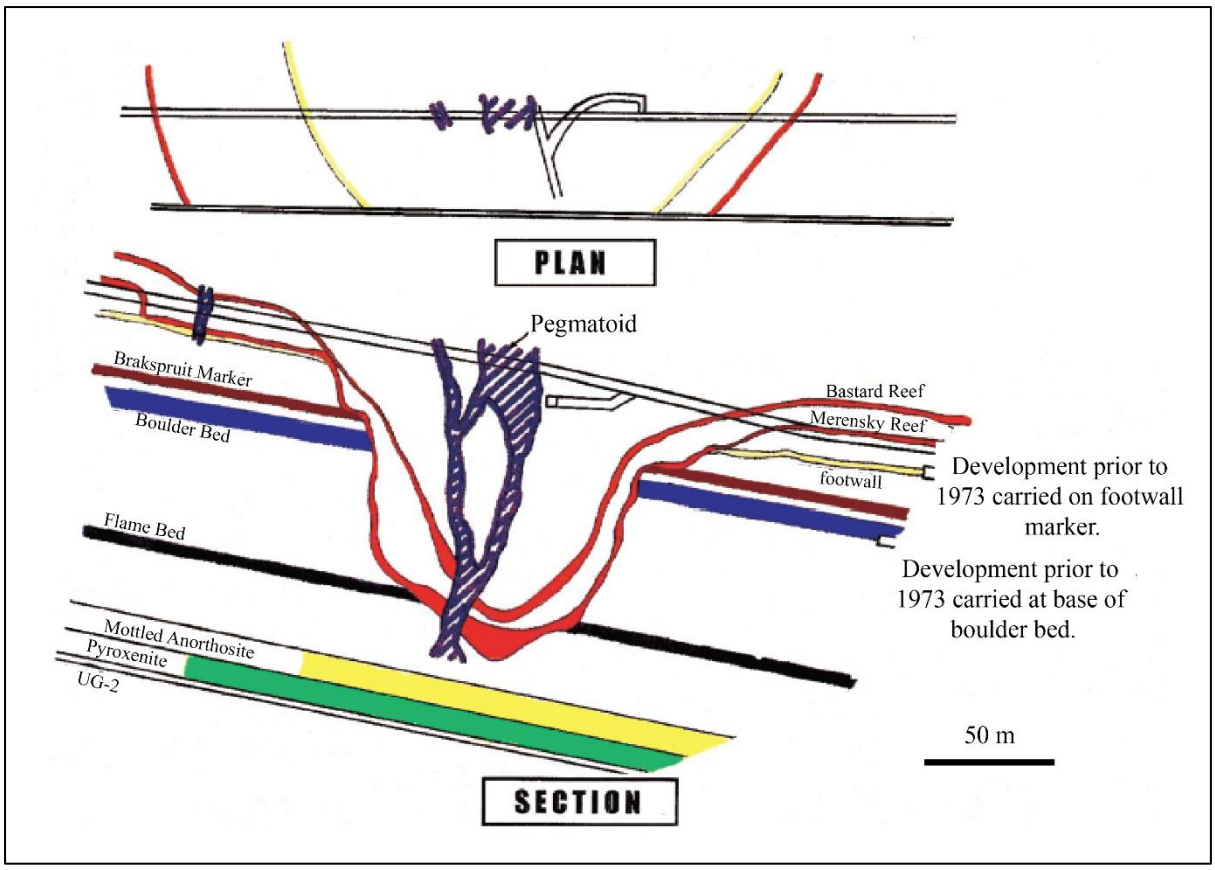

Figure 3.7*. A pothole cored by an iron-rich ultramafic pegmatites (IRUP) body within the Bushveld Complex. The Bastard Reef and Merensky Reef (red lines) show slump structure representative of a pothole while the blue in the middle is the IRUP body (modified from Campbell, 2011).*

3.4.2 Faults

Sheriff (2002) described a fault as "a displacement of rock along a shear surface." The word "fault" was derived as the mining term for a surface where the coal layer was offset (Taylor, 2012). A fault separates a section of rocks into two "fault blocks". Geologists commonly classify these blocks into a hanging wall (the bottom surface of the upper fault block) and a footwall (the top surface of the lower fault block) (Taylor, 2012). There are various types of faults; each fault is defined by the direction that the hanging wall has moved in relation to the footwall (Taylor, 2012). Table 3.1 highlights different types of faults and their characteristics. In seismic data, faults are identified as areas where reflections have been displaced relative to the adjacent areas.

Table 3.1. Types of faults (modified from Sheriff, 2002).

Fault Type	Related terms	Stress Direction		Characteristics
		Minimum	*Maximum*	
NORMAL 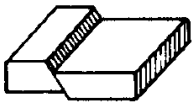	Tension fault Gravity fault Slip fault Listric fault (curved fault plane)	Horizontal (Tension)	Vertical (Gravity)	Dip usually 40° to 70°
REVERSE 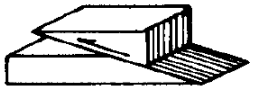	Thrust fault Low angle (dip < 45°) High angle (dip > 45°)	Vertical	Horizontal (compression)	Fault plane may disappear along bedding
STRIKE – SLIP 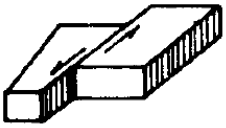	Transcurrent fault Tear fault Wrench fault Right lateral (Dextral) Left lateral (sinistral)	Horizontal	Horizontal	Fault trace often 30° to maximum stress
ROTATIONAL 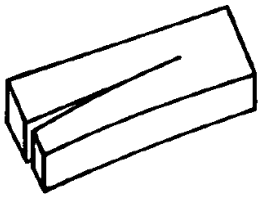	Scissors fault Hinge fault	-	-	Throw varies along fault strike; may vary from normal throw to reverse
TRANSFORM 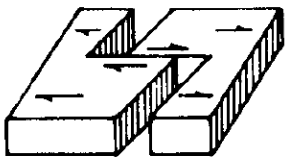	Dextral Sinistral	Horizontal	-	Associated with separation or collision of plates. New material fills rifts between separating plates or one plate rises on another if plates collide

3.5 Seismic attributes

The use of seismic attributes began in the late 1960s and early 1970s, when their significance in the interpretation of seismic section was identified (Barnes, 1999; Chopra and Marfurt, 2007). Barnes (1999) defined a seismic attribute as "a descriptive and quantifiable characteristic of seismic data that can be displayed at the same scale as the original data." Sheriff (2002) further added that a seismic attribute is a measurement that is based on measurements of time, amplitude, frequency, and/or attenuation (Figure 3.8). Attributes assist in enhancing features and patterns that may have been missed or gone unnoticed during seismic interpretation (Sheriff, 2002).

Attributes can be measured along a single trace, on a 3D seismic volume and on either pre-stack or post-stack migrated data. Post-stack attributes are used in the interpretation of this project. Post-stack attributes consist of trace attributes, interval statistics, discontinuity, time-frequency attributes, waveform, and 4D differences (Barnes, 2016). When using seismic attributes, it is often beneficial to use attributes that are mutually mathematically independent (Barnes and Laughlin, 2002; Barnes, 2007; Li and Heap, 2014; Marfurt, 2015). In this thesis, two groups of seismic attributed have been used: horizontal-based attributes and volumetric attributes.

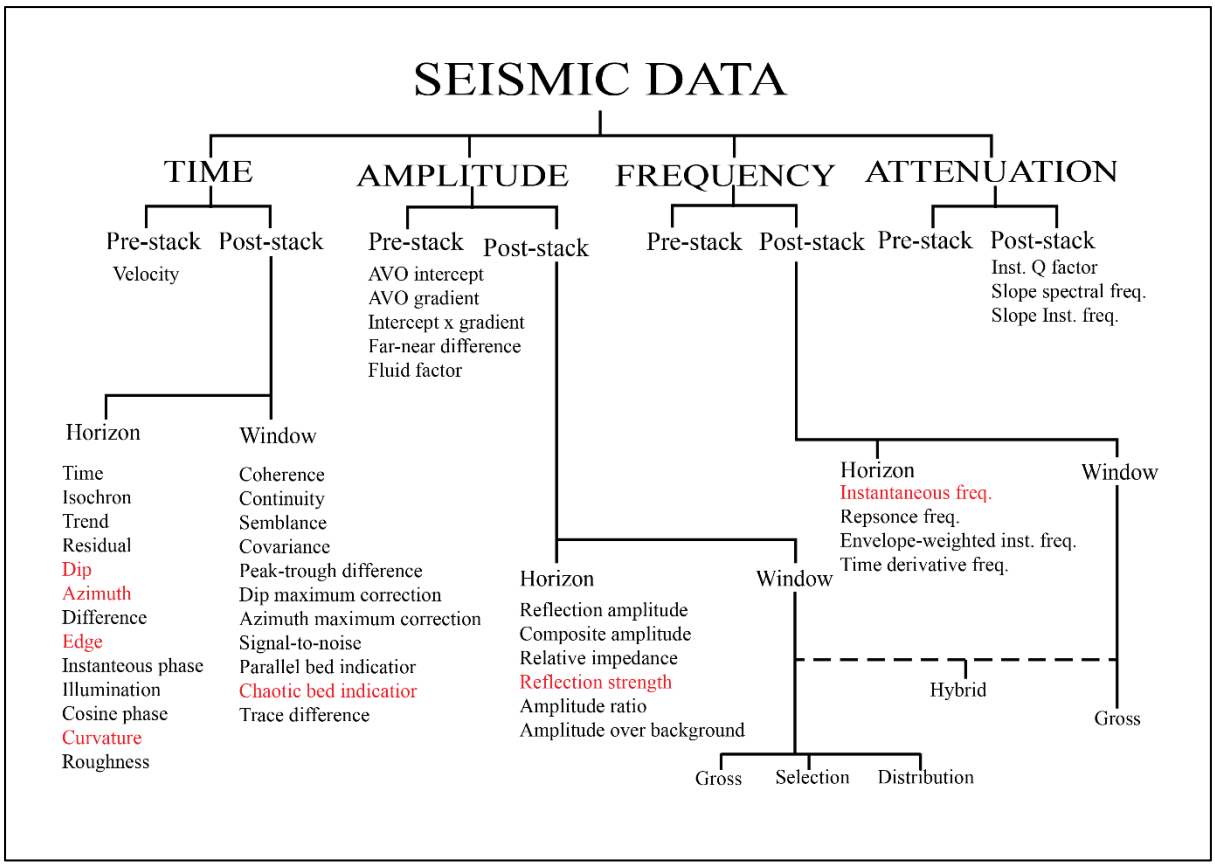

Figure 3.8*. A classification of seismic attributes derived from time, amplitude, frequency and attenuation. The window may be constant interval in either time or between to horizons. Those written in red represent attributes carried out in this study (modified from Browns, 2001).*

3.5.1 Complex-trace attributes

Complex-trace attributes, also called instantaneous attributes, are one of the most commonly used attributes for seismic interpretation (Robertson and Fisher, 1988; Barnes, 2016). Complex-trace attributes have been growing in importance in the interpretation phase since their introduction in the 1970s by Nigel Anstey and others at Seicom Delta (Taner et al., 1979; Robertson and Fisher, 1988; Sheriff, 1991; White, 1991; Brown, 1996; Manzi et al., 2013). Initially, complex-trace analysis for 1D data was operated on individual traces to produce trace attributes. However, today a complex-trace analysis can operate across multiple traces to produce volume attributes and are often found as subsection under volume-based attributes (Taner et al., 1979; Barnes, 2016).

When a complex-trace attribute is computed, a seismic trace is treated as the product of two separate attributes: instantaneous amplitude and cosine of the instantaneous phase (also known as paraphase) attributes (Manzi et al., 2013; Barnes, 2016). Other complex-trace attributes (such as frequency, bandwidth, dip and dip azimuth attributes) are derived from the instantaneous amplitude and the instantaneous phase information of a seismic trace (Barnes, 2016). Complex-trace attributes are often implemented to resolve information that is hidden in the migrated seismic sections (Barnes, 1991; Taner, 2001; Chopra et al., 2006; Chopra and Marfurt, 2007; Manzi et al., 2013).

The principle of computing a complex-trace analysis lies in the separation of amplitude information from the phase information in the seismic data (Taner et al., 1979; Barnes, 2016). This idea stemmed from the Fourier analysis as the Fourier frequency transform can be represented as amplitude and phase in the polar form (Barnes, 2016). Commonly, the Fourier transform is represented in the Cartesian form as cosine and sine spectra. However, it is better to represent the Fourier transform in the amplitude and phase spectra for physical studies (Taner et al., 1979; Barnes, 2016) this is because seismic traces are displayed in waves with amplitude and phase and. Assuming a 1D case, the cosine and the sine spectra of the Fourier transform, represented by X(f) and Y(f) respectively, can be related to amplitude and phase spectra of the Fourier transform represented by (A(f)) and (θ(f)), respectively (Taner and Sheriff, 1977; Taner et al., 1979; Renè et al., 1986).

$$X(f) = A(f)\, cos\, \theta(f) \tag{13}$$

$$Y(f) = A(f)\, sin\, \theta(f) \tag{14}$$

The same can be done for a seismic trace. A seismic trace x(t) can be separated into the product of two attributes, (i) instantaneous amplitude attribute, a(t), and (ii) the cosine of the instantaneous phase $\theta_i(t)$ attribute e.g.

$$x(t) = a(t)\, cos\theta_i(t) \tag{15}$$

However, equation 15 relates two unknown functions with one known function hence, the quadrature trace y(t), given by:

$$y(t) = a(t)\, sin\theta_i(t), \tag{16}$$

is defined as follows as the Hilbert transform of the seismic trace:

$$y(t) = h(t) * x(t) \tag{17}$$

where h(t) is the Hilbert transform operator that rotates the phase rotator by subtracting 90° of phase from a seismic trace x(t) to produce a quadrature trace y(t).

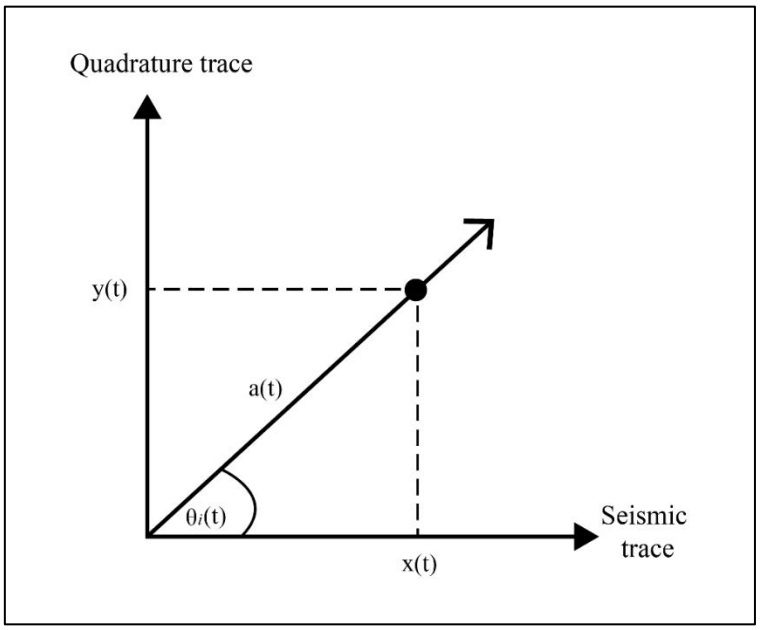

Figure 3.9. *Graphical representation of the relationship between Quadrature (y(t)) and the seismic trace (x(t)) in Cartesian coordinates. The seismic quadrature traces represent a point in Cartesian coordinates, and the amplitude and phase attributes signify the point in polar coordinates. θi(t) is the cosine of the instantaneous phase and a(t) is the instantaneous amplitude attribute.*

Instantaneous amplitude and phase can be derived from the seismic and quadrature trace (Figure 3.9) through the Cartesian to Polar coordinate transform:

$$a(t) = \sqrt{x^2(t) + y^2(t)} \tag{18}$$

$$\theta_i(t) = \arctan\left[\frac{y(t)}{x(t)}\right] \tag{19}$$

Equation 18 and 19 form the basis of all other complex-trace attributes. In this project, in addition to instantaneous amplitude and instantaneous phase, instantaneous frequency and bandwidth attributes were used. Instantaneous frequency is defined as the rate of change in time of the instantaneous phase (equation 19) over a specific window (Azevedo and Pereira, 2009). Instantaneous bandwidth is defined as the absolute value of the derivative of the envelope with time divided by the envelope, over a specified window (Azevedo and Pereira, 2009). Mathematically, the bandwidth is represented as:

$$\omega_B = \left|\frac{d\left[\frac{(env(t))}{dt}\right]}{env(t)}\right| \tag{20}$$

where d[(env(t))/dt] is the decay factor (Azevedo and Pereira, 2009).

The abovementioned complex-trace attributes assist in the interpretation as they assist in highlighting the horizons during picking and track thin horizons which are characterized by low SNR, complex faulting and low amplitudes. The envelope attribute is useful at identifying intrusions and discontinuities. The instantaneous phase attribute helps the interpreter identify lateral continuity of the reflectors. The instantaneous frequency attribute highlights changes in lithology and change in bed thicknesses (Subrahmanyan and Rao, 2008).

3.5.2 Volumetric-based attributes

3.5.2.1 Amplitude attributes

Amplitude attributes are the most used seismic attributes as they make use of the most important seismic property, the magnitude of the seismic trace values (Barnes, 2016). The amplitude attribute uses the change in acoustic impedance to reflect changes in geology (Herron, 2011). This attribute measures the reflected energy within a given window and gets rid of any unwanted phase effects that are identified when picking amplitudes (Manzi et al., 2013). Commonly used amplitude attributes are reflection strength, root mean square (RMS) amplitude, maximum amplitude, average absolute amplitude and total energy attributes. Amplitude attributes highlight bright spots and dim spots caused by gas, tuning, hard streaks, or porosity changes within the data (Barnes, 2016). A shortfall with using the amplitude attribute is that it may not give accurate results if automatic gain or trace balance have been applied in the data during the processing stage (Herron, 2011; Barnes, 2016).

3.5.2.2 Structural smoothing

Structural smoothing is a volumetric attribute that applies a 3D Gaussian filter to a 3D volume to reduce the noise in the data (Azevedo and Pereira, 2009). The structural smoothing attribute considers the bed estimation orientation using the principal component estimation method thus executing a structure-oriented filter reducing the noise without losing any edge information within the data (Azevedo and Pereira, 2009). This attribute is used to reduce noise in the data and improve the continuity of the reflections (Rojo et al., 2015).

3.5.2.3 Chaos

The chaos attribute (also known as the disorder attribute), measures lack of organisation of the seismic signal within a 3D volume (Koson et al., 2014). Chaos attribute is computed from the eigen-analysis of gradient covariance and is based on application of second derivative operators in the three axial directions within a seismic cube. This attribute is useful at mapping faults, stratigraphy, and fluid indicators. The main advantage of the chaos attribute is that it has the

ability to produce the same response for the same seismic signature irrespective of whether it is in a low- or high-amplitude region (Randen and Sønneland, 2005).

3.5.2.4 Variance attribute

The variance attribute uses the local variance as a measure of signal unconformity (Randen et al., 2001). The local variance is computed from horizontal sub-slices (Randen at al., 2001; Randen and Sønneland, 2005). If a slice is taken from a layer with no discontinuities then the amplitude variance will be small, while if the slice experiences amplitude changes (e.g. due to a faulting) then a larger variance will be expected (Randen et al., 2001). The variance attribute is an edge imaging and detection method that helps with the imaging of channels and faults (Pigott et al., 2013; Koson et al., 2014). Mathematically, the variance attribute is defined as:

$$\sigma_t^2 = \frac{\sum_{j=t-\frac{L}{2}}^{j=t+\frac{L}{2}} w_{j-t} \sum_{i=1}^{I} (x_{ij} - \overline{x_j})^2}{\sum_{j=t-\frac{L}{2}}^{j=t+\frac{L}{2}} w_{j-t} \sum_{i=1}^{I} x_{ij}^2} \quad (20)$$

where x_{ij} is the sample value at a horizontal position, i and j are the vertical time sample indices. W_{j-t} is the vertical smoothing term over a window with a length L (Azevedo and Pereira, 2009).

3.5.2.5 Ant-tracking

Ant-tracking is an attribute designed to enhance edges such as faults, fractures and other linear anomalies (Azevedo and Pereira, 2009). This attribute mimics the concept of ant colonies looking for food (Azevedo and Pereira, 2009). Ants use pheromones to mark the shortest path taken from the nest the food; these pheromones guide the other ant members to the food (Figure 3.10) (Pedersen et al., 2002; Cox and Seitz, 2007; Azevedo and Pereira, 2009; Ngeri et al., 2015). Similarly, the ant-tracking attribute uses agents (virtual ants) to move along the seismic volume emitting pheromones (Azevedo and Pereira, 2009; Ngeri et al., 2015). Faults are then

identified as areas strongly marked with pheromones (Randen et al., 2001; Fehmers and Hocker, 2003; Skov et al., 2003; Aguado et al., 2009; Khair et al., 2012; Ngeri et al., 2015).

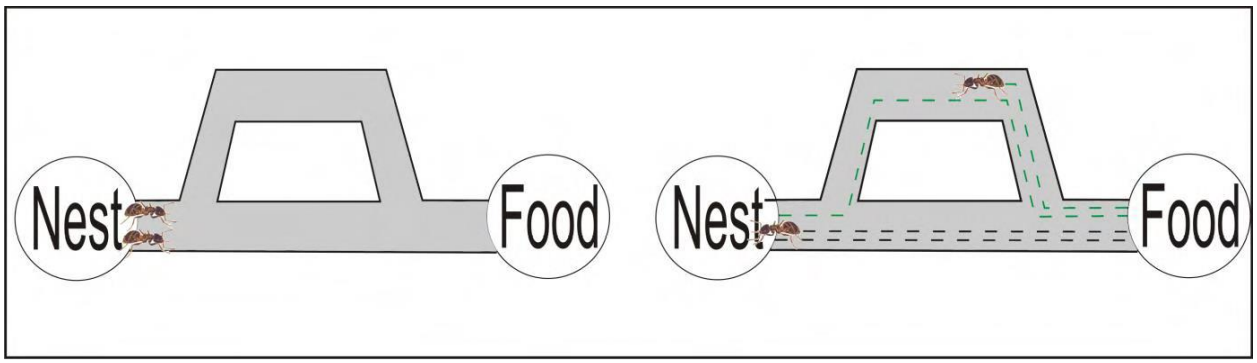

***Figure 3.10**. Illustration of ants starting at the same point at the nest finding food. The ant with the shortest path (marked in black) will have more pheromones than the path longer path (marked in green) taken by the other ant. (modified from Azevedo and Pereira, 2009).*

To implement the ant-tracking attribute a few steps (Figure 3.11) are required: (i) seismic conditioning – to reduce spatial noise in the data; (ii) generate an edge detection cube; (ii) implement an edge enhancement volume, e.g. the chaos attribute (Azevedo and Pereira, 2009).

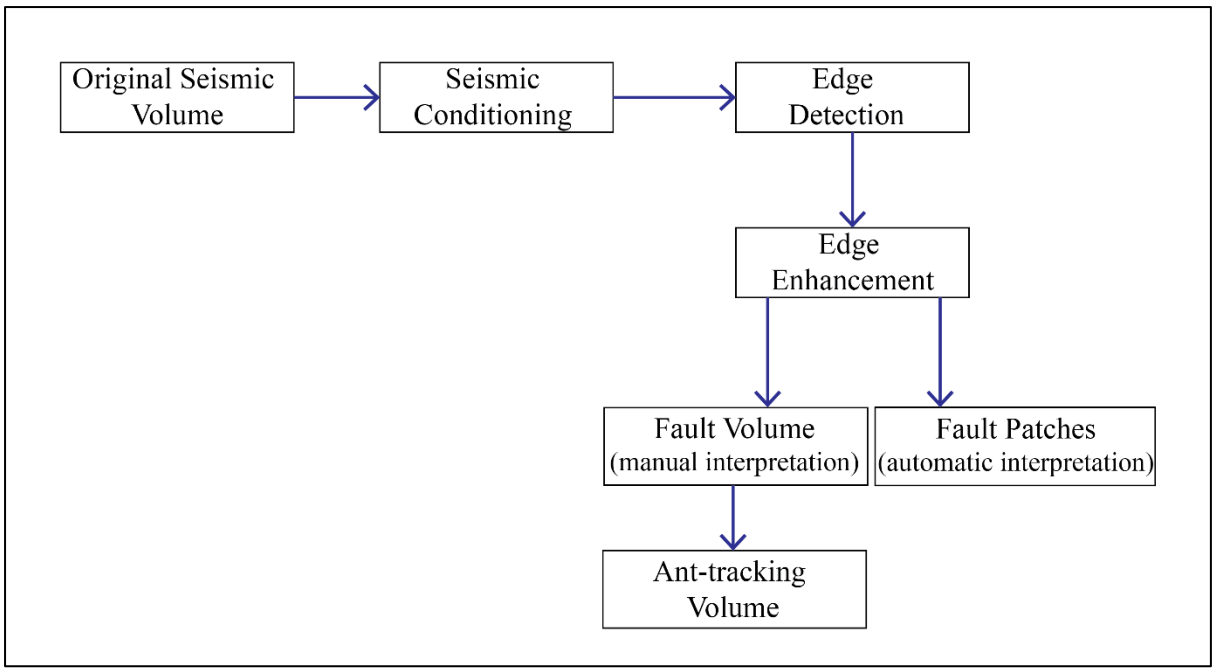

Figure 3.11. *Flow Chart for the implementation of the ant-tracking attribute highlighting the seismic conditioning, edge detection and edge enhancement to create the ant-tracking volume and fault patches (modified from Azevedo and Pereira, 2009).*

3.5.3 Horizon-based attributes

Horizon-based attributes, unlike volume-based attributes, are applied directly to the picked horizon to enhance subtle features within the horizon. Following the successful application of horizon-based attributes to the hard rock 3D seismic data from the Witwatersrand gold fields for mining industry (Manzi et al., 2012), horizon-based attributes have been used in this study to aid the interpretation of the 3D seismic data from the Bushveld Complex.

3.5.3.1 Dip and dip azimuth attributes

Dip and dip azimuth attributes were first described by Dalley et al. (1989) as the "amount of inclination of a horizon in the subsurface" and "the direction of this inclination measured from a local reference direction," respectively. This definition was later simplified by Rijks and Jauffred (1991); they defined dip and dip azimuth as the magnitude and direction, respectively,

of the time gradient vector from a local reference (Figure 3.12). Dip and dip azimuth can be mathematically defined as:

$$Dip = \sqrt{\left(\frac{\partial t}{\partial x}\right)^2 + \left(\frac{\partial t}{\partial y}\right)^2} \quad (21)$$

$$Azimuth = \arctan\left(\frac{\partial t}{dy} / \frac{\partial t}{\partial x}\right) \quad (22)$$

where $\frac{dt}{dx}$ is the dip in ms.m^{-1} in the x direction and $\frac{dt}{dy}$ is the dip in the y direction, in an x-y Cartesian coordinate system.

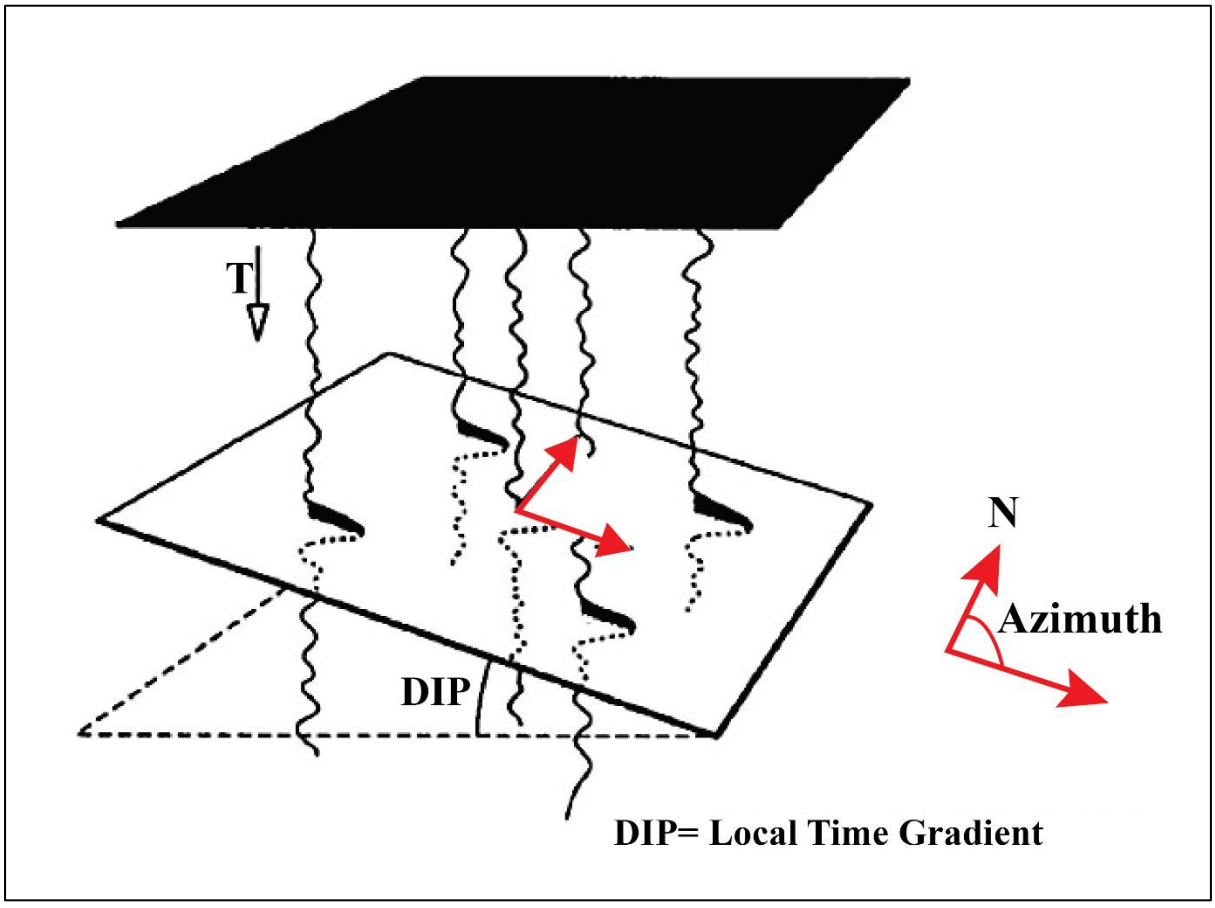

***Figure 3.12**. Representation of dip and dip azimuth attributes where dip and dip azimuth are defined as the magnitude and direction of the time gradient, respectively (modified from Rijks and Jauffred, 1991).*

It is important to analyse the results from dip and dip azimuth attributes independently, because some features might be enhanced by the dip attribute but not by the dip azimuth attribute and

vice versa. However, it is still vital that these attributes are integrated. This can be done using the combined dip and dip azimuth map (Rijks and Jauffred, 1991), allowing for simultaneous enhancement of features by both attributes.

3.5.3.2 Edge detection attribute

The edge detection attribute is a combination of dip and dip azimuth variations that have been normalized to local noise of the interpreted horizon (Manzi et al., 2012a). The edge detection attribute detects discontinuities (e.g. faults, dykes and fractures) within a seismic horizon (Rock Deformation Research, 2004; Manzi et al., 2012b). This is because in a seismic section, faults often decrease the amplitude of the reflector (Randen et al., 2001). The edge detection attribute measures the changes in the signal amplitude within the horizon. This attribute has a great advantage of not introducing artefacts by smoothing and is sensitive to small amplitude variations in the data (Randen et al., 2001; Manzi et al., 2012a). The edge detection attribute is therefore ideal for enhancing subtle faults, which are difficult to see visually.

4 METHODOLOGY

To achieve the aims and objectives of this study, 3D reflection seismic data were interpreted using various methods and a statistical analysis was carried out. Figure 4.1 shows a flow chart that summaries the required steps.

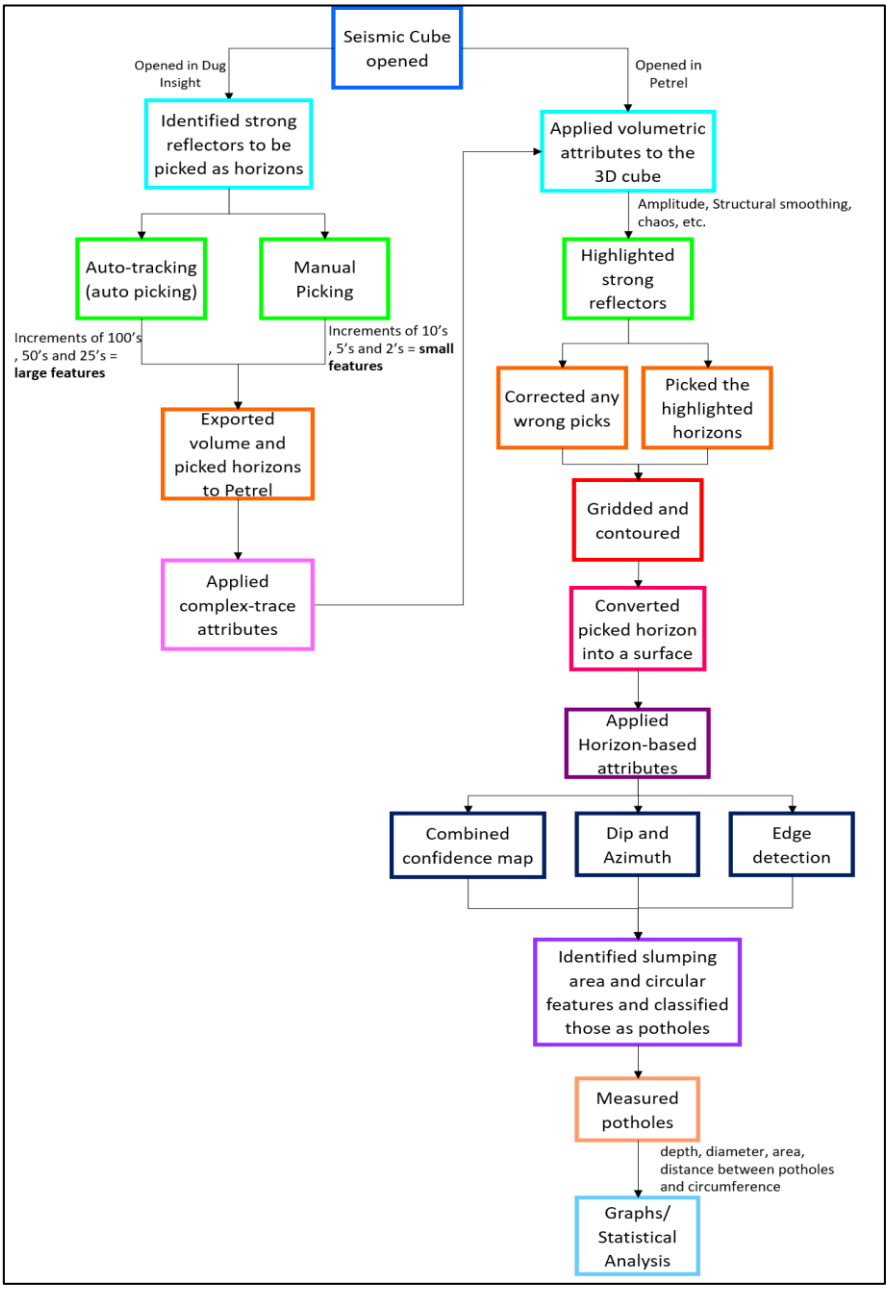

***Figure 4.1**. Flow chart summarising the methods used. The steps that were followed started off with auto-picking and manual picking then complex-trace attributes were applied. Created horizons and located potholes. The potholes were measured, and a statistical analysis was carried out.*

4.1 SEISMIC INTERPRETATION

Interpretation of the 3D reflection seismic data was done using DUG Insight (https://dug.com/dug-insight/) and Petrel software (https://www.software.slb.com/products/petrel) packages. To begin, complex trace attributes (e.g. amplitude, instantaneous frequency and instantaneous phase) implemented in Petrel software were computed for the seismic cube in order to identify the horizons within the volume.

4.1.1 Complex trace attributes

The complex trace attributes were implemented using different Hilbert filter window sizes, however, upon inspection it was noticed that the window size of 33 could be used as there was insignificant change that could be identified from increasing the window size. For example, decreasing the window size reduced the visibility of the horizons.

4.1.2 Horizon interpretation

The volume was imported into DUG Insight and four of the strong identified reflectors with constant phase were picked. The peak of the wave was chosen by a positive polarity of the data, using both 3D auto-picking (commonly referred to as auto-tracking) and manual picking. Auto-picking is more time-efficient than manual picking for picking horizons and interpreting structural features but only works on easy data sets.

In the auto-picking method, the interpreter plants seeds on the inline, crossline and time slices to extrapolate the extent of the horizons or geological features. The auto-picking function follows a workflow (refer to Guru for full explanation in Schlumberger, 2015) that searches for areas in the data that are similar to where the seeds' are placed and extrapolates along the seeds. Manual picking is more time-consuming but typically more precise, especially in

structurally complex areas. The best practice for picking a horizon is to incorporate both auto-picking and manual picking. In addition to the methods of picking, the quality of the picked horizon is dependent on the quality of the data and the complexity of the geology of the area (complex structures may result in uncertainties in picking).

Picking was initially performed with inline, crossline and time slice (Figure 4.2) at increments of 100s, 50s, and 25s (i.e. picking every 100th line, every 50th line etc.) using the auto-picking method; detailing all the larger geological features. This was followed by manual picking in increments of 10s, 5s, and then 1s (e.g. every single inline and crossline) to increase the detail within the interpretation. Slumping of the horizons was mapped as potholes (see chapter 5.3 for detailed classification of potholes). The larger potholes (> 300 m) were identified from the large inline and crossline increments, and the smaller potholes (< 300 m) were mapped from the smaller inline and crossline increments. Once the horizons were picked the main fault was then picked in increments of 100s, 50s, 25s, 10s, 5s and then 1s offsetting the four horizons.

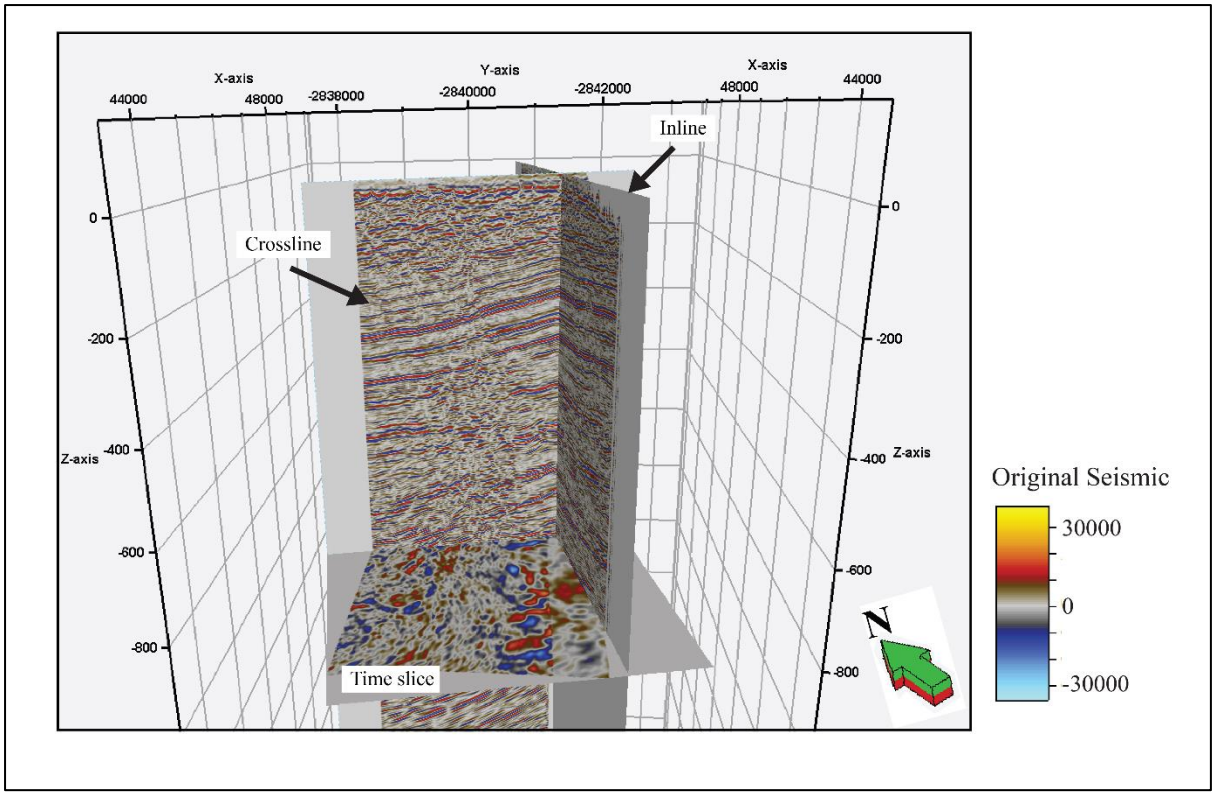

***Figure 4.2**. Seismic cube highlighting the inline, crossline and time slice that were used to pick the horizons and identify the potholes.*

4.1.3 Pothole identification

The data were then imported into Petrel software package. In Petrel, the picked horizons were checked for correctness and locations of incorrect picking were corrected. The picked horizons were gridded and contoured using different algorithms based on the amount of detail revealed about the horizon. Gridding is a method of spatially-regularizing irregularly-spaced data via interpolation and fills in the gaps in the horizon. Gridding is done for two main reasons, to facilitate automated contouring and manipulate picked horizons (Herron, 2011). The gridding process (the kriging method was used) is done through testing different parameters and analysing the output contour maps (Herron, 2011). The gridding and contouring process creates a surface of the picked horizon. To identify the potholes, two methods were used, namely: the method of enhancing the potholes with attributes and the method of taking the difference between two surfaces.

4.1.3.1 Identification of potholes by seismic attributes

The first attribute that was applied to the surfaces was the combined confidence classification attribute. This attribute combines the surface stability index and the thick-slice volume amplitude. The surface stability index is defined as the estimated confidence in the surface by comparing the depths or two-way travel times of surrounding locations, highlighting areas where the surface fluctuates in elevation (Schlumberger, 2015). On the other hand, the thick-slice volume amplitude is defined as a histogram equalization of the RMS amplitude on either side of the surface location.

The parameters used to perform the confidence classification map were a stability window with a radius 3 and the sample window of size 5 for both the surface stability index and the thick-slice volume amplitude respectively. The various attributes, as well as the inlines, crosslines and time slices, allowed for the identification of potholes within the different horizons. To better delineate potholes, the areas which had dark spots and those that exhibited a change in contour, dip and elevation (enhanced by the different attributes) were located. Figure 4.3 shows an example of a normal TWT section (Figure 4.3a), which is enhanced to highlight the potholes as dark spots by the RMS attribute (Figure 4.3b). This was further confirmed by placing inlines and crosslines across those features to investigate if the seismic sections were also characterized by these slumping features. If all methods showed similar results, then the feature would be marked as a pothole.

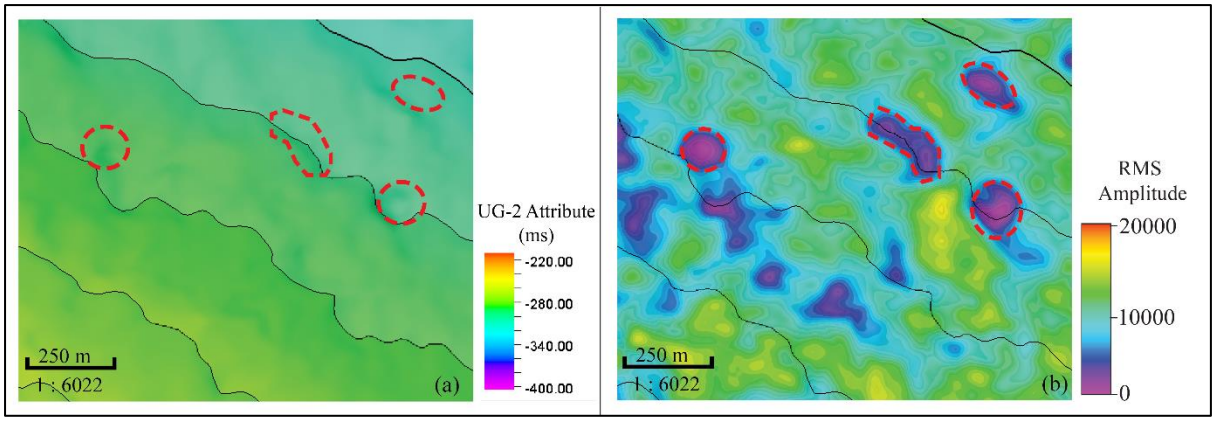

Figure 4.3. *Image highlighting how potholes were enhanced on the UG-2 using RMS amplitude attribute. a) shows an area with potholes however they are unclear; b) shows the potholes being enhanced using the RMS amplitude attribute applied on the horizon. Some of these dark spots are circled in red. RMS: Root Mean Square.*

4.1.3.2 Identification of potholes by difference-of-two-surfaces

To identify potholes by computing the difference between-two-surfaces, a surface of the horizon was created with a large grid spacing of 450 x 450 (Figure 4.4a) to maintain only the regional dip of the area but remove all smaller features. Then the picked UG-2 horizon (Figure 4.4b) was subtracted from the gridded surface (Figure 4.4a). The resultant surface (Figure 4.4c) showed the potholes and the elevated features on the horizon after the regional is removed. However, since the focus was only on the potholes, the elevated features were removed leaving only the slump structures on the horizon (Figure 4.4d).

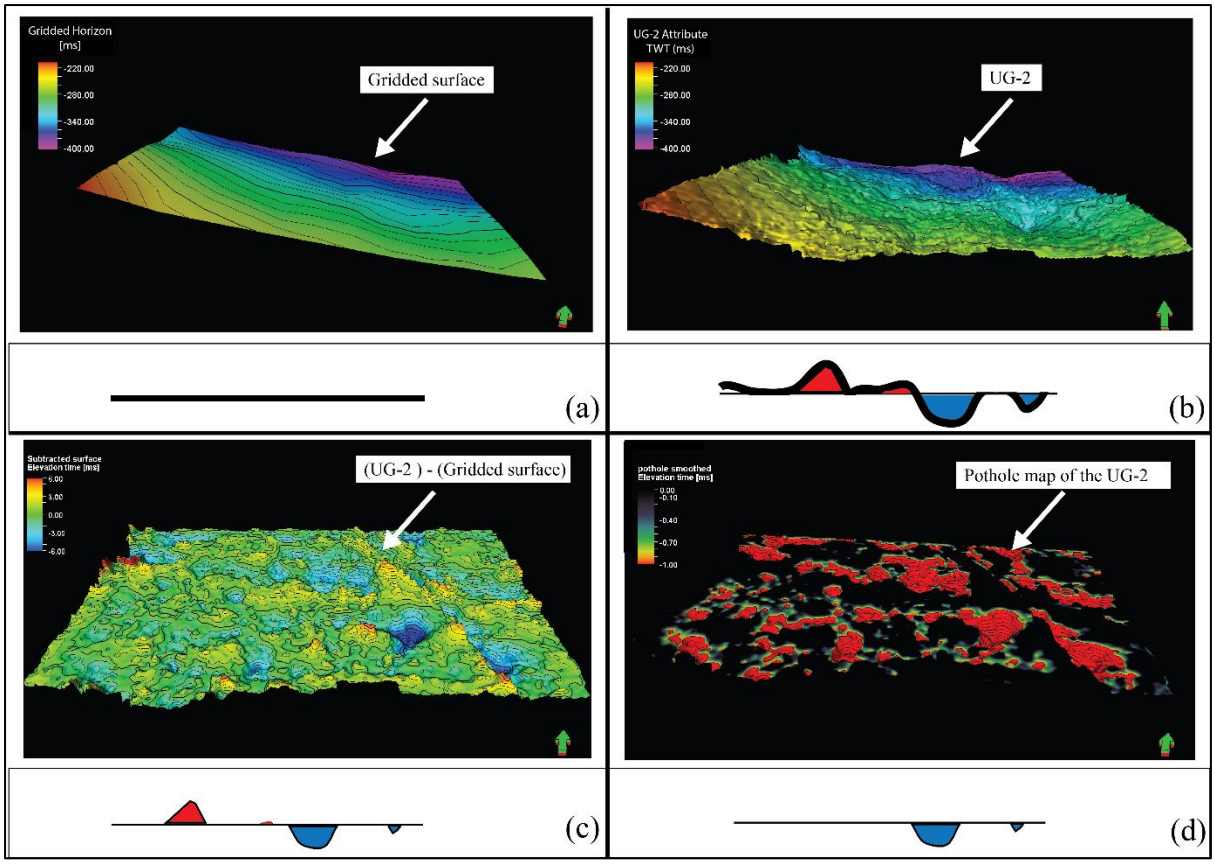

Figure 4.4. *A schematic of the difference-of-two-surfaces method where (a) is a 450 x 450 gridded surface of the UG-2 horizon maintaining only the regional dip; (b) the picked UG-2 horizon; (c) is the difference between the gridded surface and the horizon showing positive amplitude anomalies and negative anomalies; (d) showing only the negative anomalies interpreted as potholes. The symbol below figures shows how first there is only a straight gridded line while the UG-2 has different features (elevated features – red, slump structures – blue). The regional is removed and the features are only remaining (again elevated features – red, slump structures – blue) lastly the elevated features are removed leaving only the slump structures (slump structures – blue). VE = 25.*

4.1.4 Volume-based attributes

The use of volumetric attributes allows for increased confidence in the interpretation. As mentioned above, structural smoothing, variance and chaos attributes were utilized in this study. The ant-tracking volumetric attribute made use of all the volumetric attributes. Therefore, they will be discussed during the rundown of how the ant-tracking was executed.

Ant-tracking

The ant-tracking attribute was applied to the seismic cube in order to identify small scale faults that could not be seen due to the faults being smaller than the resolution limit. Chapter 3 discussed the stages that are undergone when applying the ant-tracking attribute: seismic conditioning, edge detection, enhancement and interpretation.

For the seismic conditioning stage, the structural smoothing attribute was computed on the seismic cube to reduce the noise in the data (Khair et al., 2012). Figure 4.5 shows the results after the application of the structural smoothing attribute. Following the application of the structural smoothing attribute the AGC attribute was applied so as to further highlight the remaining reflections. Figure 4.6 shows the results of the AGC on the structurally smoothed volume.

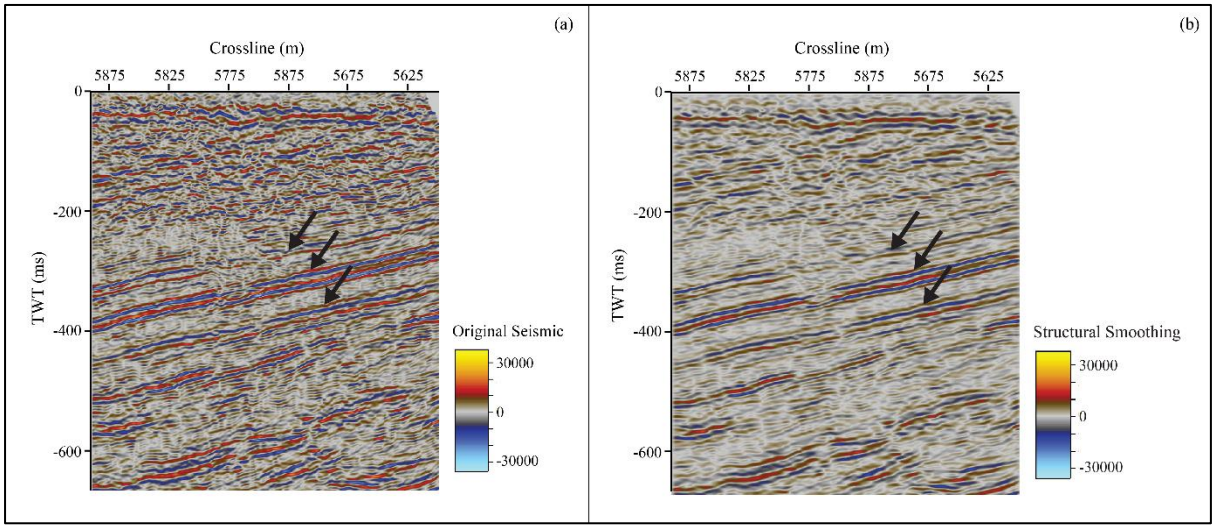

***Figure 4.5**. Inline 1531 where (a) is the seismic section before the application of the structural smoothing attribute and (b) after the application of the structural smoothing attribute. It is clear to see that the structural smoothing attribute has increased the signal-to-noise ratio. The attribute also enhanced the continuity of the strong reflectors (highlighted with the arrows).*

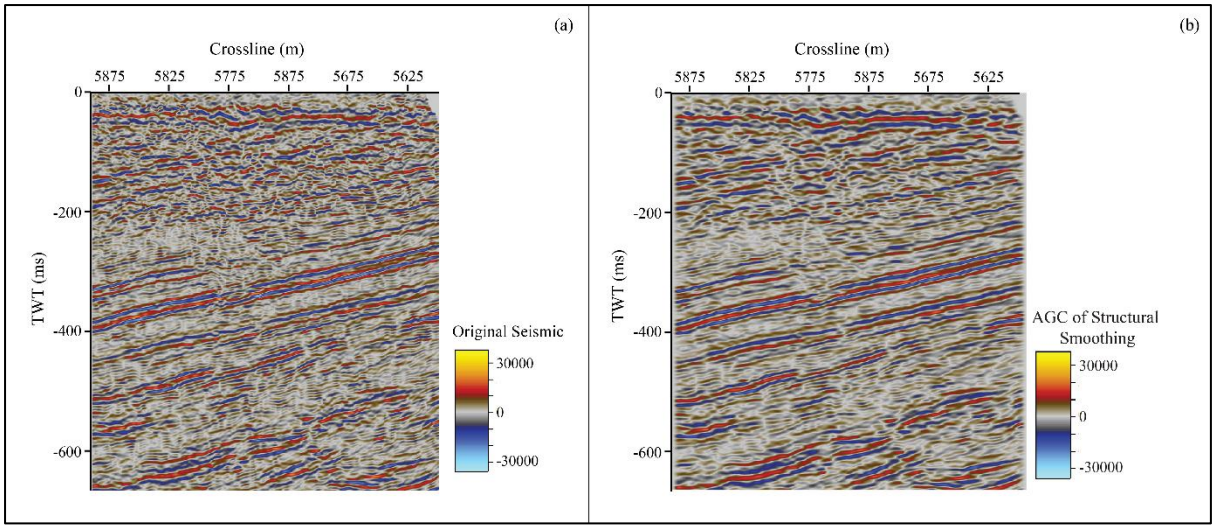

Figure 4.6*. Inline 1531 where (a) is the original seismic section and (b) is the section after the application of the structural smoothing attribute followed by the AGC. The AGC attribute magnifies the horizons making the picking process simpler.*

To enhance edges in the data, we applied the chaos attribute to the 3D seismic data. To apply the chaos attribute, a filter size of 1.5 in the x, y, z direction was used. This filter size was used because a smaller filter size (0.2) introduced noise to the data while a larger filter size (10) showed little information. The chaos attribute allowed us to identify areas where the reflections were inconsistent, and areas characterized by discontinuities within the data. The chaos attribute also allowed for the identification of the large faults in the data, indicated by arrows in Figure 4.7b, which were not apparent in the original seismic section (Figure 4.7a).

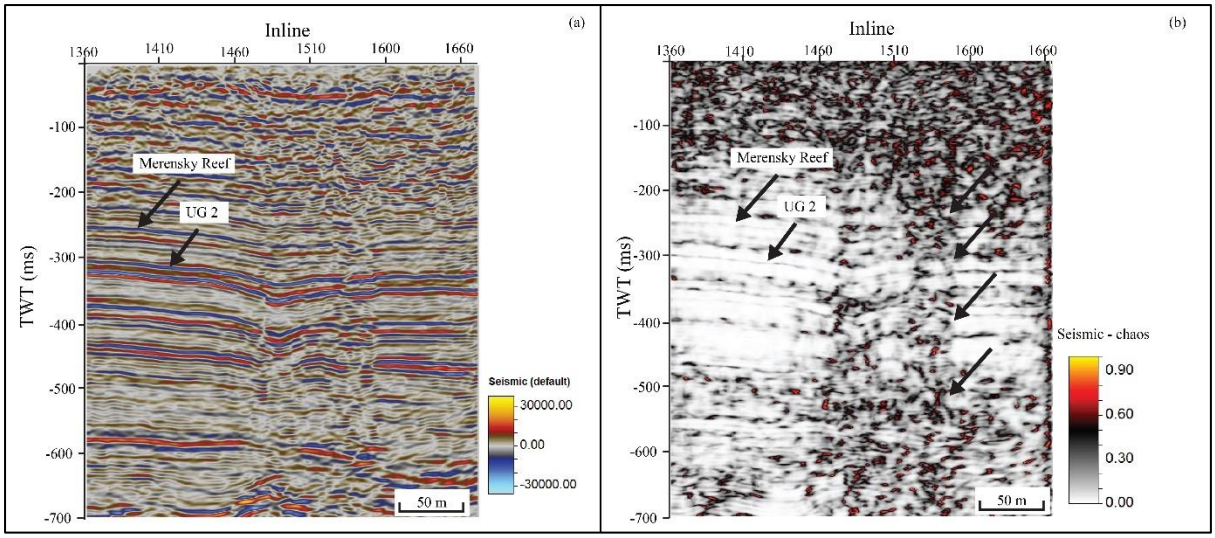

***Figure 4.7**. Crossline 5780 where (a) is the original seismic section and (b) the seismic section after the application of the chaos attribute. This attribute enhances the continuity of the major economic horizons (Merensky Reef and UG-2) and the areas with low amplitude reflections (e.g. faults).*

The enhancement stage is the stage where the ant-tracking attribute is applied. The attribute is applied on the previously constructed chaos attribute. In order to get the optimal result from the ant-tracking attribute, aggressive ants were used (a more vigorous method whereby the ants are allowed to detect the faults in a more flexible manner), parameters shown in Table 4.1, followed by passive ants (a more conservative method whereby the ants move along the signal stronger direction), parameters shown in Table 4.2. The aggressive ants were implemented first because the major fault was already identified using seismic attributes. Therefore, applying the aggressive ants first would give the finer details and the passive ants, thereafter, would reduce any noise introduced by the aggressive ants. A stereonet filter (controls the orientation the ants move in order to highlight faults in a particular direction) is often used to highlight or eliminate faults that dip in a particular direction. However, in this study the stereonet filter was not applied to the seismic data to highlight all faults for further interpretation.

Table 4.1. Parameters used when applying aggressive ants to achieve an ant-tracking result.

Parameters	Aggressive
Initial ant boundary (Defines the initial distribution of agents. Large values result in loss of detail)	7
Ant-track deviation (Controls the amount of deviation allowed on either side of the tracking direction)	2
Ant step size (The number of voxels an ant agent can move with every increment. An increase in this value will lower the resolution)	3
Illegal steps allowed (Defines the number of steps an ant agent can take without finding a local maximum in one direction in its search distance)	1
Legal steps required (The extent of connectivity of the detected edges)	3
Stop criteria (%) (The percentage of illegal steps that any agent is allowed)	5

Table 4.2. Parameters used when applying passive ants to achieve a result for ant-tracking.

Parameters	Passive
Initial ant boundary (Defines the initial distribution of agents. Large values result in loss of detail)	5
Ant track deviation (Controls the amount of deviation allowed on either side of the tracking direction)	2
Ant step size (The number of voxels an ant agent can move with every increment. An increase in this value will lower the resolution)	3
Illegal steps allowed (Defines the number of steps an ant agent can take without finding a local maximum in one direction in its search distance)	2
Legal steps required (The extent of connectivity of the detected edges)	2
Stop criteria (%) (The percentage of illegal steps that any agent is allowed)	10

The final stage was to interpret the highlighted faults and produce the fault patches. Figure 4.8b shows the benefits of using the ant-tracking attribute. The attribute was able to delineate a fault that was not visible prior to applying the ant-tracking attribute (Figure 4.8a).

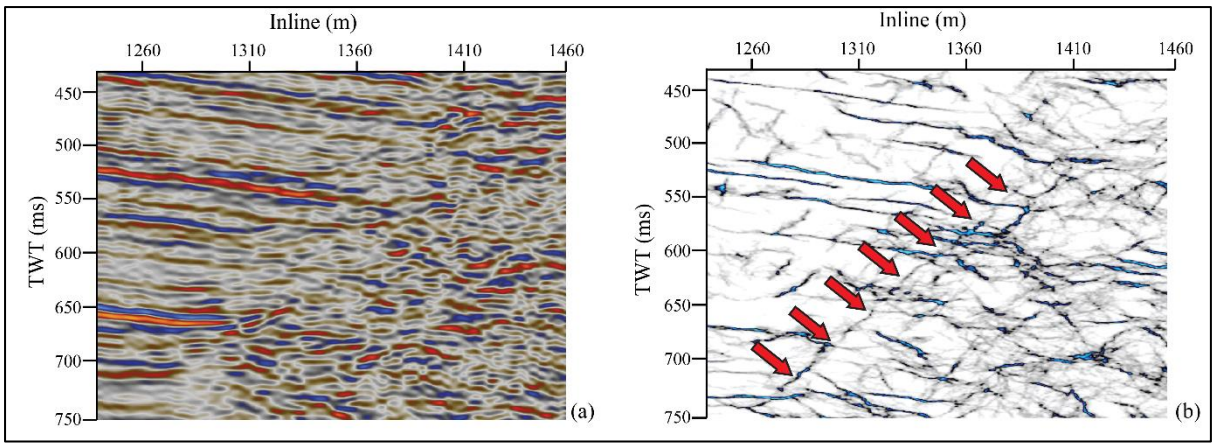

***Figure 4.8**. Crossline 5770 showing (a) an amplitude section prior to the application of the ant-tracking attribute and (b) the section after the application of the ant-tracking attribute. The ant-tracking attribute was able to delineate a linear feature that was previously unidentified (highlighted in the red arrows).*

4.2 STATISTICAL ANALYSIS

The identified potholes were geo-referenced (from an estimated centre), and the following parameters were measured for statistical analysis: their depths (e.g. from top to the bottom of the pothole), diameters, area and circumference. The geo-referencing allowed for the location of the potholes to determine their distribution, while the measured information gave characteristics of the potholes. This information was entered in a database and a code to generate graphs (using MATLAB and R studios, see Appendix A to C) was written to identify the relationship between the location of the potholes, their size and depths of the potholes.

4.3 SPATIAL ANALYSIS

4.3.1 Quadrant analysis

Quadrant analysis is a type of analysis that can identify the spatial distribution of some features over an area of occurrence. A quadrant analysis is performed on a mapped area by dividing the map into several equal-sized sub-areas (called quadrants), such that each sub-area contains a

number of points (Davis, 2002). The data points are said to be uniformly distributed if each sub-area contains the same number of points of some feature of interest (Davis, 2002).

To implement a quadrant analysis on pothole distributions over an area, the mean number of potholes per quadrant is calculated. Once this value is determined we can use a suitable hypothesis model, such as a Poisson model, which tests if the potholes are randomly distributed. This model can be given by the equation:

$$P(r) = e^{(-\frac{m}{T})} \frac{\left(\frac{m}{T}\right)^r}{r!}, \tag{23}$$

where r is the number of potholes per quadrant, m the total number of potholes, T the total number of quadrants. The values obtained in the above equation 23 were then multiplied by number of quadrants (T) to get an expected value which would be used to compare with our observed data. To analyse the observed data, the coordinates recorded above for each pothole in Q-GIS were plotted and a map was created such that the study area was divided into 500 m^2 grids (e.g. 10 x 6 grid). Then the number of grid elements with no potholes was counted and that number was recorded, and then this was followed by counting how many grids had one pothole and so forth until all potholes were counted for. Then a test of goodness fit (χ^2) was calculated and used together with the determined degrees of freedom (e.g. v = c – 2, where c is the number of categories).

4.3.2 Nearest neighbour analysis

To conduct the nearest neighbour analysis, MATLAB (see a code in Appendix C) was used to calculate the distance from one pothole to all the other potholes then the shortest distance from one pothole to another for each of the potholes was taken as the nearest neighbour. To

determine the mean distance (the observed mean distance) and the expected mean distance, the Donnelly (1978) correction method was used, which can be approximated as:

$$\bar{\delta} \approx \frac{1}{2}\sqrt{\frac{A}{n}} + \left(0.514 + \frac{0.412}{\sqrt{n}}\right)\frac{p}{n}, \quad (24)$$

where, A is the area of interest, n is the number of potholes and p the perimeter of the rectangular study area. Consequently, a ratio of the observed and the expected mean was calculated and, based on this value, it was possible to deduce if the data were clustered or not.

4.3.3 Kernel density distribution

The kernel density estimation calculates the density of features within a predetermined neighbourhood for point data. In order to implement a kernel density distribution, a smoothly curved surface is created over each point. The value of the surface is highest where there is a data point and diminishes away from the point within a fixed search radius from the point. To determine the search radius, a few parameters must first be calculated including: the mean centre, distance from the (weighted) mean centre of all the points, weighted median of the distances (D_m), the standard distance (SD). Together the parameters are used in the following equation:

$$search\ radius = 0.9 \times \min\left(SD, \sqrt{\frac{1}{ln(2)}} \times D_m\right) \times n^{-0.2}, \quad (25)$$

where *n* is the sum of all the data points. The *min* suggests that, out of the obtained results the smaller value will be used as the search radius. In this study the kernel density distribution was implemented in Q-GIS by first importing the pothole coordinates as points. This was then used to generate the kernel density heat map.

4.3.4 Cluster analysis

Cluster analysis is a type of statistical analysis that uses a suite of techniques to create groups in any dataset according to some characteristic represented by the data. There are many algorithms that can be used for cluster analysis. For the purpose of this study, k-means clustering is chosen, which is a commonly used technique in statistical analysis. K-means clustering is a type of a centroid model where initial cluster centres as seeds are iteratively moved into localized minimum sum of squared-distance configurations (Lloyd, 1982). In this technique, at each time step, an assignment and an update stage occur in sequence. During the assignment stage, each data point is assigned to a point, known as the cluster mean, which minimizes its Euclidean distance. During the update stage, new means are calculated as the centroids of their present data configuration. These steps occur iteratively until new assignment steps no longer change classification of the data points. Since this is a hill-descent type of algorithm, there is no guarantee that the solution is a global minimum. Hence repetitions and random initializations are frequently used to overcome local minima.

5 DETECTION OF POTHOLES AND FAULTS THROUGH SEISMIC ATTRIBUTES

5.1 POTHOLE CHARACTERISTICS

Carr et al. (1994) described potholes as "discrete quasi-elliptical areas" with diameters between 10 and 200 m. Potholes are identified where approximately 30 m of the normal footwall stratigraphy has been misplaced and the layer has been disrupted (Buntin et al., 1985; Viljoen and Hieber, 1986; Carr et al., 1994). For the purpose of this study, potholes are defined as areas where the horizon slumps downward. Seismically, potholes can be identified through the presence of low amplitude or chaotic seismic reflections and circular shaped features along the seismic horizon, which are enhanced by various seismic attributes. This chapter looks at how various complex-trace attributes, volumetric attributes and horizon-based attributes delineate seismic horizons of interest and their associated potholes. Although multiple horizons were identified throughout the seismic volume, the horizon-based attributes were only computed for the UG-2 and Merensky Reef (MR) as those are of economic importance.

5.2 COMPLEX-TRACE ATTRIBUTES

Seismic data are usually contaminated by both random and coherent noise, which can sometime hamper the successful application of seismic attributes. 3D reflection seismic data used for this study have high SNR, and thus form a basis from which various attributes could be derived. Prior to the application of seismic attributes, certain type of noise was suppressed through careful post-stack smoothing.

Different complex-trace attributes were used to see if features could enhance the visibility of the various horizons. The following complex-trace attributes were applied: instantaneous

amplitude (envelope), instantaneous phase, instantaneous frequency, and instantaneous bandwidth. Figure 5.1a is the original seismic section before the computation of complex-trace seismic attributes. Figure 5.1b shows the results obtained from the application of the envelope attribute. The envelope attribute (Figure 5.1b) could detect layers of high energy reflections with values ranging from 12500 to 17500. The envelope attribute was also able to enhance the visibility of subtler changes in the layering that may have been missed on the original seismic volume (Figure 5.1a). The envelope attribute made identifying the different horizons easier as the high amplitude values (20000 – 25000) stood out from the low amplitude values (0 – 10000). On the other hand, the instantaneous phase attribute (Figure 5.2b) resolved and mapped the continuity of thin seismic reflections across the section, which was not clear in Figure 5.1a. However, this attribute also enhanced noise within the data, owing to its sensitivity to noise, which complicates the interpretations of strong reflectors.

The instantaneous frequency attribute section (Figure 5.3b) is dominated by frequencies ranging from 0 to 150 Hz. Low frequency seismic events (0-50 Hz) represent strong reflections associated with thin stratigraphic units. The strong and thick stratigraphic boundaries are characterised by frequency values from 100 Hz up to 150 Hz. The instantaneous bandwidth attribute (Figure 5.4b) is also dominated by low frequencies ranging from 0 to 50 Hz, which correspond to strong reflections. However, the thin layered seismic reflections exhibit frequencies between 50 and 100 Hz.

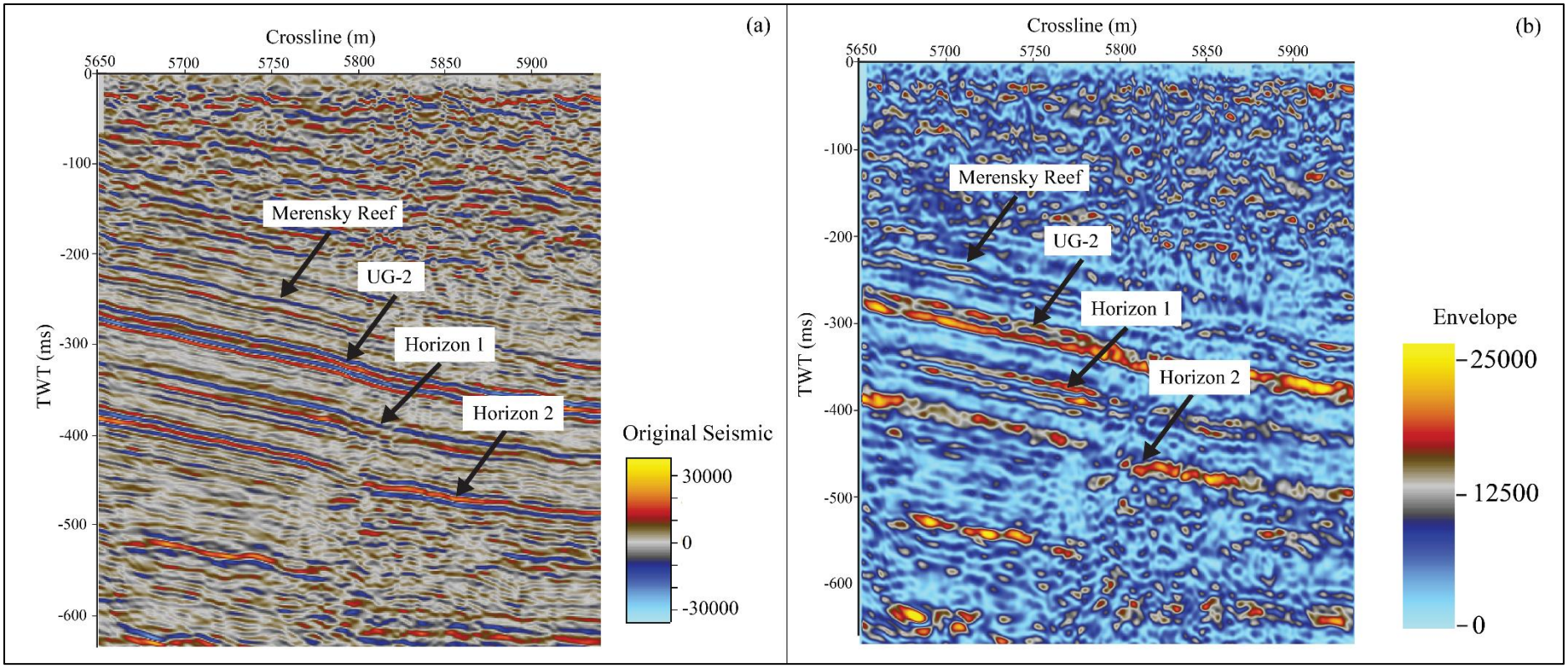

Figure 5.1. *Inline 1391 (a) before the application of the envelope attribute and (b) after the application of the envelope attribute. The envelope attribute was able to detect layers of high energy reflections with values ranging from 12500 to 17500. Note that the attribute was able to enhance the visibility of subtler changes in the layering that may have been missed in (a). The economic horizons (Merensky Reef and UG-2) were identified along with two other horizons.*

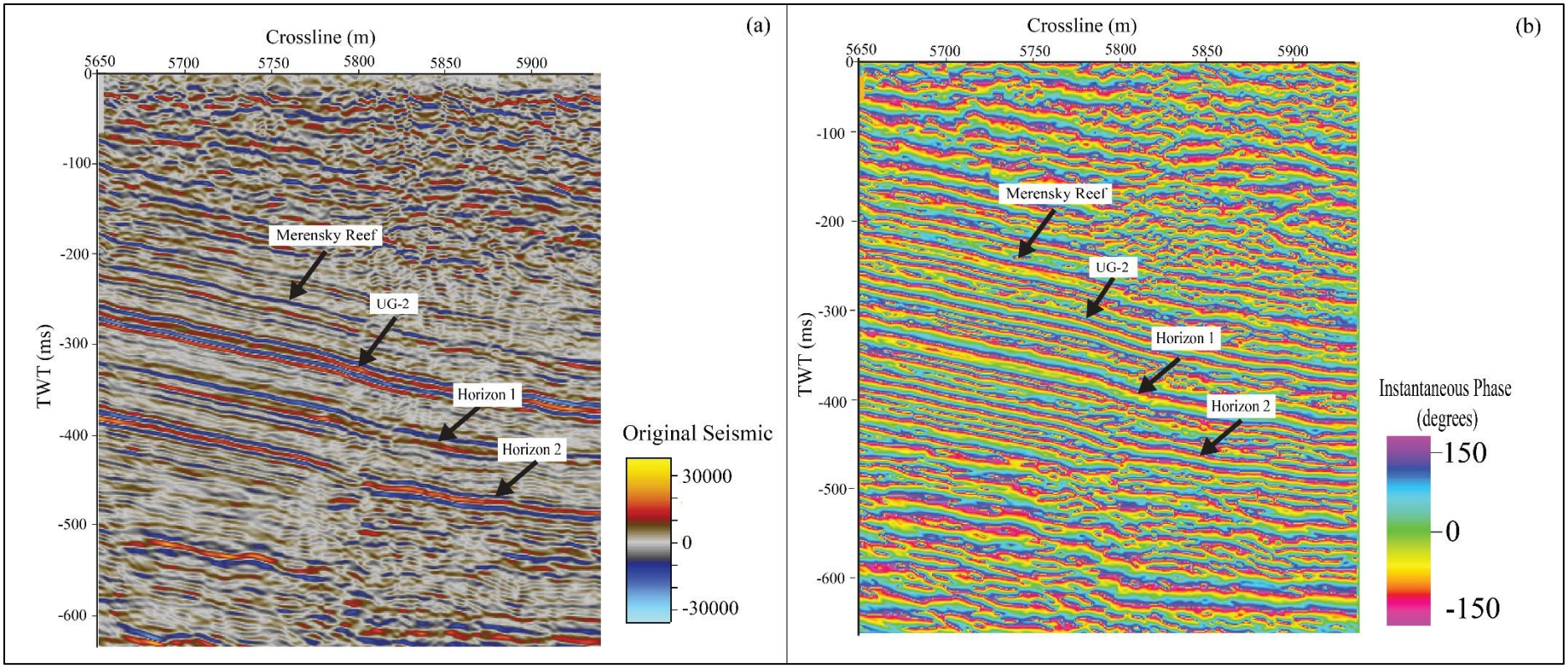

Figure 5.2. *Inline 1391 (a) before the application of the instantaneous phase attribute and (b) after the application of the instantaneous phase attribute. The instantaneous phase attribute resolved the continuity of thin seismic reflections across the section with instantaneous phase with values ranging from -150 to 150 Hz. However, this attribute also enhanced noise within the data when compared to (a). The economic horizons (Merensky Reef and UG-2) were identified along with one other horizons.*

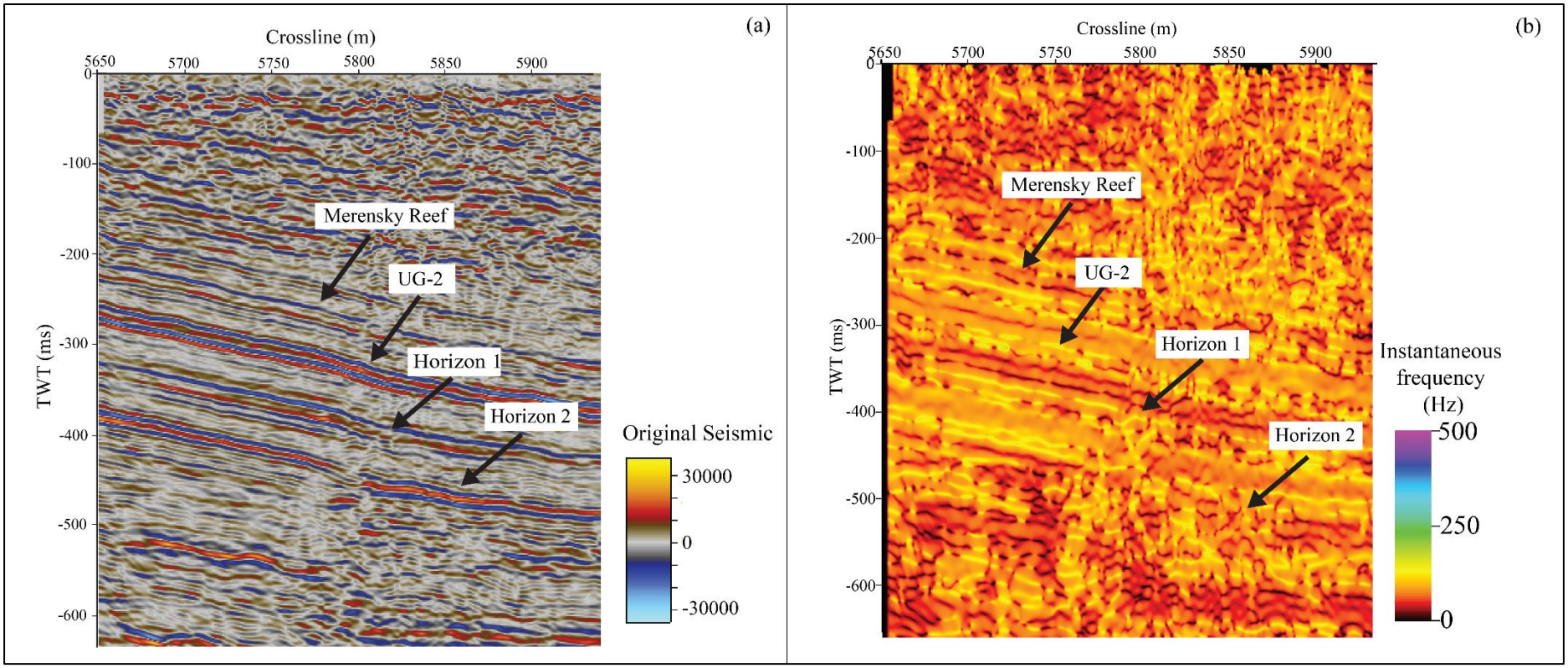

Figure 5.3. *Inline 1391 (a) before the application of the instantaneous frequency attribute and (b) after the application of the instantaneous frequency attribute. The section was dominated by frequency values ranging between 0 – 150 Hz. The attribute shows the horizons as bright yellow layers (frequency value of 150 Hz). The economic horizons (Merensky Reef and UG-2) were identified along with other horizons.*

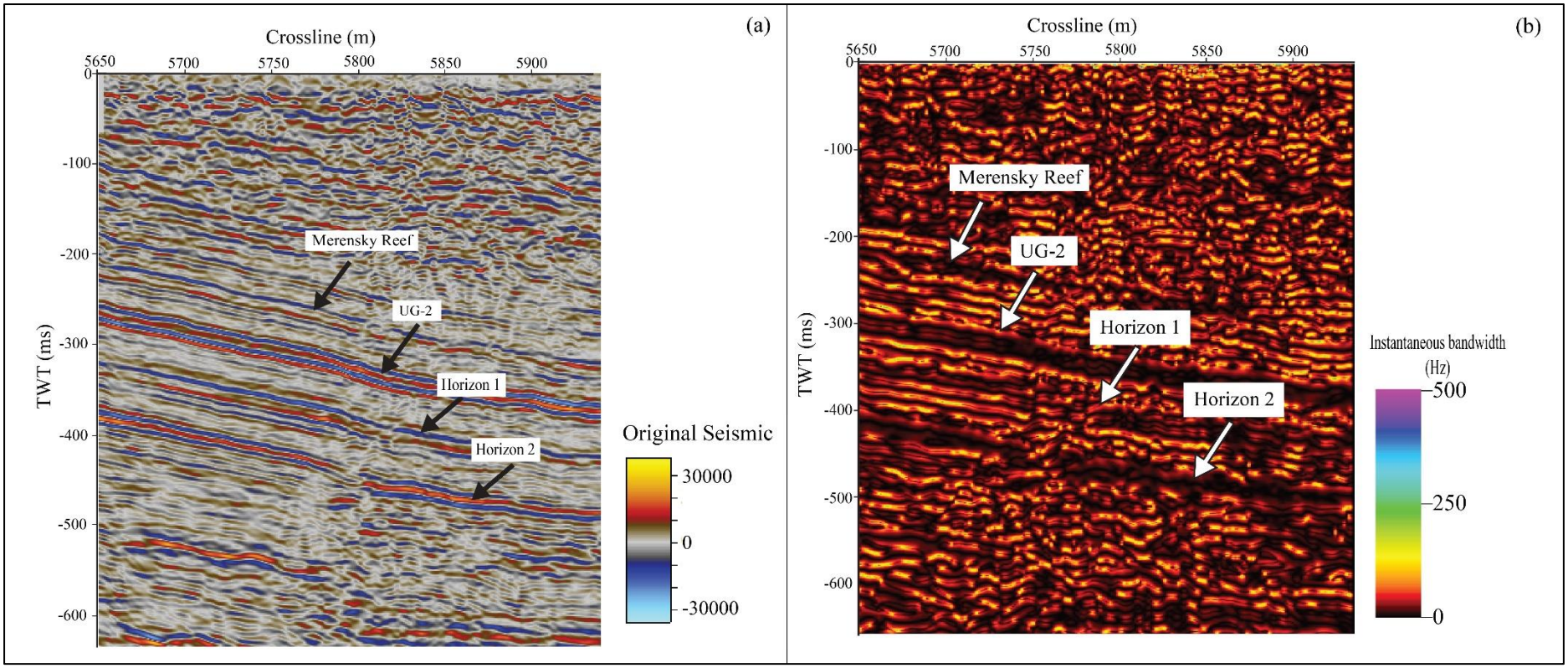

Figure 5.4. *Inline 1391 (a) before the application of the instantaneous bandwidth attribute and (b) after the application of the instantaneous bandwidth attribute. The section was dominated by frequency values ranging between 0 – 50 Hz. The attribute shows the horizons as bright yellow layers (frequency value of 170 - 180 Hz). The economic horizons (Merensky Reef and UG-2) were identified along with other horizons.*

5.3 VOLUMETRIC ATTRIBUTES

5.3.1 Structural smoothing

Structural smoothing attribute was applied to further enhance the quality of the seismic volume by reducing the noise. Figure 5.5 shows the structurally smoothed vs the original seismic section. The structural smoothing filter shows a slightly higher signal-to-noise ratio than the original section there was no significant change between the original and the structurally smoothed section. Figure 5.6 shows the uninterpreted (Figure 5.6a) and interpreted (Figure 5.6b) seismic sections after applying structural smoothing to the data. The seismic section exhibits four strong seismic reflections (Figure 5.6b), which are cross-cut by three vertical discontinuities. The first two strong reflections are associated with the two economic horizons of interest in the area, the Merensky Reef (MR) and Chromitite layer (UG-2).

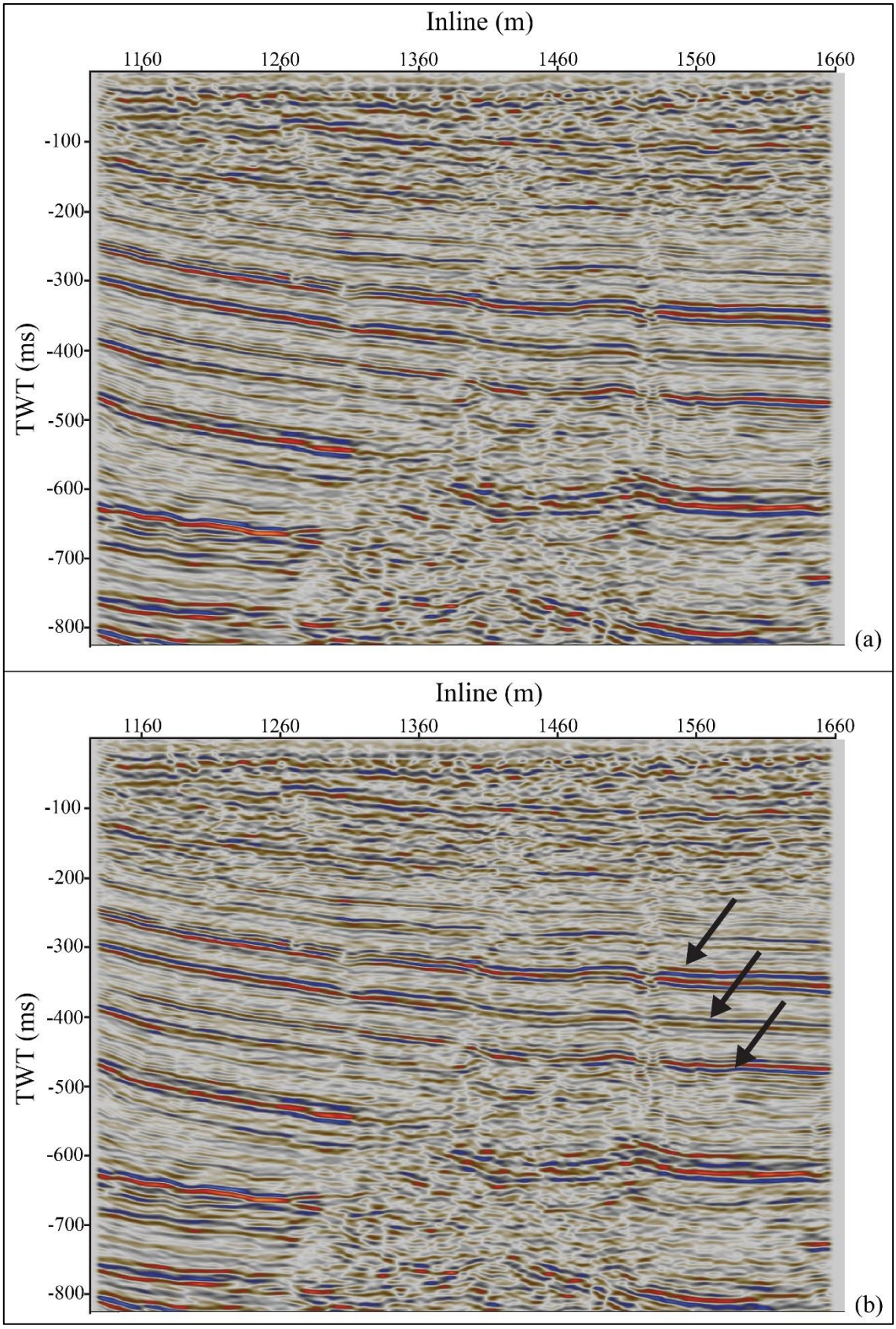

Figure 5.5*. Crossline 5780 shows (a) the original seismic section and (b) the structurally smoothed section. The structural smoothing filter shows high signal-to-noise ratio than the original section making it easier to see the horizons (shown with the arrows).*

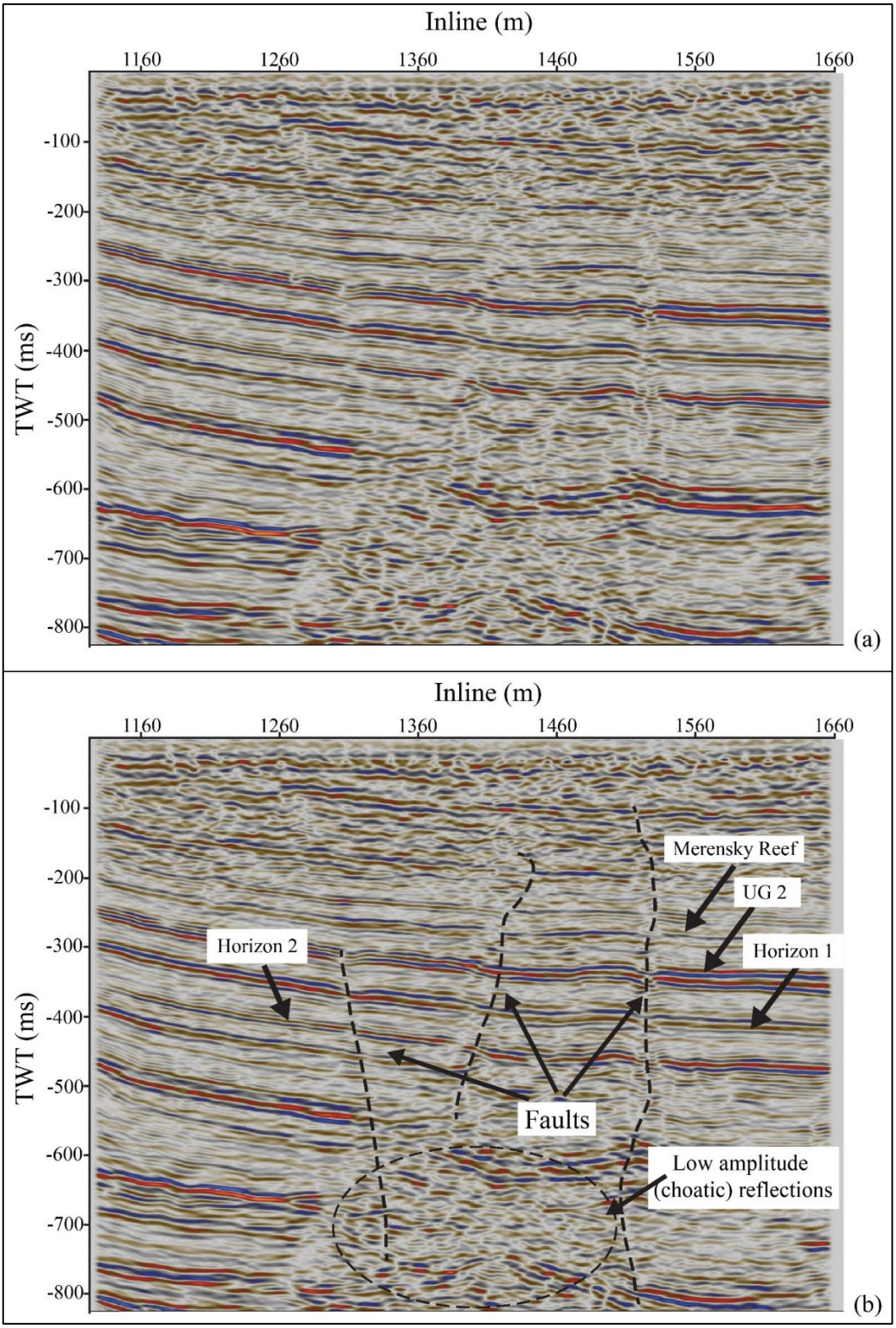

Figure 5.6*. Crossline 5780 after the application of the structural smoothing volumetric attribute and (a) in the uninterpreted section and (b) the section after interpretation. The structural smoothing attribute highlighted four strong seismic reflections (the first two being the Merensky Reef and the UG-2). The horizons are being cross-cut by three vertical discontinuities. The structural smoothing attribute also revealed an area with low-amplitude chaotic reflectors, located in the central region between 500 and 800 ms of the section.*

5.3.2 Chaos

As mentioned earlier, chaos attribute measures the lack of organisation (e.g. where the seismic signature varies significantly) in the estimated dip and dip azimuth within the data (Koson et al., 2014). Figures 5.7b, 5.8 and 5.9b show the effectiveness of the chaos attribute at highlighting low amplitude reflections and large variations in the reflections when compared to the original seismic section (Figures 5.7a, and 5.9a). The chaos attribute (Figure 5.8) is scaled from 0 to 1: (i) values > 0.50 are represented by red colours and are mainly caused by strong variation in the estimated dip and dip azimuth in the data. These values may represent highly dipping seismic events, which could be associated with faults; and (ii) values from 0 to 0.50 are represented by white and black/grey colours and indicate small variations of dip and dip azimuth mainly caused by potholes or subtle faults and fractures. Also, values presented by white colours may correspond to areas with no evidence of strong variation in dip and dip azimuth. Normally, these areas are associated with horizontally layered stratigraphy that exhibits no variations in the seismic amplitude. This attribute has the ability to detect chaotic regions within seismic data, thus it can highlight areas of disruptions along the seismic horizons. Figure 5.8 also demonstrates how chaos attributes highlight discontinuities (indicated as red dashed lines) within the seismic section (at -400 ms and reaching -750 ms, with chaos of 0.50 to 0.80).

In addition, the chaos attribute shown in Figure 5.10 has delineated layers of low chaos (0 to 0.20), representative of the horizons, that are intercepted by two vertical structures of chaos between 0.50 and 1.00, which are interpreted as faults.

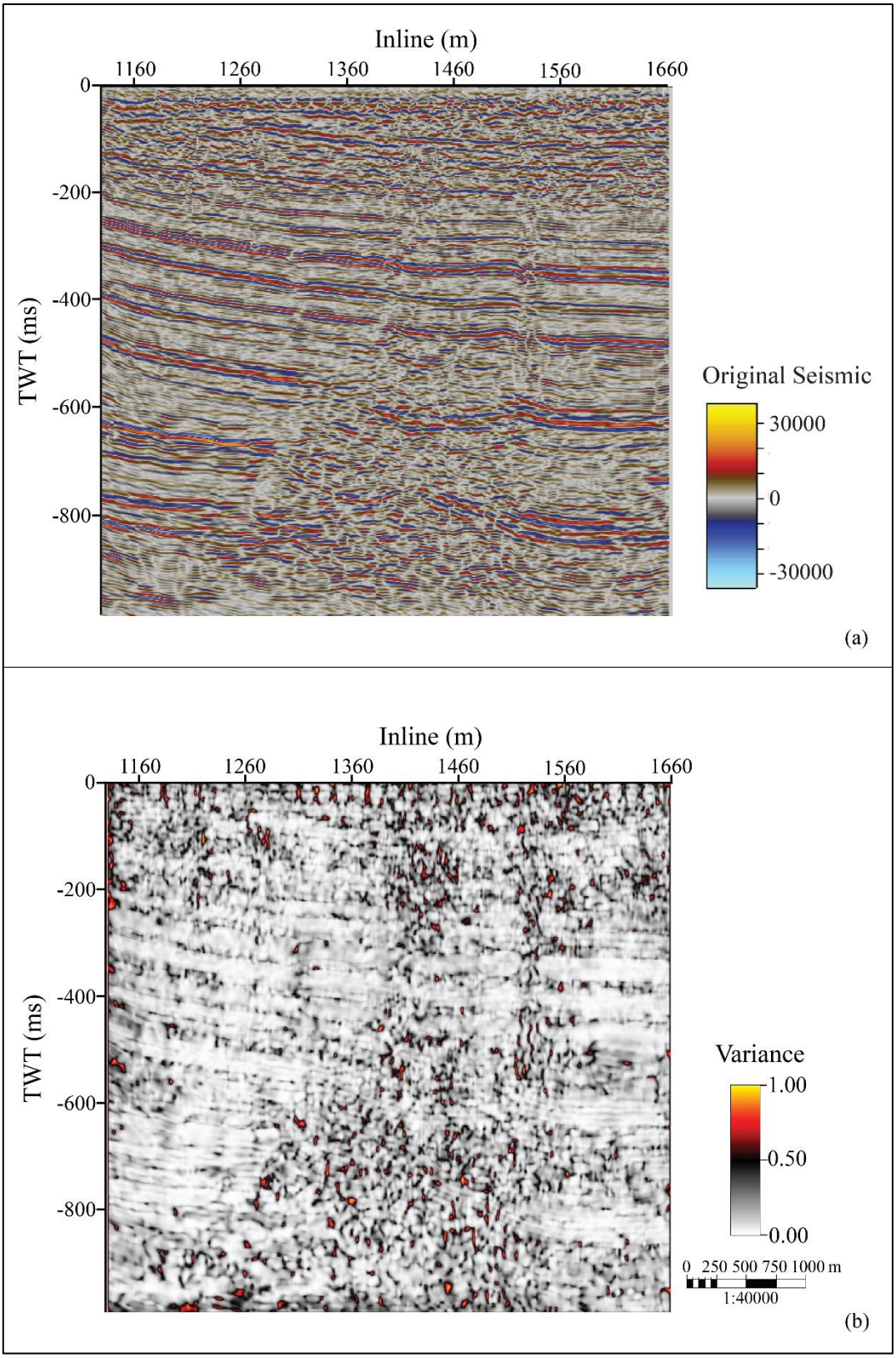

Figure 5.7*. Crossline 5780 (a) before the application of the chaos attribute and (b) after the application of the chaos attribute. Note here that the chaos attribute highlights low amplitude reflections and large variations in the reflections effectively when compared to the original seismic section (a).*

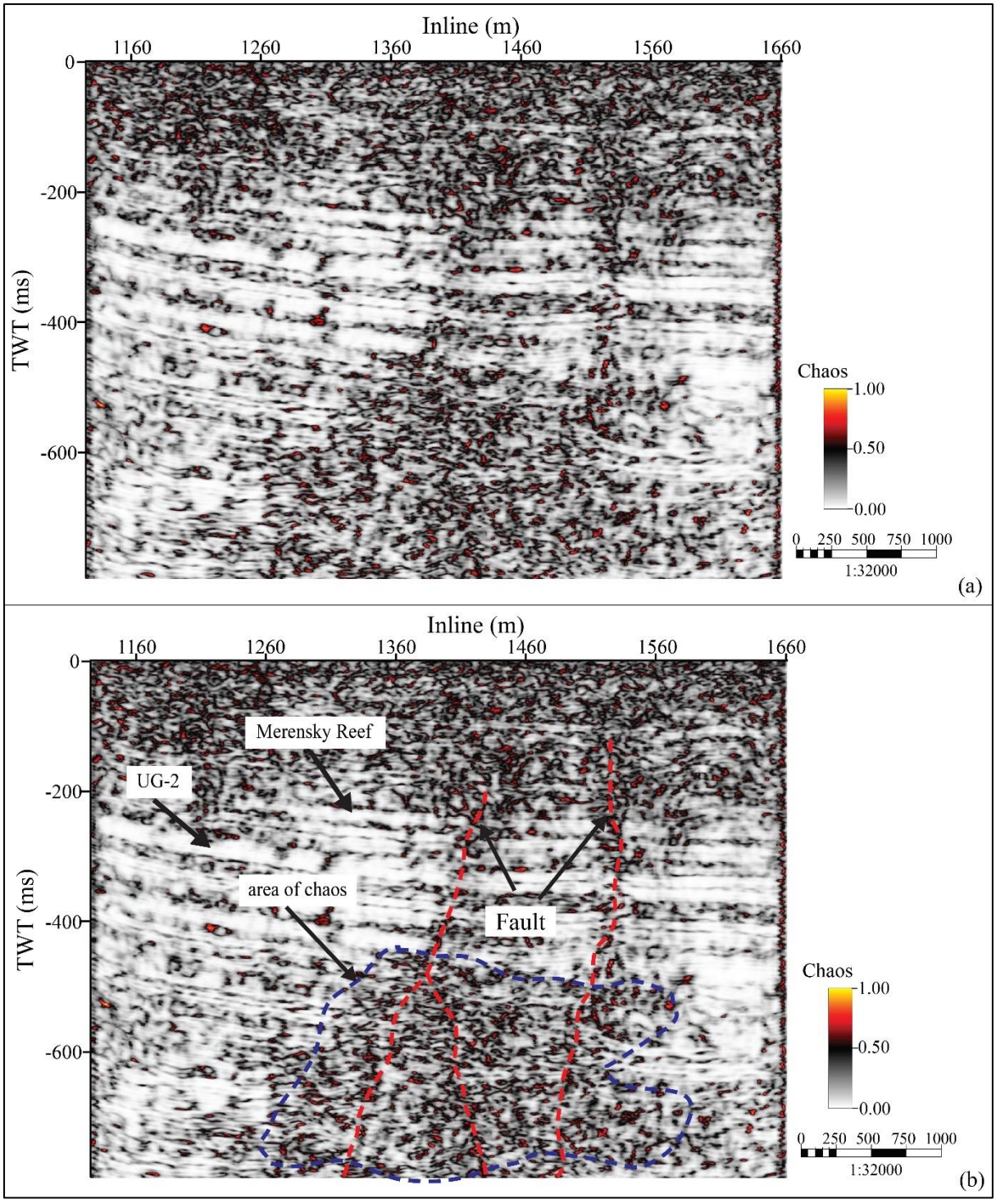

***Figure 5.8**. Crossline 5780 (a) uninterpreted and (b) interpreted. The chaos attribute is able to highlight two discontinuities (indicated as red dashed lines) within the seismic section (at -400 ms and reaching -750 ms, with chaos of 0.30 to 0.80). The attribute has also managed to delineate layers of low chaos (0 to 0.20) that are intercepted by two vertical structures of chaos between 0.50 and 1.00 as well as an area of high chaos (highlighted by the blue dashed line).*

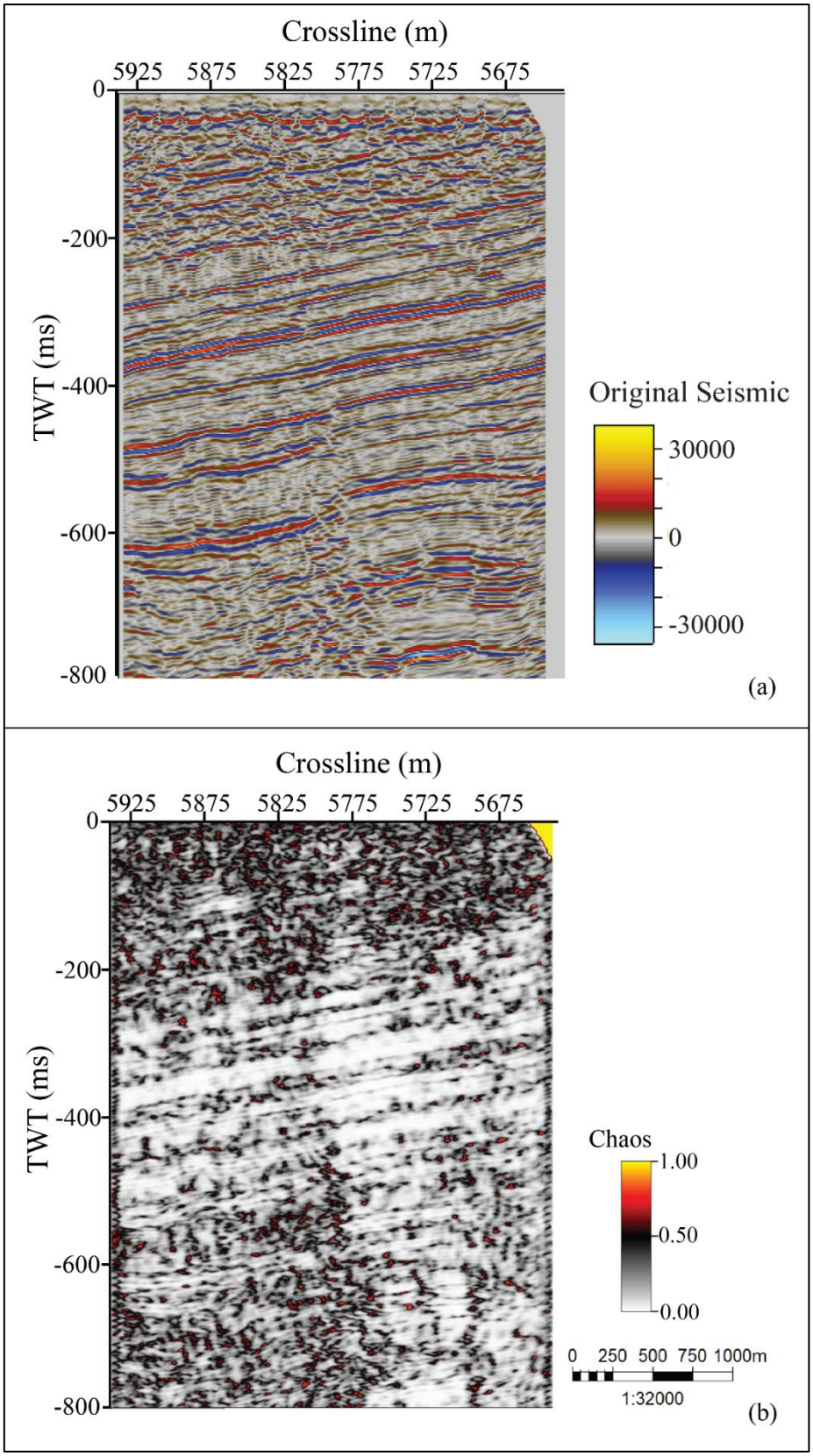

Figure 5.9. *Inline 1331 (a) before the application of the chaos attribute and (b) after the application of the chaos attribute. The chaos attribute highlights low amplitude reflections and large variations in the reflections effectively when compared to the original seismic section (a).*

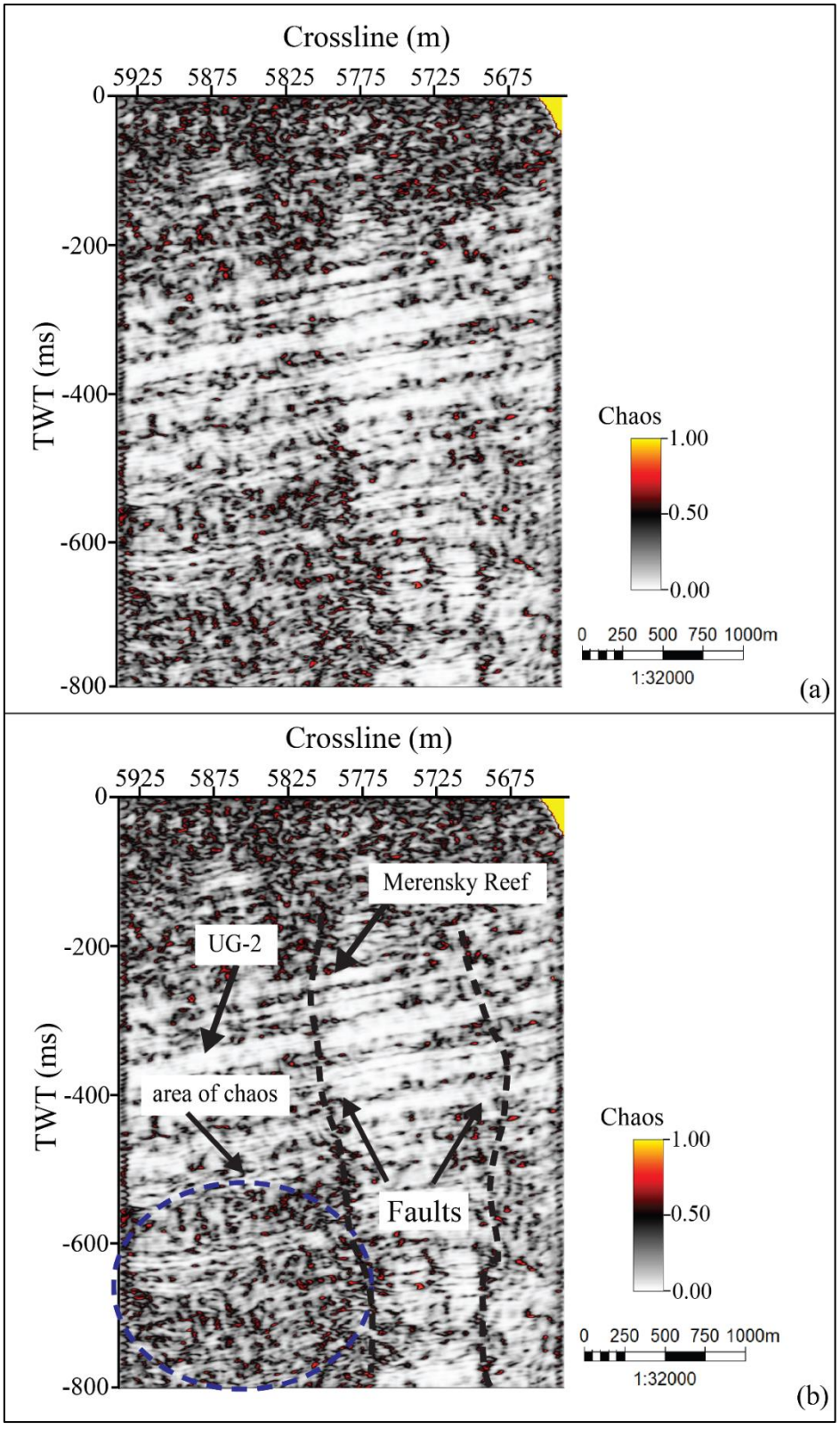

***Figure 5.10**. Inline 1331 (a) uninterpreted and (b) interpreted. The chaos attribute is able to highlight two discontinuities (indicated as red dashed lines) within the seismic section (at -400 ms and reaching -750 ms, with chaos of 0.30 to 0.80). The attribute has also managed to delineate layers of low chaos (0 to 0.20) that are intercepted by two vertical structures of chaos between 0.50 and 1.00 as well as an area of high chaos (highlighted by the blue dashed line).*

5.3.3 Variance

The variance attribute is the opposite of coherency. Figures 5.11, 5.12 and 5.13 show how the variance attribute enhances the areas with no coherency within the seismic volume. The variance attribute measures lateral variations of the seismic signal within the data, which can be related to geological features such as faults, potholes and horizons. In particular, dissimilarities of the signal along the seismic horizon caused by potholes and major faulting can be emphasized by variance attribute. In short, variance attribute enhances edges within the seismic data (Koson et al., 2014).

The variance attribute shown in Figure 5.12 highlights horizontal layers with a low variance of 0.0 – 0.3. These low variance layers are intercepted by a steeply dipping event (shown by red dashed lines) that have a higher variance that ranges from 0.5 to 0.8 (also see Figure 5.14). In both Figures 5.12 and 5.14, an area of high variance (variance value: 0.3 at 0.8; TWT: -600 ms to -800 ms) is observed. This degree of faulting along the seismic horizons cannot be observed on the original data (Figure 5.11a and 5.13a). Most importantly, these near-vertical features cross-cut both the MR and UG-2 which is important for future mine and planning and designs.

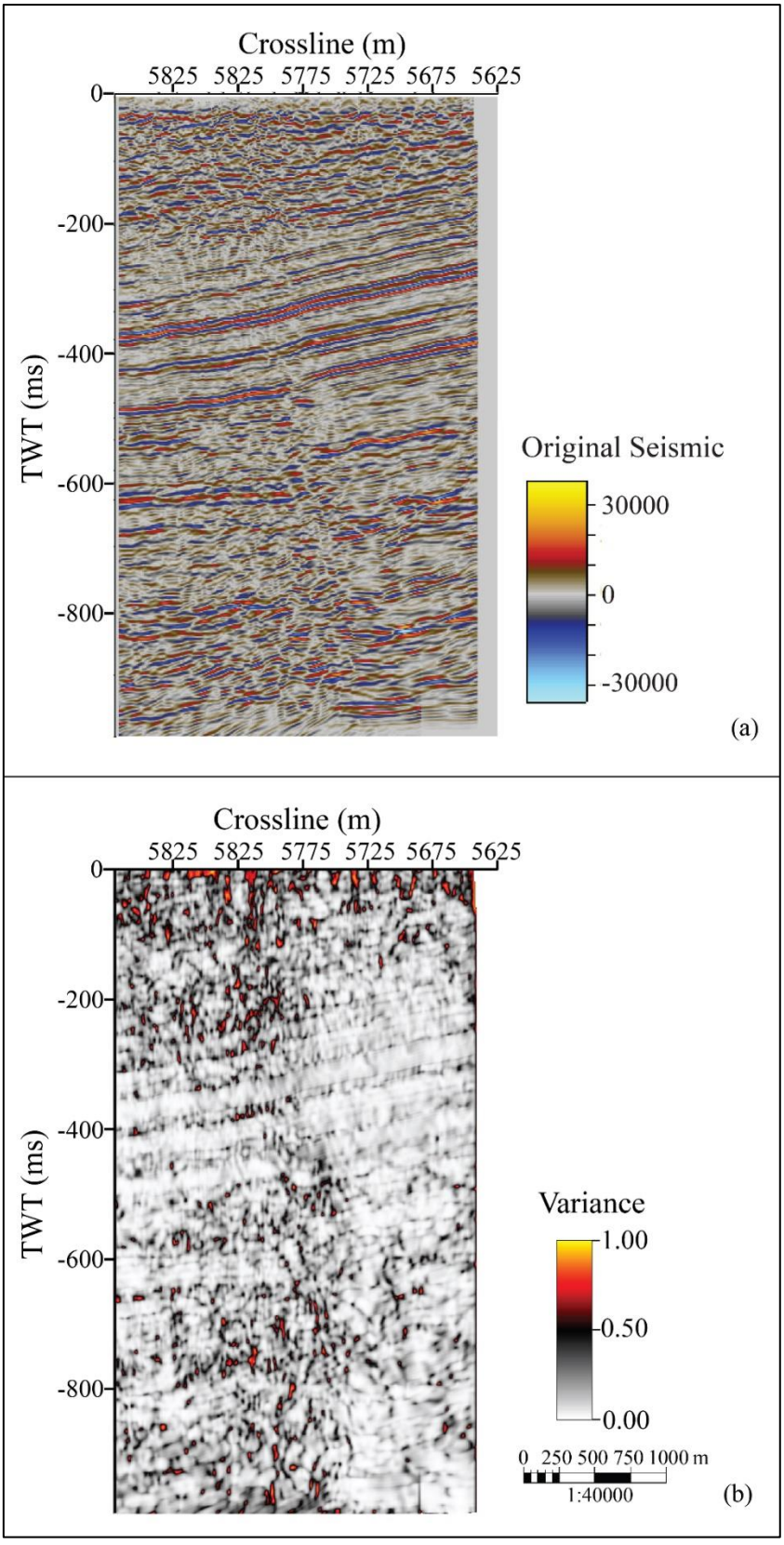

Figure 5.11. *Inline 1391 (a) before the application of the variance attribute and (b) after the application of the variance attribute. The variance attribute highlights low amplitude reflections and the lack of coherency in the reflections when compared to the original seismic section (a).*

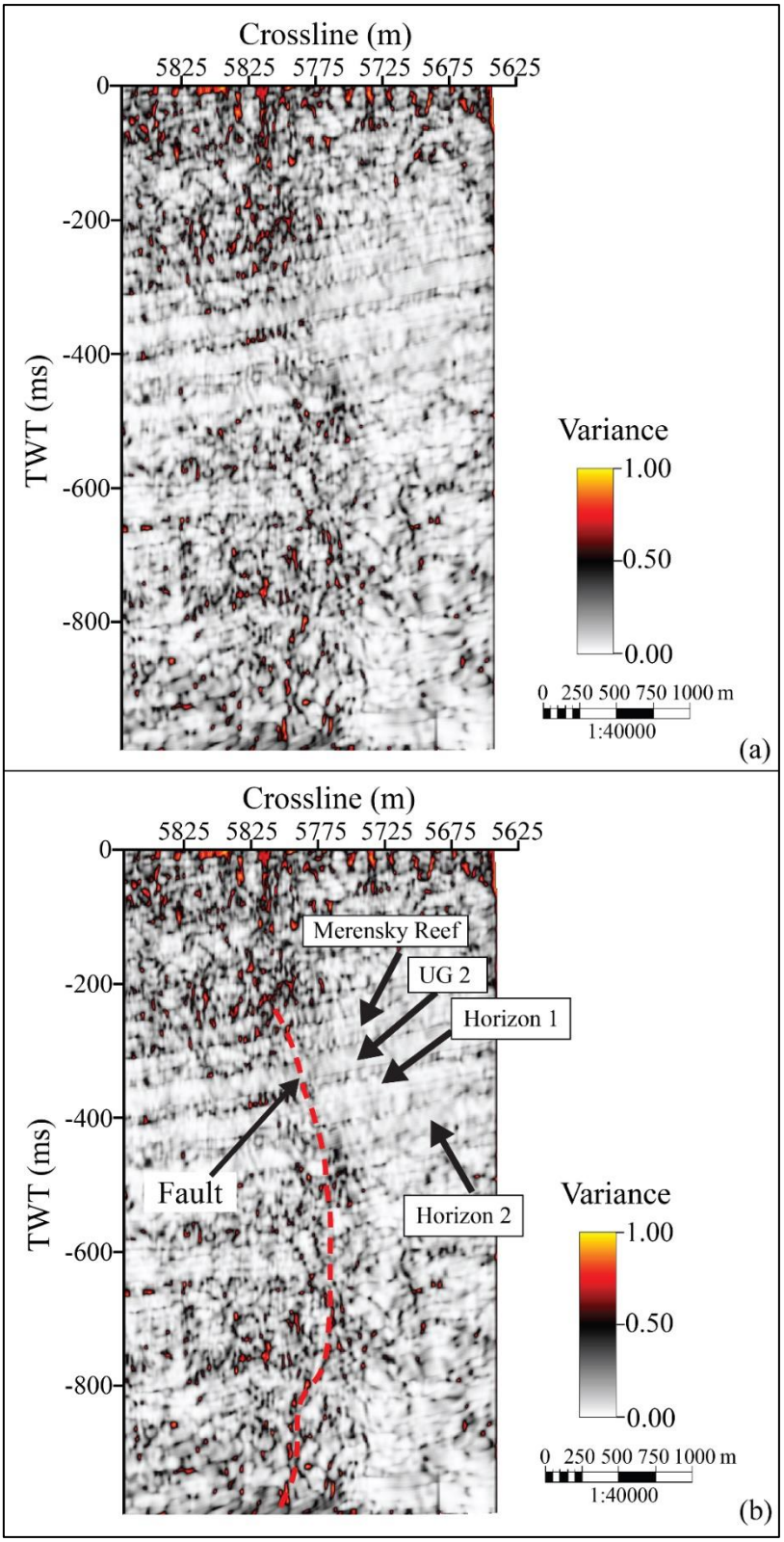

***Figure 5.12**. Application of the Variance attribute. Inline 1391 displays (a) Uninterpreted section; (b) the interpreted section. This attribute highlights horizontal layers with a low variance of 0.0 – 0.3. These low variance layers are intercepted by a steeply dipping event (shown by red dashed lines) that have a higher variance that ranges from 0.5 to 0.8.*

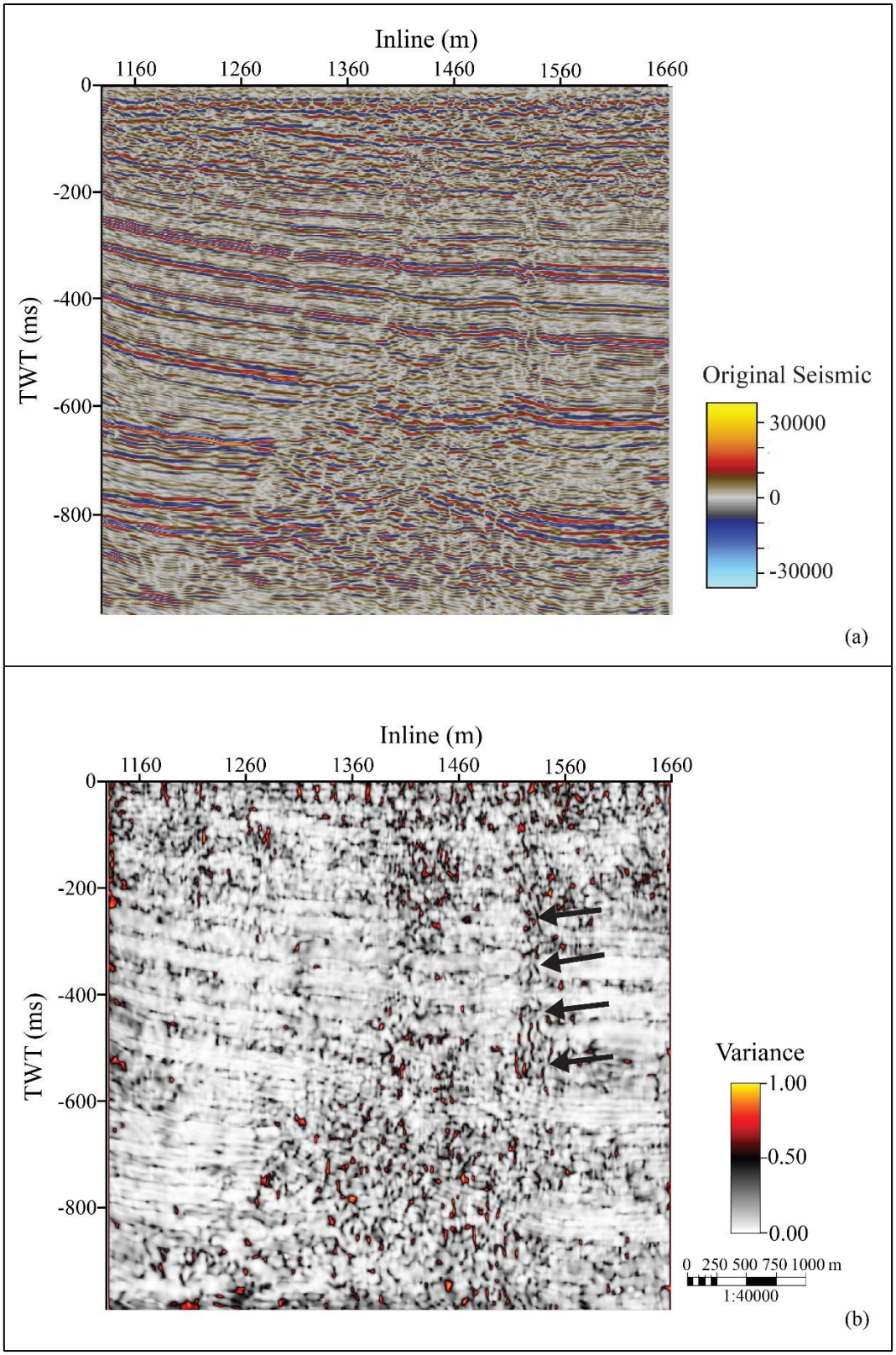

Figure 5.13*. Crossline 5780 (a) before the application of the variance attribute and (b) after the application of the variance attribute. The variance attribute highlights low amplitude reflections and the lack of coherency in the reflections when compared to the original seismic section (a). The degree of faulting along the seismic horizons seen in b cannot be observed on the original data (a) (see arrows).*

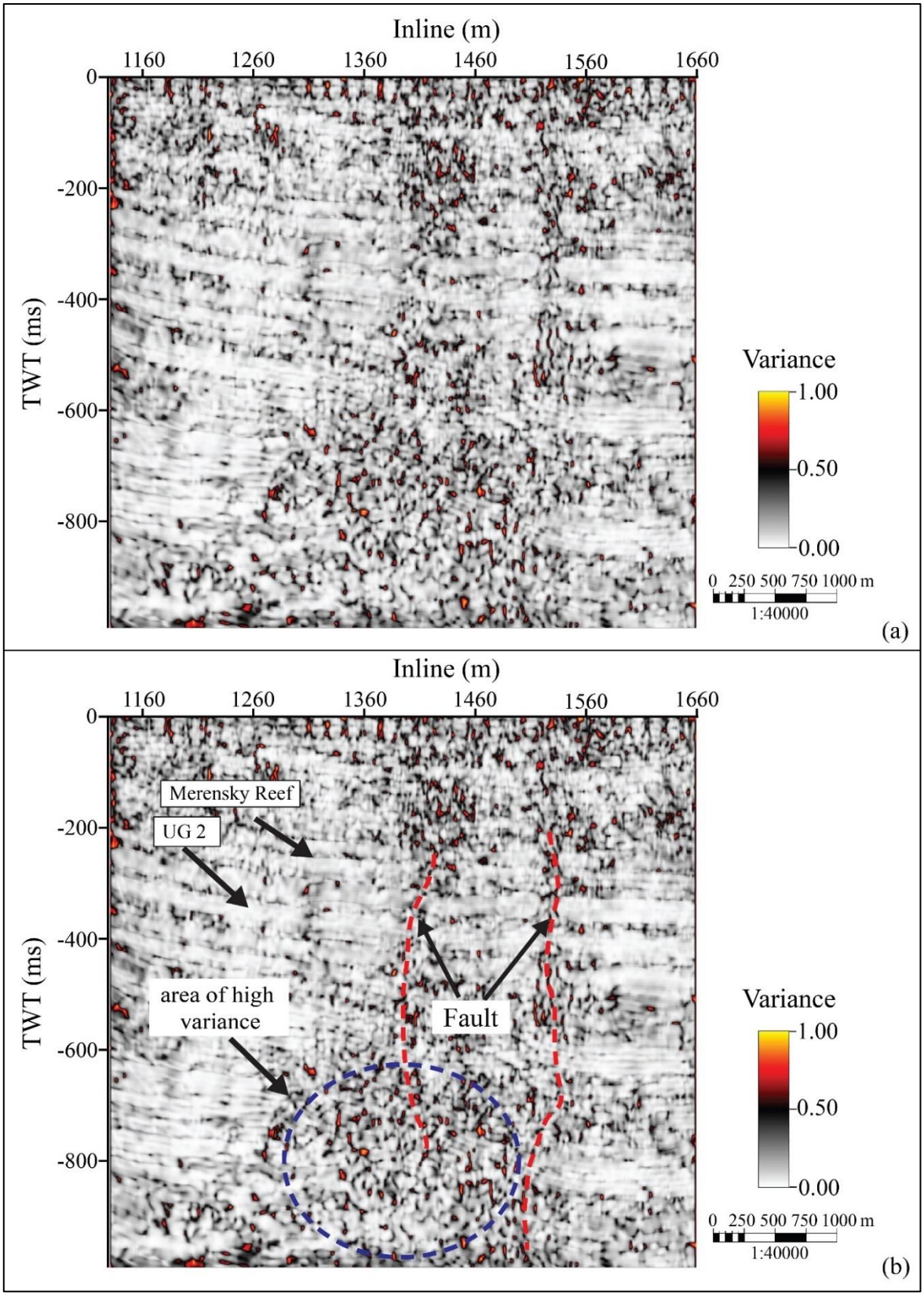

***Figure 5.14**. Application of the variance attribute. Crossline 5780 displays: (a) Uninterpreted section; (b) the interpreted section. An area of high variance (variance value: 0.3 at 0.8) at TWT -600 ms to -800 m is observed in the section. The identified near-vertical features (shown by the red dashed lines) cross-cut both the MR and UG-2.*

5.4 COMBINED CONFIDENCE CLASSIFICATION METHOD

The combined confidence classification method (Figures 5.15 and 5.16) was applied to the UG-2 and Merensky Reef (MR) horizon; red to blue colours represent high (less structurally complex) to low confidence (high structurally complex) level, respectively. The surface was then smoothed using the average method (combination of the mean and median filters). The UG-2 (Figure 5.15) shows that the interpretation confidence level is higher in the western region of the horizon when compared to the eastern region. For the MR horizon, however, the confidence level is higher in the eastern than in the western region (Figure 5.16). Both horizons show good delineation of a distinct north-northwest trending fault represented as a linear feature with low confidence zone.

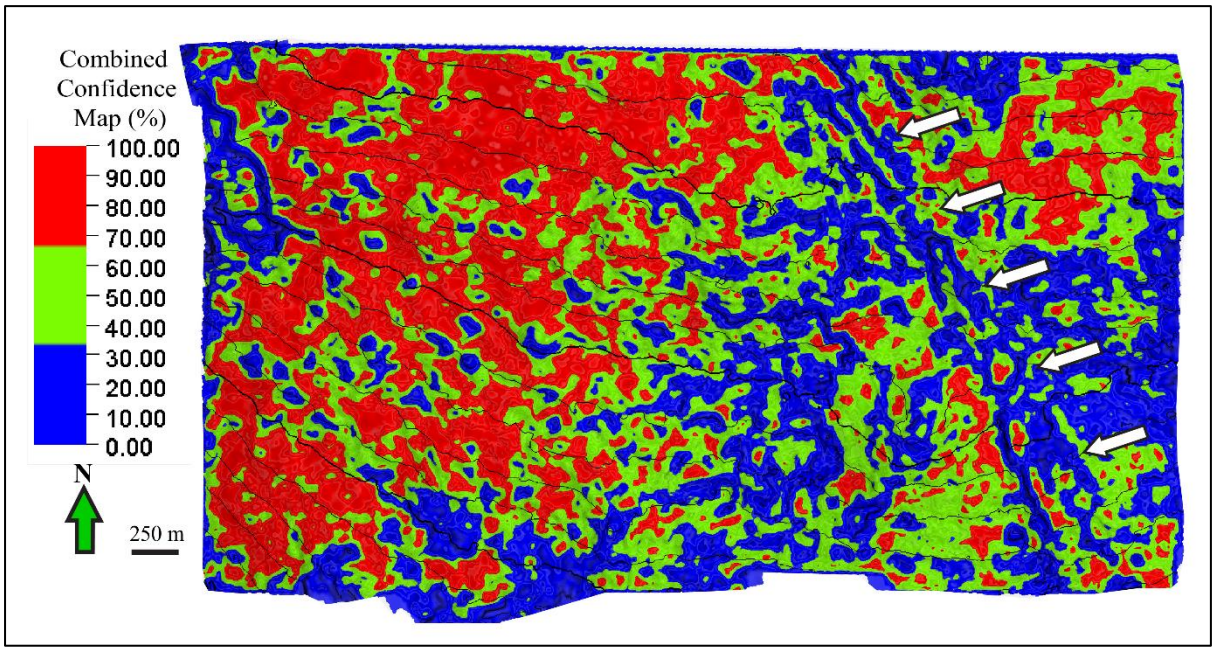

***Figure 5.15**. Combined confidence map of the UG-2. Here red to blue colours represent high (less structurally complex) to low confidence (high structurally complex) level, respectively. Interpretation confidence level is higher in the western region of the horizon when compared to the eastern region. The map was able to delineate a linear feature in the low confidence zone (highlighted with the white arrows).*

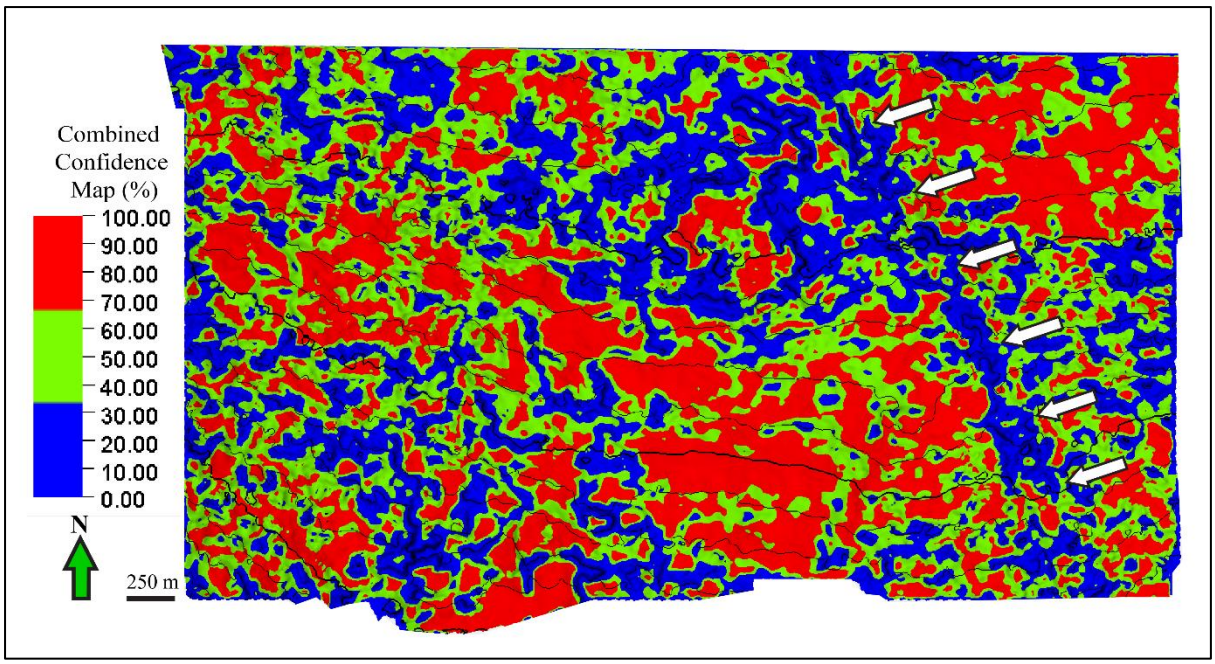

***Figure 5.16**. Combined confidence map of the Merensky Reef. Here red to blue colours represent high (less structurally complex) to low confidence (high structurally complex) level, respectively. Interpretation confidence level is higher in the eastern than in the western region. The map was able to delineate a linear feature in the low confidence zone (highlighted with the white arrows).*

5.5 HORIZON-BASED ATTRIBUTES

Horizon-based attributes were applied to both the UG-2 and the Merensky Reef horizons. These include RMS amplitude, dip, dip azimuth, edge detection and minimum curvature.

5.5.1 Application of horizon-based attributes on the UG-2

The UG-2 RMS amplitude map (Figure 5.17) exhibits a fault with high RMS amplitude values that ranges from 17 500 to 22 500 that trends north-northwest (marked by white arrows); this fault is consistently revealed by all applied attributes. For example, this fault is also mapped in the (i) dip attribute map (Figure 5.18) with an approximately dip value of 7°; (ii) dip azimuth attribute map (Figure 5.19) (although it is not as prominent as in other attributes) with a value of 250°; (iii) edge detection map (Figure 5.20) with a value of 10%; and (iv) minimum curvature map (Figure 5.21) with a value ranging from -0.03 to -0.06. Furthermore, the RMS amplitude attribute reveals bright spots or amplitude anomalies on the map with low amplitude

values ranging from 0 – 5 000 (square in Figure 5.17). Additionally, on the edge of the UG-2 RMS map and on the left side of the fault (circles in Figure 5.17) there is a change in the contour lines from almost horizontal to curved suggesting a change in topography, and the areas exhibit amplitude values that range from 5 000 to 12 500.

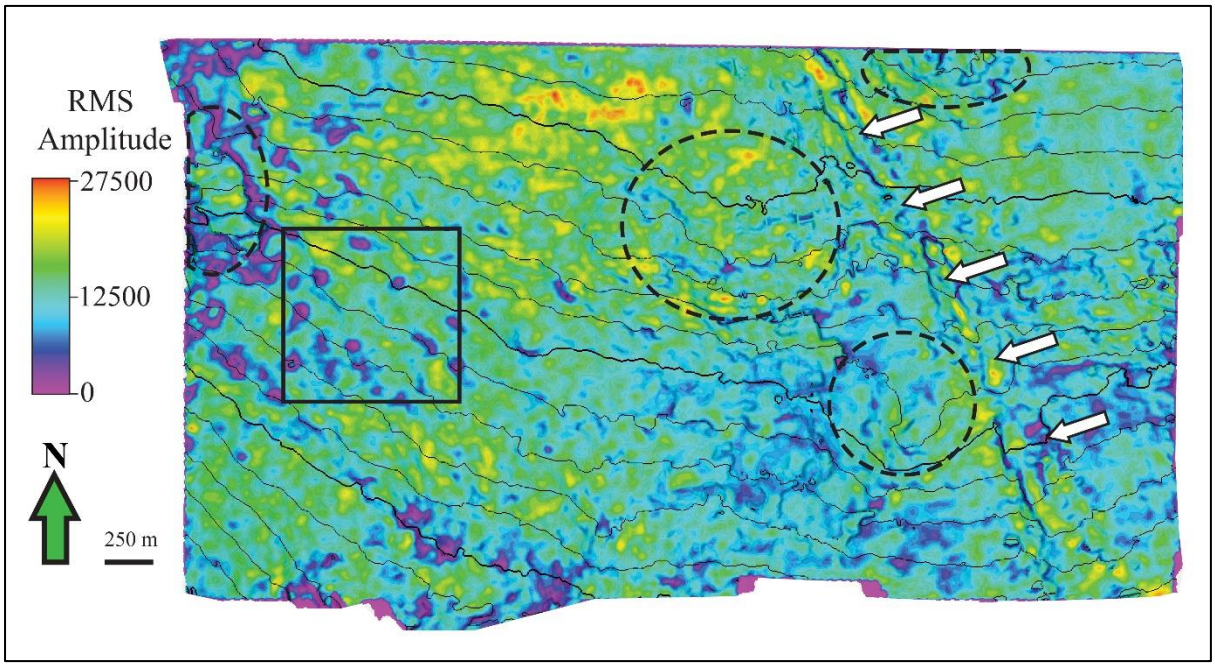

***Figure 5.17**. UG-2 after the application of the RMS Amplitude attribute highlighting a linear feature (arrows), bright spots (square) and changes in contour lines and low amplitudes (circles).*

From the UG-2 dip attribute map, the horizon is characterised by small dip values ranging between 5° and 6°. The dip attribute also shows mapping of large areas (marked as white circles in Figure 5.18) with slightly higher dip values (7° - 8°) as compared to the rest of the horizon and similar changes in the contour lines as in RMS amplitude map are also observed. However the dip attribute map does not enhance the smaller potholes.

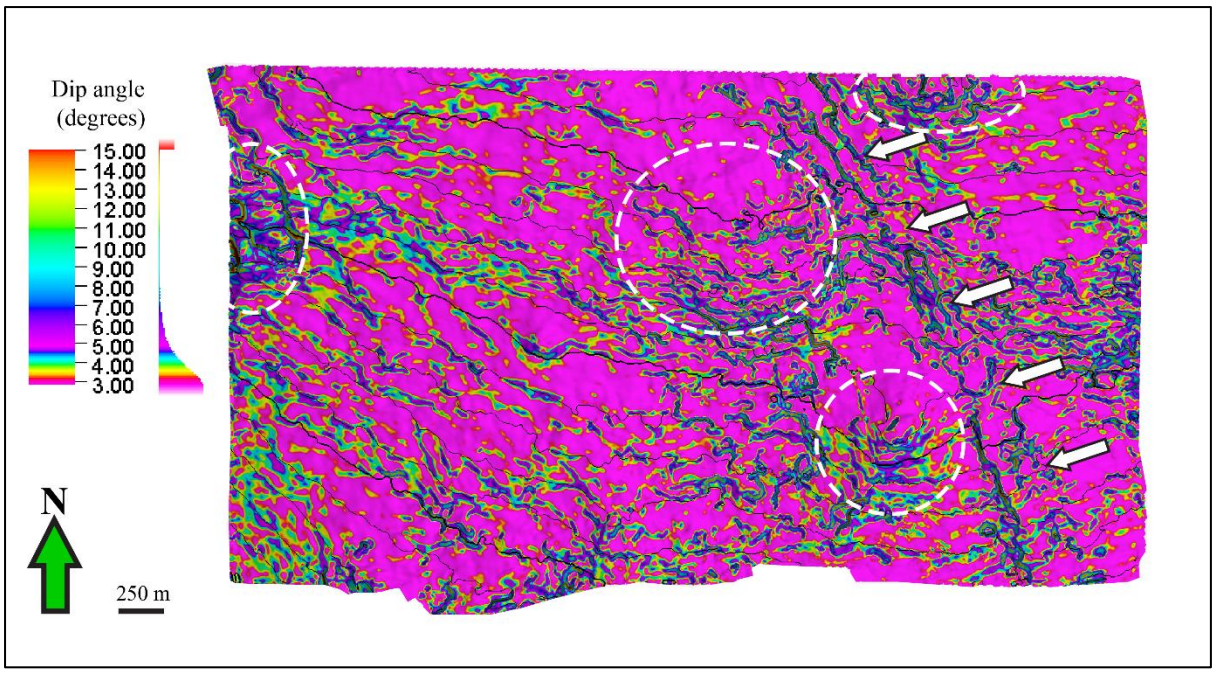

***Figure 5.18**. UG-2 after the application of the dip attribute highlighting a linear feature (arrows) and changes in contour line and low dip angles (circles).*

In the UG-2 dip azimuth map, the western region is dominated by low dip azimuth values ranging from 0° to 75°, while the eastern region has higher values ranging from 150° to 325° and uncommon low dip azimuth values (Figure 5.19). This attribute was unable to highlight any small circular features.

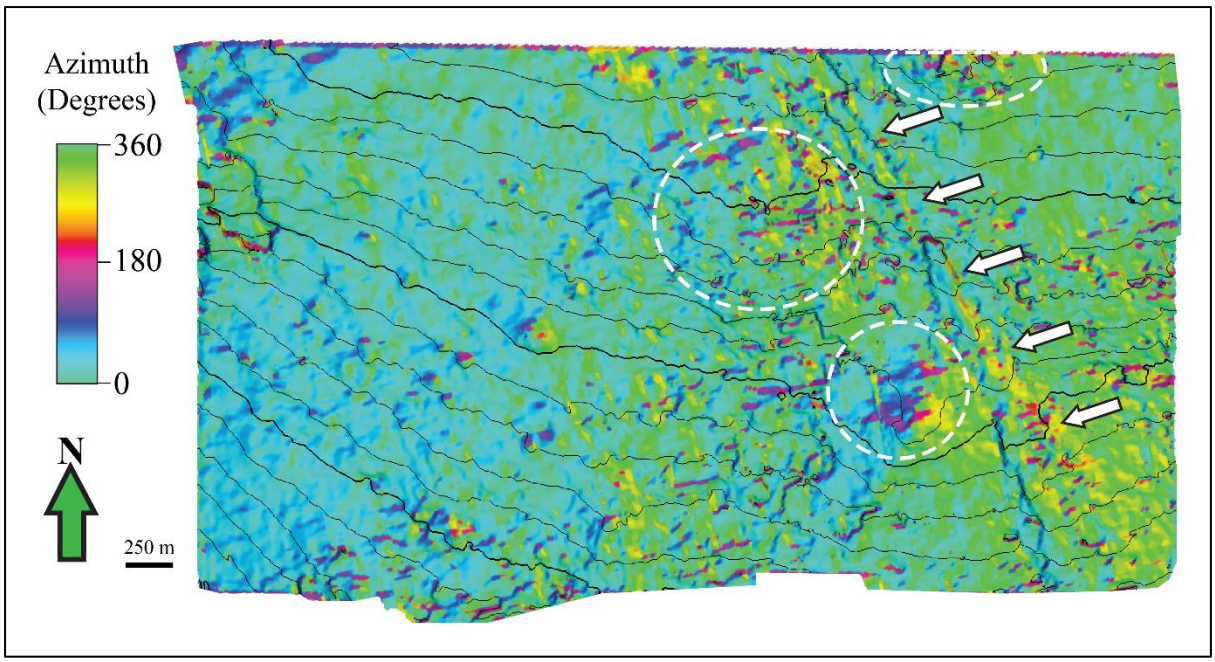

***Figure 5.19**. UG-2 after the application of the dip azimuth attribute highlighting a linear feature (arrows) and changes in contour line and low dip azimuth (circles).*

The edge detection attribute shows circular features throughout the horizon, which are interpreted as pothole structures. The edge detection attribute highlights potholes (indicated by white circles) by showing a rim of low percentage (10% – 25%) followed by higher percentages (60% – 80%) in the middle of the study area. However, the larger circular features or potholes are often found to display lower percentages in the middle as opposed to the smaller ones (Figure 5.20). This could be suggestive of the mechanism that formed the potholes.

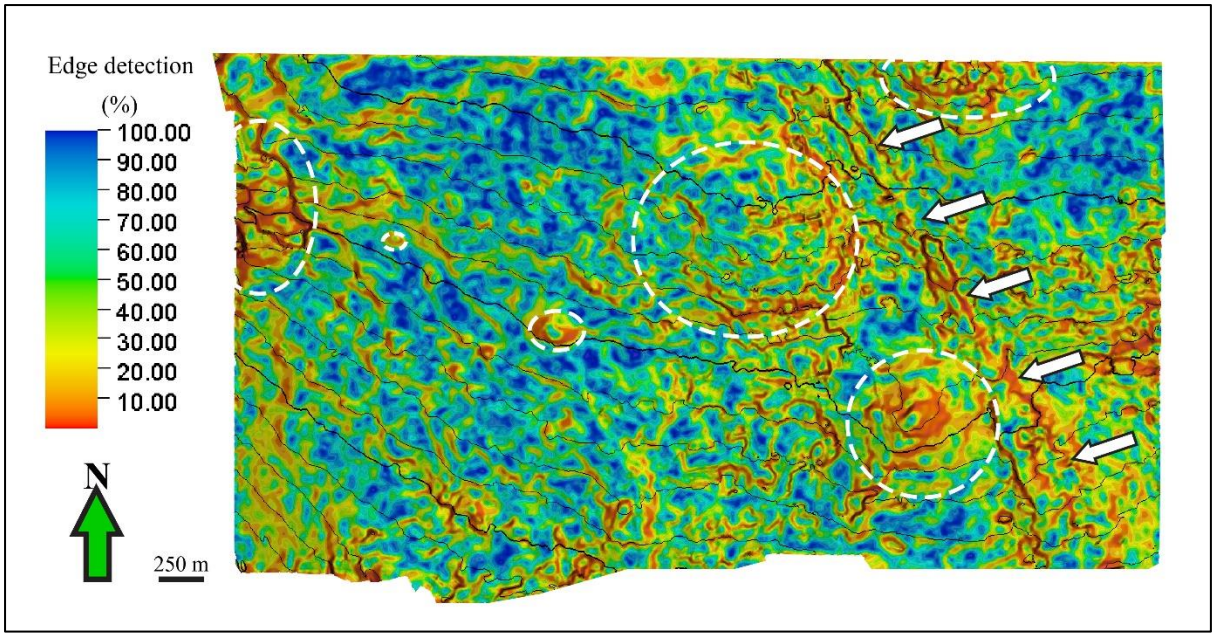

***Figure 5.20**. UG-2 after the application of the edge detection attribute highlighting a linear feature (arrows) and changes in contour line and a circular rim of low percentages with higher percentages in the middle(circles).*

A closer inspection at the minimum curvature attribute map shows that the map exhibits a minimum curvature that ranges from 0.00 to -0.06. The same potholes (indicated as black circles) identified in the other attributes (e.g. dip, dip azimuth and edge detection attributes) are also highlighted in the minimum curvature attribute as bright red spots on the horizon (Figure 5.21). The minimum curvature attribute has been able to highlight not only the large slumping areas but also the smaller slumping areas. These areas exhibit low values (-0.01 to -0.06) on the minimum curvature map.

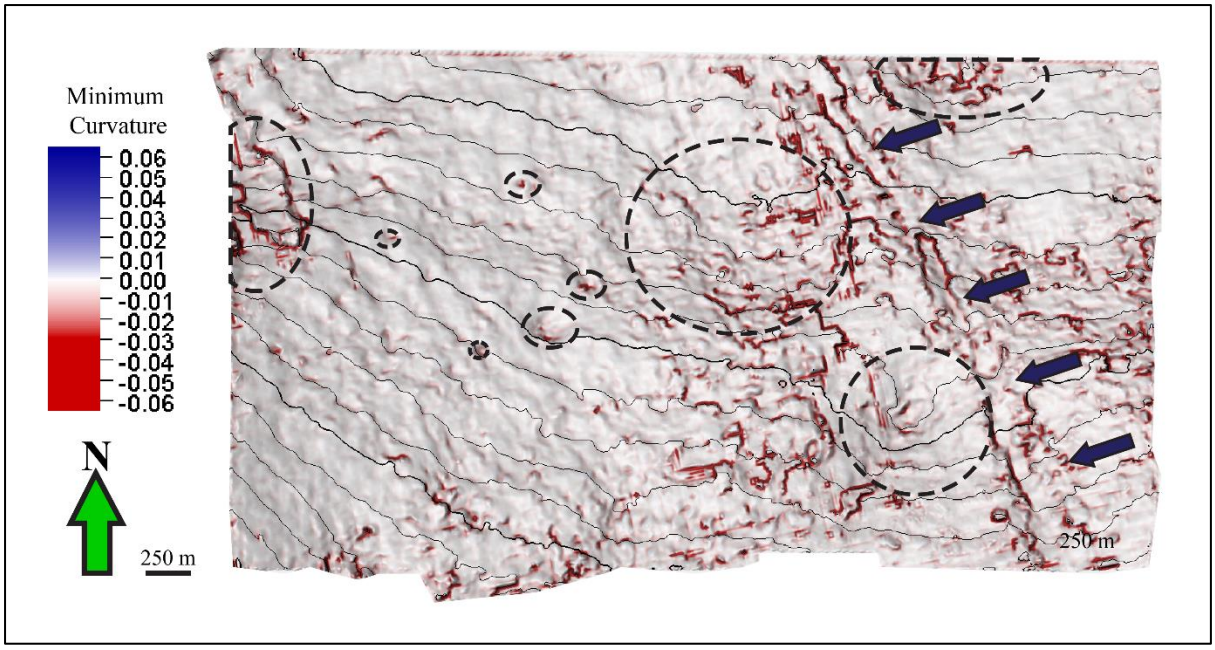

Figure 5.21. *UG-2 after the application of the minimum curvature attribute highlighting a linear feature (arrows), bright spots (small circles) and changes in contour line and low curvature values(circles).*

5.5.2 Application of horizon-based attributes to the Merensky Reef

After the application of the RMS amplitude attribute (Figure 5. 22) to the Merensky Reef, the map shows the mapping of a dominant, north-northwest trending fault represented as a linear feature (marked in white arrows) that cuts through the study area. This linear feature is consistently observed in all the other attributes applied to the Merensky Reef. On the dip attribute map (Figure 5.23), it exhibits a value of 7.5°; on the dip azimuth attribute map (Figure 5.24), it exhibits a value of 230°; on the edge detection map (Figure 5.25), it is dominated by a value of 10%; and on the minimum curvature map (Figure 5.26), it is characterized by values ranging from -0.03 to -0.06. On the north-western part of the fault, slump features (herein interpreted as potholes); these slump features are also associated with a change in contour lines (indicated as black dashed lines).

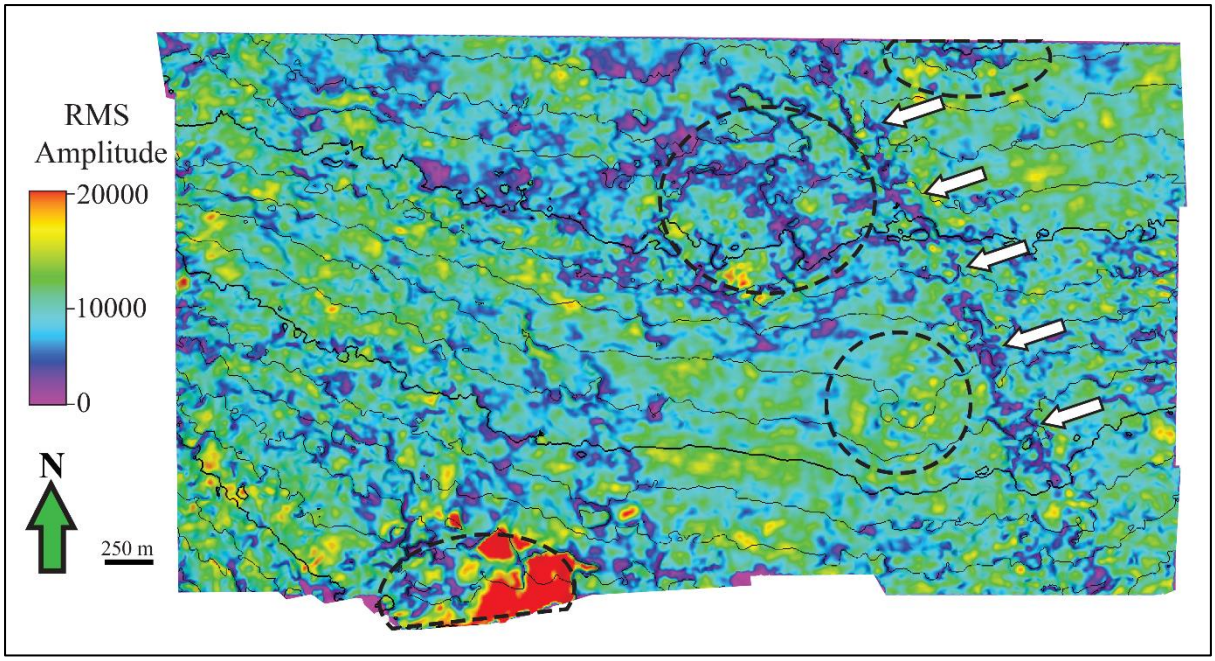

***Figure 5.22**. Merensky Reef after the application of the RMS Amplitude attribute highlighting a linear feature (arrows) and changes in contour line and low amplitudes (circles).*

The dip attribute map of the Merensky Reef shows that the horizon is dominated by low dip values, ranging between 5° and 6°. The dip attribute also shows good mapping of large areas (marked circles in Figure 5.23) with slightly higher dip values (7° - 8°) as compared to the rest of the horizon; this is also highlighted by the change in contour lines seen on the map.

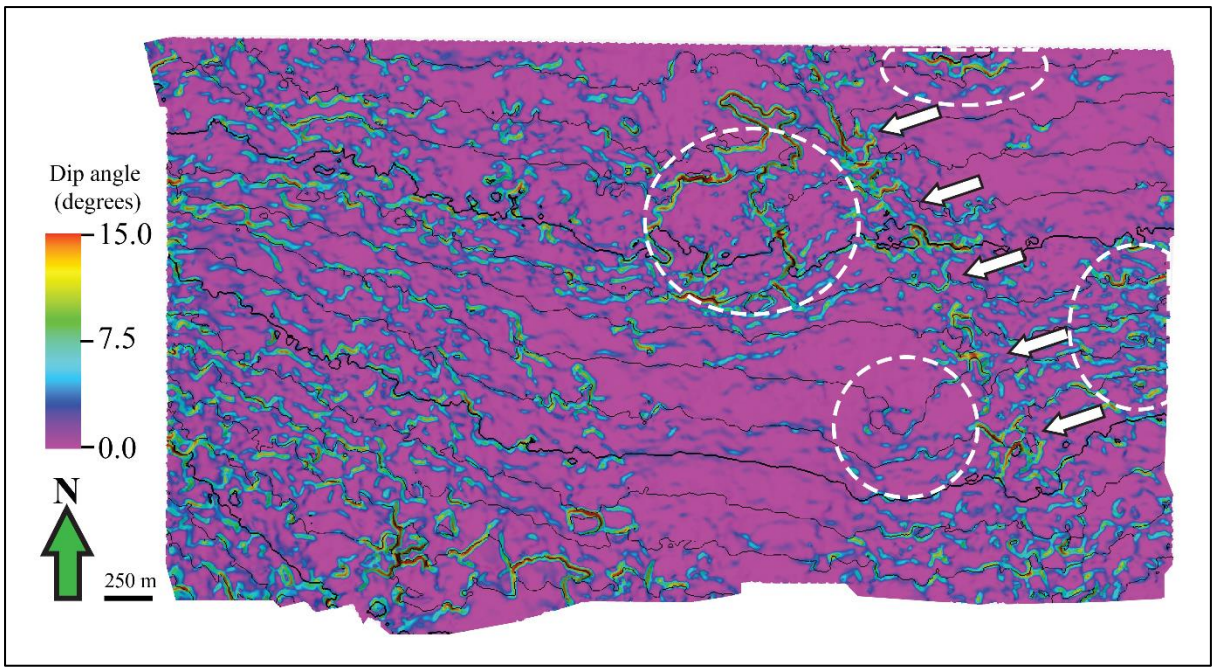

***Figure 5.23**. Merensky Reef after the application of the dip attribute highlighting a linear feature (arrows) and changes in contour line and low dip angles (circles).*

On the dip azimuth map, the area is generally dominated by high dip azimuth values ranging from 300° to 360°. However, the southwest region is characterized by low dip azimuth values ranging from 0° to 75°. The dip azimuth map also shows good mapping of three large slumping areas (or potholes) (indicated by white dashed lines) with values ranging from 180° to 230° (Figure 5.24).

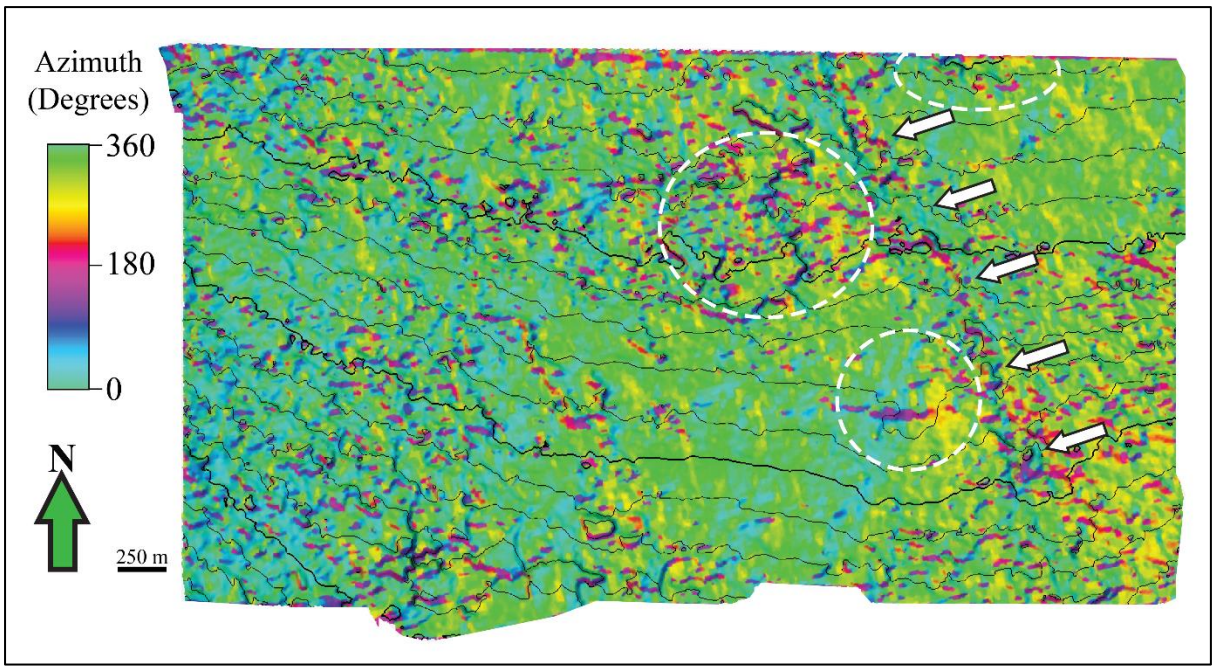

***Figure 5.24**. Merensky Reef after the application of the dip azimuth attribute highlighting a linear feature (arrows) and changes in contour line and low dip azimuth (circles). The map is dominated by dip azimuth values ranging from 180° to 360°).*

On the edge detection attribute map, the Merensky Reef is dominated by low percentages with areas of higher percentages in the central region. The attribute highlights the irregularity or structurally complexity of the Merensky Reef. Most importantly, the map exhibits a dominant north-northwest trending fault (indicated by arrows) and semi-to circular potholes (indicated as white dashed lines) (Figure 5.25).

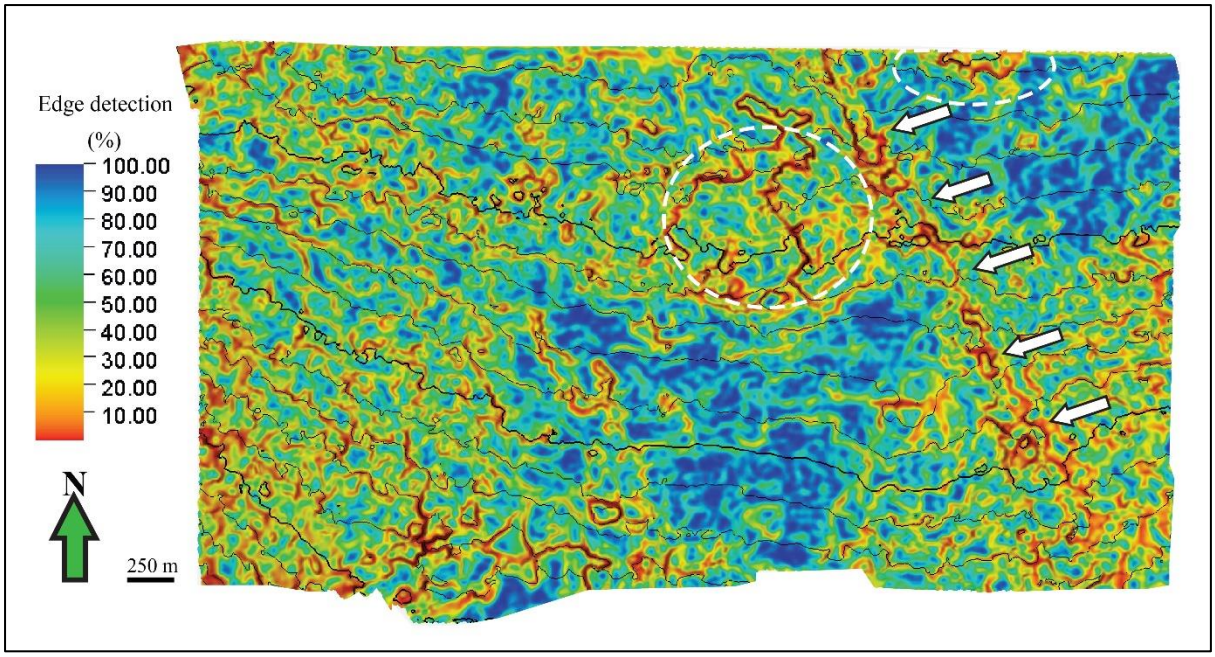

***Figure 5.25**. Merensky Reef after the application of the edge detection attribute highlighting a linear feature (arrows) and changes in contour line and a circular rim of low percentages with higher percentages in the middle(circles).*

On the minimum curvature attribute map, the minimum curvature ranges from 0.00 to -0.06 (Figure 5.26). The minimum curvature attribute shows high resolution detection of the larger slump structures (> 300 m in diameter) within the horizon but fails to enhance the smaller ones (< 300 m in diameter).

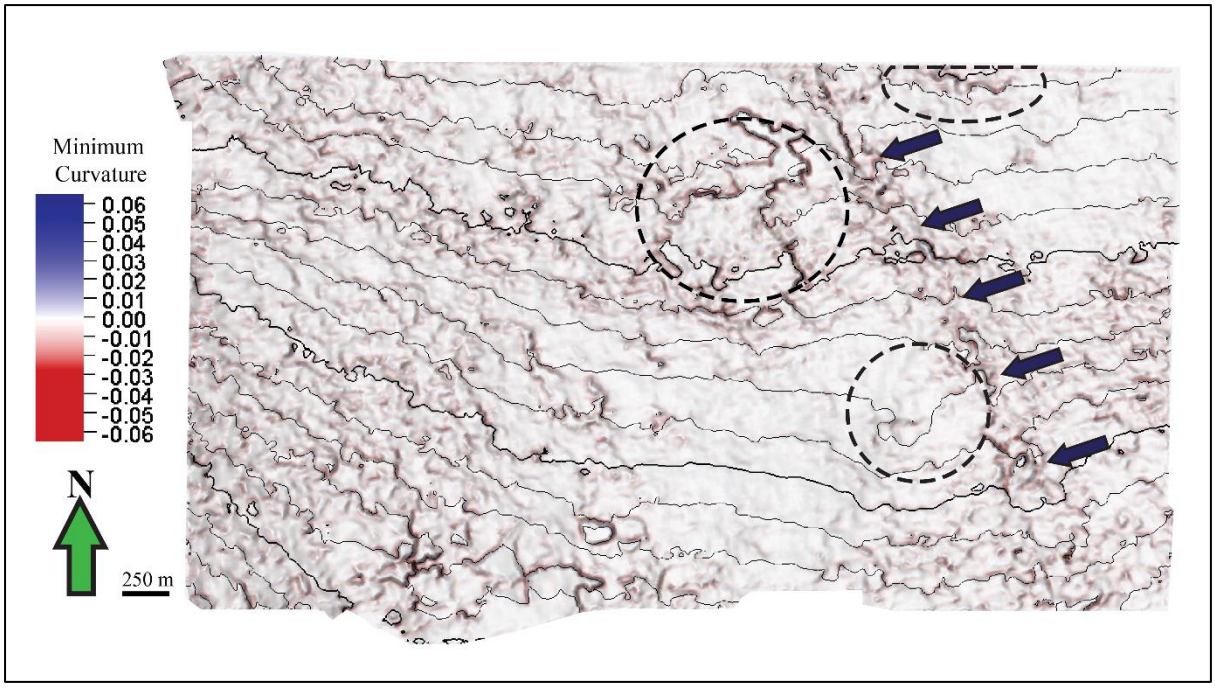

***Figure 5.26**. Merensky Reef after the application of the minimum curvature attribute highlighting a linear feature (arrows) and changes in contour lines and low curvature values(circles).*

5.6 FAULT ENHANCEMENT AND ITS ASSOCIATION WITH POTHOLES

Results (Chapter 5.5) from seismic attributes have shown the detection of one major fault that trends north-northwest, which is a dominant structure in the study area. This section focuses on this fault by examining its extent (in depth) through different volumetric attributes.

From the volumetric attributes, starting with the variance attribute, it is noticed that the variance attribute is able to better enhance the detection of the faulted region when compared to the original amplitude section (Figure 5.27a). In Figure 5.27b, the seismic section is dominated by values ranging from 0 – 0.50 except at the point where the fault is dominant. For example, the variance values rise from 0.50 to 0.90 at the faulted region. However, there is little to no major displacement caused by the fault at the horizons, indicating the fault is dominated by a small throw that cannot be observed on seismic sections. Furthermore, it is noticed that the fault is

not mapped as a continuous single fault, but it breaks up into subtle fault segments (Figure 5.27b).

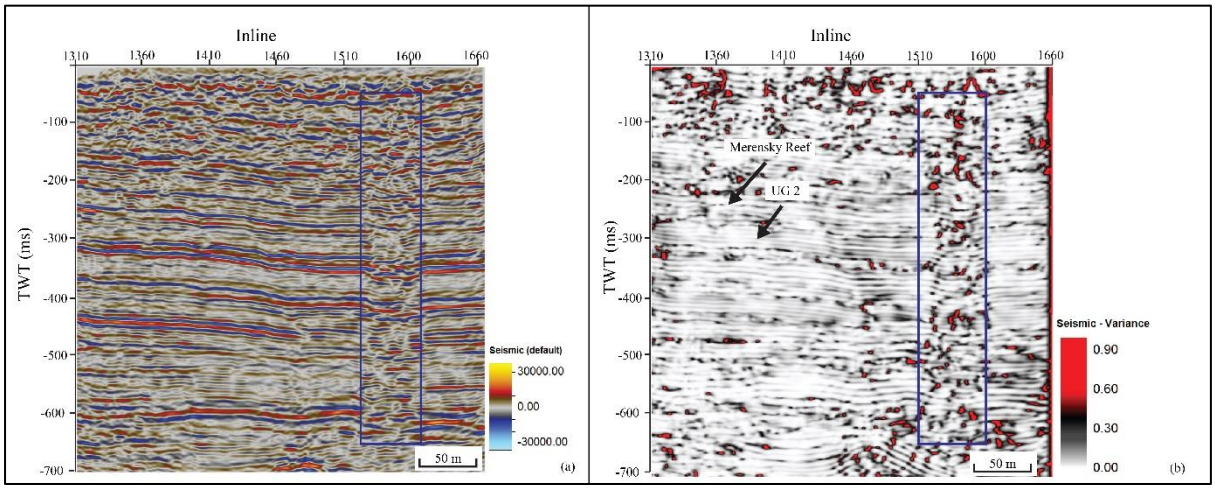

***Figure 5.27**. A comparison of (a) the seismic section prior to attributes and (b) the variance attribute to highlight the major fault. The blue box shows the region where the fault is. Crossline 5660 is shown here. The variance values rise from 0.50 to 0.90 at the faulted region. The faulted region exhibits little to no displacement and the fault is also broken up into smaller fault segments.*

In addition, chaos attribute (Figure 5.28) shows similar results to those obtained from the variance attribute whereby the low chaos values are interrupted by higher chaos values ranging from 0.50 – 0.80. As mentioned earlier, these values are representative of the faulted region within the seismic volume. The chaos attribute (Figure 5.28b) further identifies a second fault that is not observed or visible in the original amplitude display data (Figure 5.28a), which trends north-northwest as the major fault (marked in the green box in Figure 5.28). For example, the amplitude display seismic section is unable to map the continuity of the second fault whereas the chaos attribute shows increased chaos values along the fault plane, thus making it easier to trace its continuity.

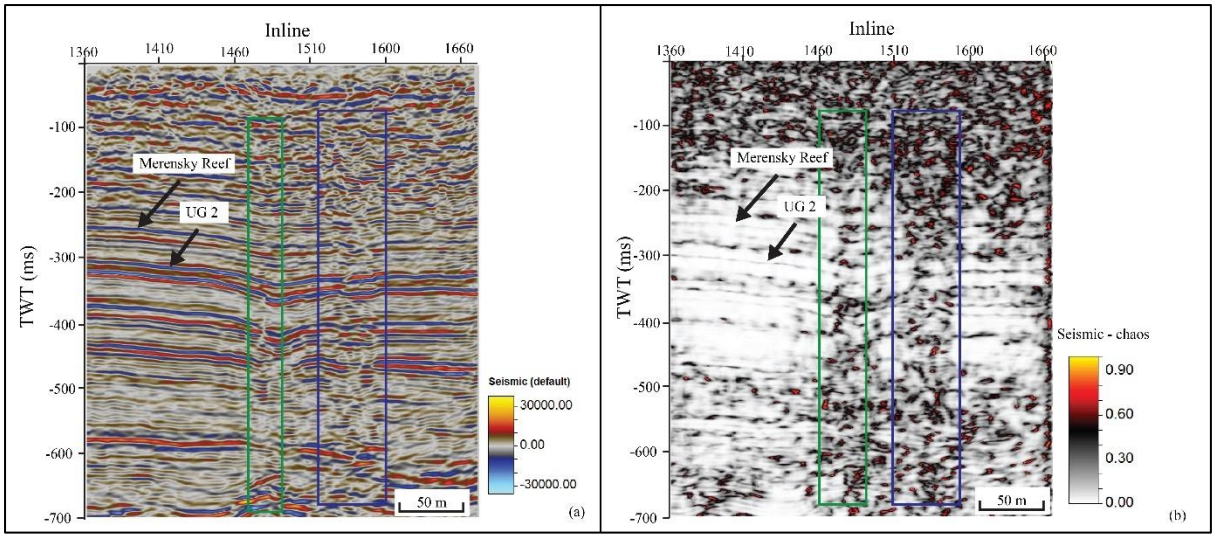

Figure 5.28. *A comparison of (a) the seismic section prior to attributes and (b) the chaos attribute to highlight the major fault. The blue box shows the region where the fault is, and the green box shows the new fault not previously seen using other attributes. Crossline 5690 is shown here. The chaos attribute shows two faults: the major fault (marked in blue box) and a secondary fault (marked in green box). The secondary fault is not observed or visible in the original amplitude display data. The fault trends in the north-northwest like the major fault.*

The application of the ant-tracking attribute to the seismic cube (Figure 5.29) shows that the fault, previously detected by 3D horizon-based seismic attributes, is not a single fault but a fault zone that is made up of multi-fault segments and fractures. Ant-tracking attribute (Figure 5.29b) shows a degree of faulting that is not clear on the horizon attributes and original seismic sections (Figure 5.29a). For example, at 450 – 600 ms (within the red box) in Figure 5.29b, the section is characterized by clear fractures that were not visible in the original seismic amplitude display (Figure 5.29a). Also, the seismic section extracted from ant-tracking volume shows that the fault zone is continuous and offset the strata below and above the UG-2 and Merensky Reef horizons.

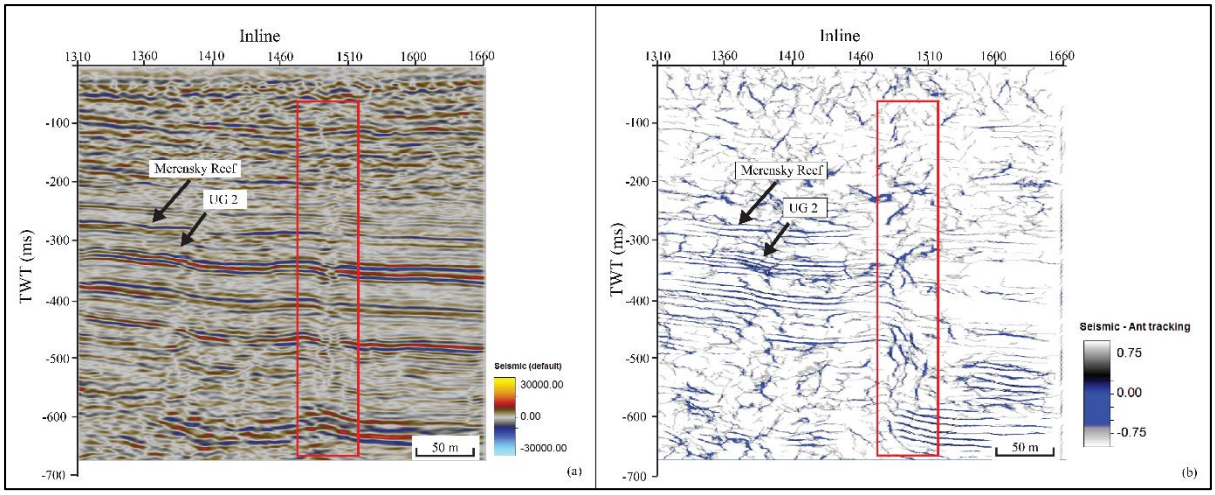

***Figure 5.29**. A comparison of (a) the seismic section prior to attributes and (b) the ant-tracking attribute to highlight the major fault. The red box shows the region where the fault is. Crossline 5780 is shown here. The ant-tracking attribute shows that major fault (within the red box) is not a single fault but a fault zone that is made up multi-fault segments and fractures. The fault zone is continuous and offsets the strata below and above the UG-2 and Merensky Reef horizons.*

The horizon-based attributes, such as dip, dip azimuth and edge detection, were computed for UG-2 horizon to better delineate the faults in the study area. In Figure 5.30 the dip attribute map exhibits a fault with a dip angle of about 8° - 9°. The map reveals that the fault is not a single continuous fault, but a fault zone made up of a series of discontinuous multi-fault segments (marked with arrows). This attribute also shows that there is another south-southeast trending fault (F3) that merges with the main fault zone (F1).

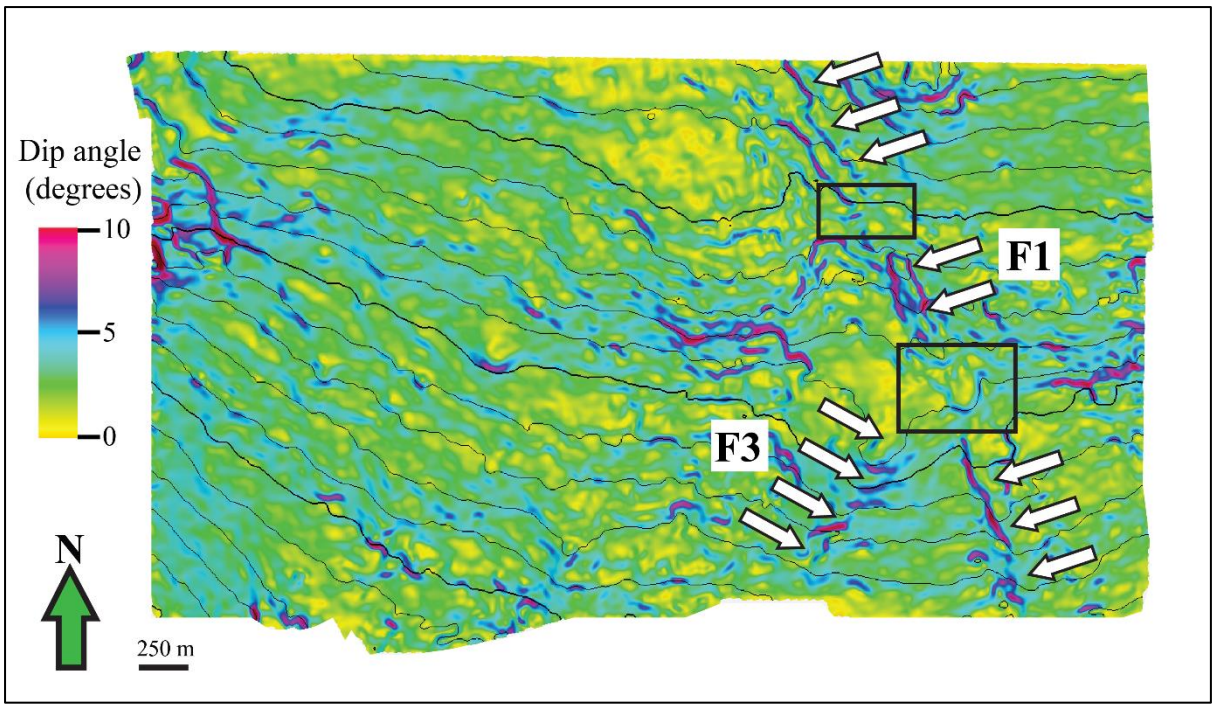

***Figure 5.30**. Dip angle attribute highlighting the major fault (F1). The fault has a dip angle of about 8° - 9°. The fault is seen as discontinuous (seen with the black boxes) also a secondary fault (F3) merges into the main fault.*

In addition, the dip azimuth attribute (Figure 5.31) enhances the connectivity and continuity of the north-northwest trending multi-fault segments of the main fault zone (F1), i.e., the fault is a single continuous fault that can be traced across the survey area. Furthermore, the south-southeast trending fault (F3), with a dip between 25° and 50°, is better delineated by the dip azimuth attribute.

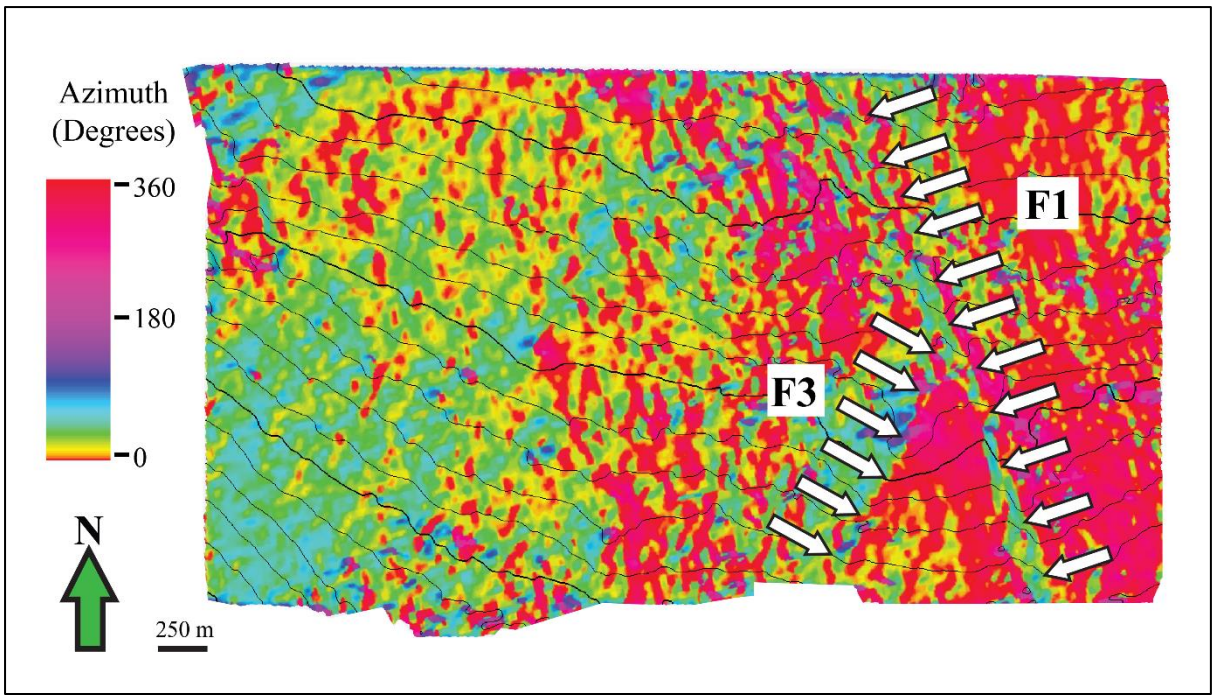

***Figure 5.31**. Dip azimuth attribute highlighting the extent of the major fault (F1) as well as a secondary fault (F3) that merges into the major fault. Both these faults have a dip azimuth range between 25° and 50°.*

The edge detection attribute map (Figure 5.32) shows an important degree of faulting, which is not observed in both dip and dip azimuth attributes. For example, the edge detection map shows that F1 starts as a single fault (shown as white arrows) in the north and splits into two fault segments forming another fault (F2) in the south. Furthermore, the edge detection attribute has enhanced the detection of the south-southeast trending fault (F3) that merges with the main fault near the southern part of the study area, which concurs with the results from dip and dip azimuth attributes.

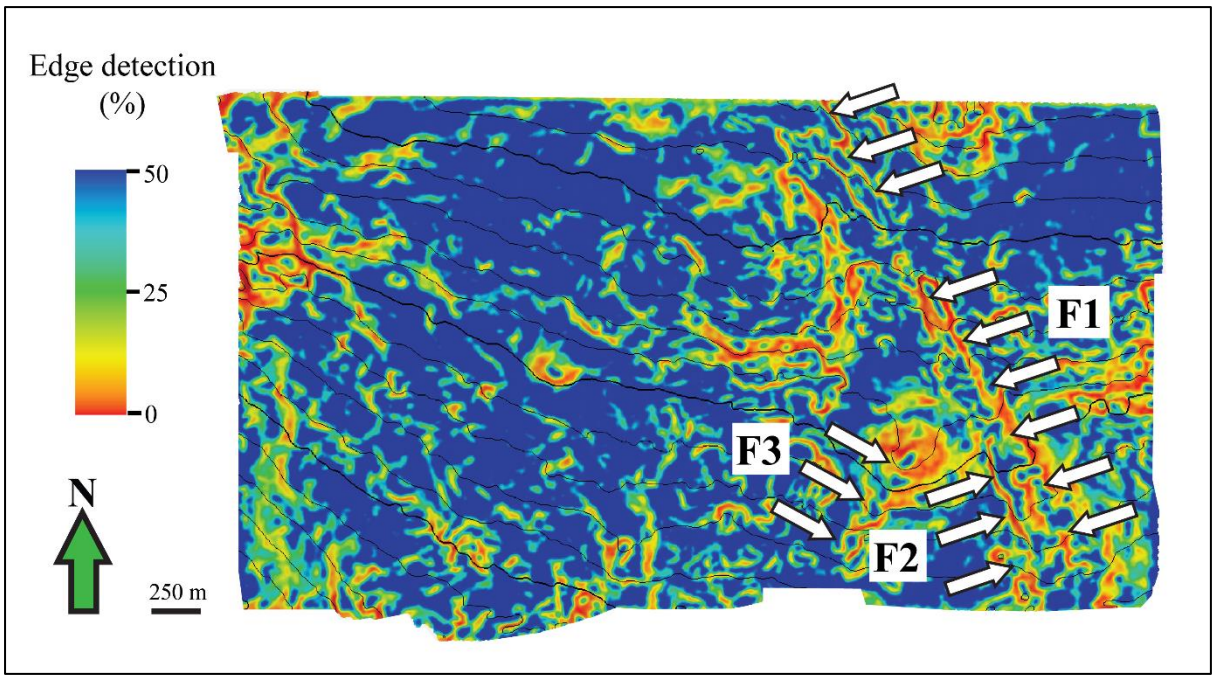

***Figure 5.32**. Edge detection attribute on the UG-2 highlighting the major fault (F1) splitting into two faults (F1 and F2) (extent is shown with the arrows). The edge detection attribute has enhanced the detection of the south-southeast trending fault (F3) that cuts through the pothole and merges with the main fault (F1) near the southern part of the study area.*

Inspection of the larger potholes on seismic sections shows that there are low amplitude reflections (indicative of faults or pegmetoids or both) that either crosscut the pothole or are visible beneath the pothole (green box in Figure 5.33). The low amplitude region is located at a TWT of -400 ms to -600 ms. The potholes with the lineament beneath do not occur only in the Merensky Reef and UG-2 but can be traced down to lower regions of the study area (shown with the dashed lines). Interestingly the smaller potholes firstly have no faults crosscutting them or beneath them and secondly, they are only visible on the Merensky Reef and the UG-2 and do continue deeper (Figure 5.34).

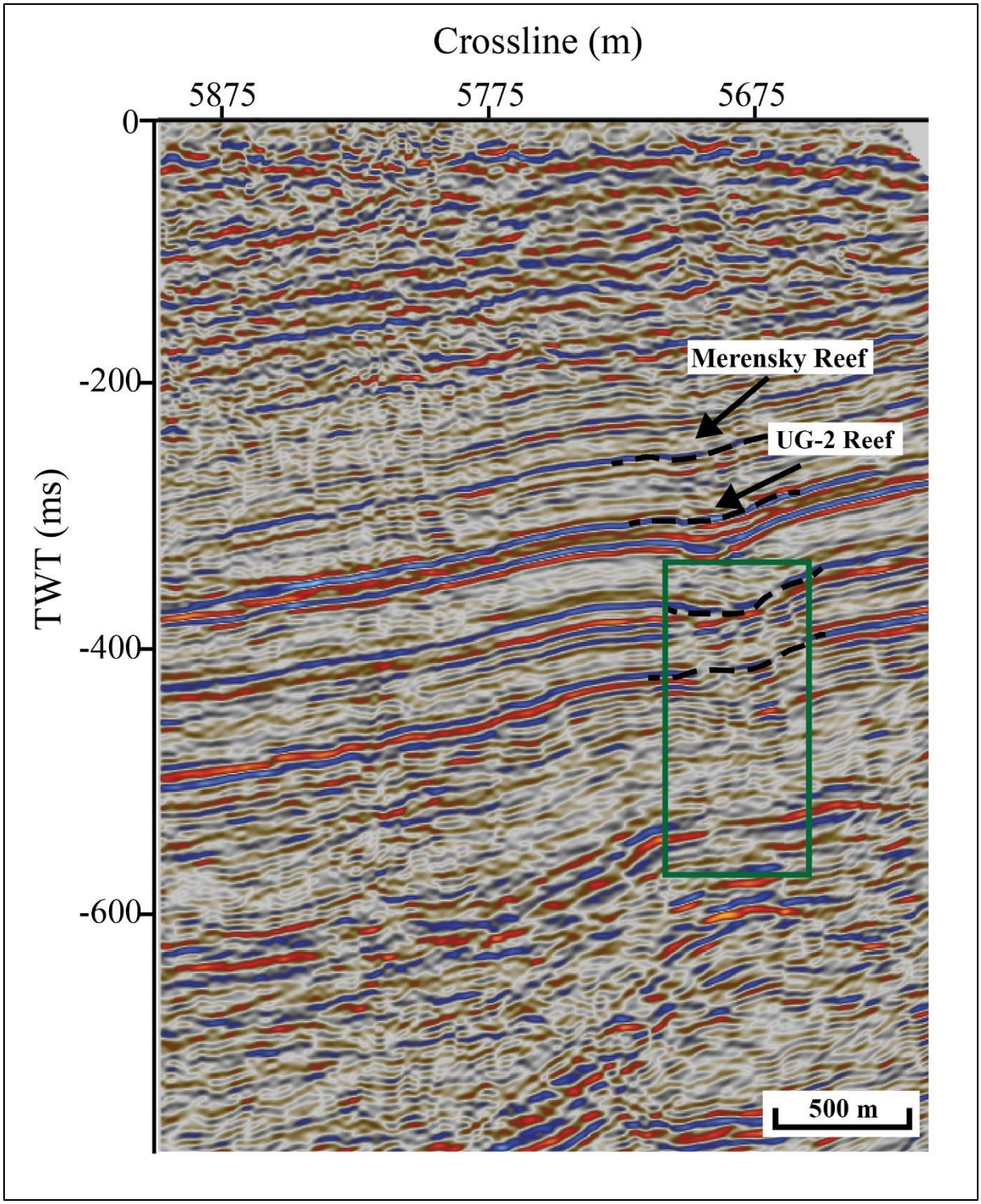

Figure 5.33. *Seismic section of the larger potholes that are seen at different depths (dashed lines) and the low amplitude reflections (fault) that crosscuts and extends beneath the pothole (Green square). Here the fault is identified in both the economic horizons (Merensky Reef and UG-2)*

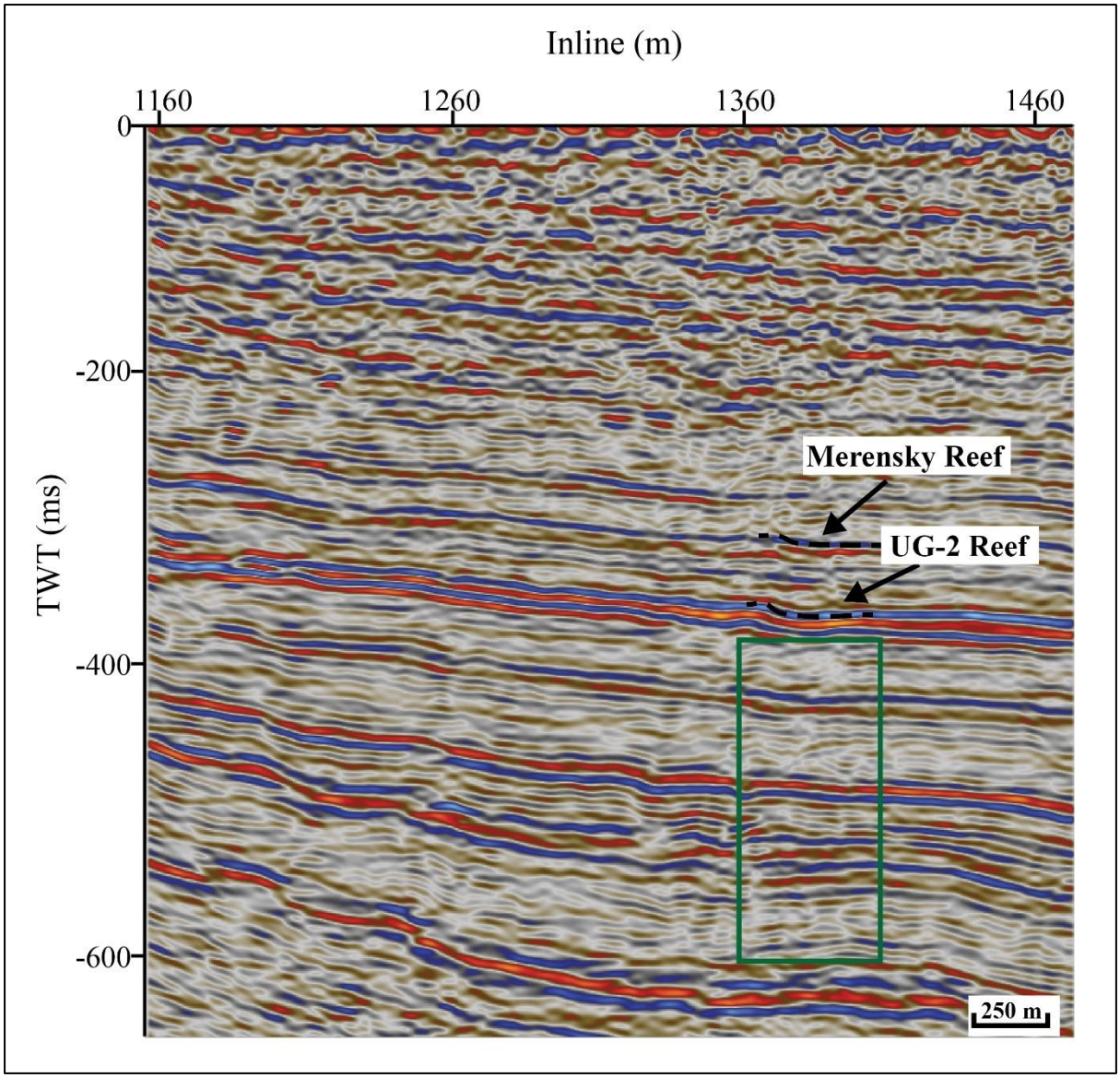

***Figure 5.34**. Seismic section of the small potholes only identified in the two reef horizons (Merensky Reef and UG-2) and the green box highlighting the absence of low amplitude reflections.*

5.7 POTHOLE CLASSIFICATION

The identified potholes are manifested as depressions within the seismic section (Figure 5.35a) and the section is characterized by pothole walls ranging from steep to gentle. The bottom of the pothole is defined as the region where the reflections weaken within the area. The edge of the pothole is identified as the perimeter where the pothole pinchs out and the horizon returns to the horizontal level. The distance between the two edges was measured as the diameter of the pothole. The depth was then calculated as the point orthogonal to the diameter line from

the bottom of the pothole (Figure 5.34b). Generally, the potholes can be asymmetrical on the cross-sections as the flanks are not on the same level on either side of the bottom.

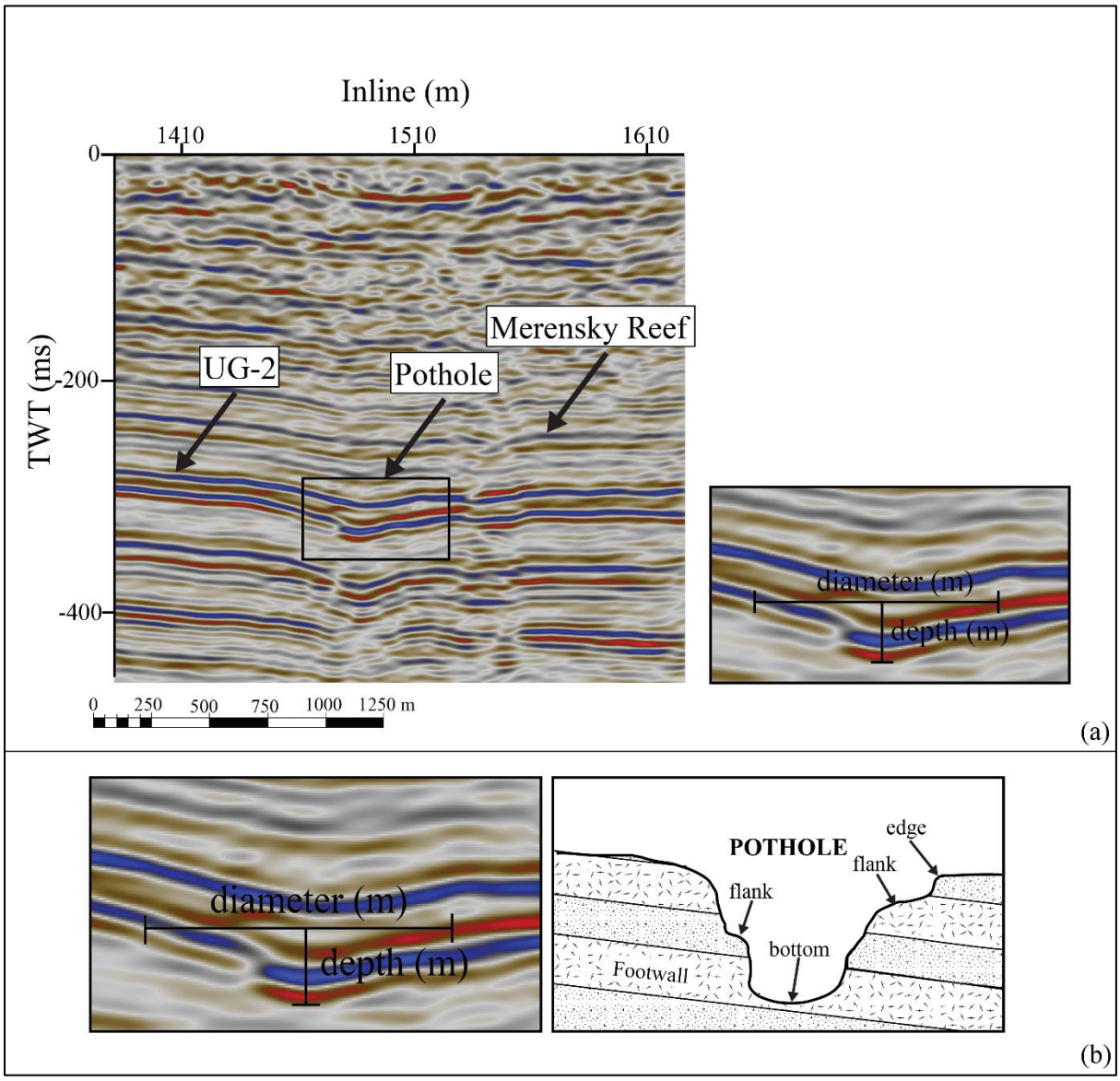

***Figure 5.35**. An image illustrating (a) a seismic section showing the main economic horizons, Merensky Reef and the UG-2. The section also highlights a pothole. (b) The diameter of the pothole was determined as the location where the reflector just straightened out and the depth as the deepest point where there is a slump. A schematic diagram of the determined pothole.*

5.8 SUMMARY

The layers of the Bushveld Complex and its associated horizons were imaged using different complex-trace attributes. The attributes clearly show four main horizons in the top 600 ms of the section. Horizons were determined as continuous horizontal regions with similar values that are distinct from the rest of the section.

The above-mentioned complex-trace attributes are able to identify the horizons because there is a significant acoustic impedance contrast between the alternating layers of orthopyroxenites and chromitites, giving rise to strong reflections. The instantaneous phase attribute also reveals the continuity of the reflectors as the attribute does not regard the waveform and computes the argument of the analytical signal per-sample (Schlumberger, 2015).

Most of the volumetric attributes (chaos and variance) do not only enhance definition of the seismic horizons in the data but also show better enhancement of discontinuities that are not well observed on the conventional seismic amplitude displays, while the structural smoothing attribute did not enhance any features. These discontinuities are interpreted as faults, since they displace the horizons. The chaotic region, in particular, suggests that most discontinuities in the data may represent intrusions such as dykes since they do not displace the horizons. This is further supported by observed weakening of the otherwise strong and continuous horizons in the vicinity of the chaotic region. The variance attribute was able to better enhance the faults when compare to the other attributes.

The results from the confidence map (see Figure 5.15) suggest that the eastern region of the study area exhibit more larger potholes (in size) than the western side which is less structurally complex with smaller potholes (in size). Furthermore, the results show that low confidence areas are mainly associated with potholed and faulted areas, which cause difficulties in picking seismic horizons using conventional methods.

The horizon-based attributes also highlighted slump structures which were interpreted as potholes. The potholes are seen as bright spots or circular areas with an attribute value differential with the surrounding areas. The horizon-based attributes could identify a fault that is truncated in the north-northwest to the south-southeast of the study area. This was true on both the Merensky and UG-2 reefs. Seismic attributes also identified similar potholes at both UG-2 and Merensky Reef levels. Potholes were not observed in the lower parts of the seismic section. They seem to be restricted to the upper 800 ms.

In general, potholes are asymmetrical in shape on the cross-sections and sometimes have association with faulting. Summarily, the volumetric attributes and the horizon-based attributes are able to enhance the continuity, crosscutting relationships and bifurcations of the fault networks, which is not possible with conventional interpretation on seismic sections.

6 STATISTICAL ANALYSIS AND SPATIAL ANALYSIS ON THE LOCATED POTHOLES

6.1 INTRODUCTION

The distribution of potholes has received little attention from the mining companies in the Bushveld Complex as predicting their occurrence is challenging and no genetic model is universally-accepted. This unfortunate lack of understanding may cause problems for deep mine planning. Previous studies suggested that potholes in the Bushveld Complex are randomly distributed with some clustering (Farquhar, 1986; Ballhaus, 1988; Carr et al., 1994; Chitiyo et al., 2008). Since potholes identified in the UG-2 were the same potholes identified in the Merensky Reef (see Chapter 5) and UG-2 is the most economically significant horizon of the two, subsequent analyses were only conducted on the UG-2 horizon. In this chapter, potholes are statistically analysed by considering their physical properties such as their locations, diameters and areas, and depths from the UG-2 horizon. A principal goal of these analyses is to categorise the potholes and identify their statistically-relevant characteristics.

6.2 INTEGRATED METHODS FOR POTHOLE CHARACTERISATION

Various measurements were made on the potholes that were identified on the UG-2 horizon: diameters, TWTs, depths from the UG-2, diameters and areas. Potholes that were identified through seismic attribute analysis are listed in Table 6.1 This method was able to identify 35 potholes present at both the Merensky Reef and the UG-2 horizons. Potholes that were identified with the difference-of-two-surfaces method are listed in Table 6.2. This method was able to identify 66 potholes. It is important to reiterate that all analyses were only performed on data from the UG-2 horizon. TWT was converted to depth using an average velocity of 6000

m/s (the average velocity at the UG-2 level). The depth in table 6.1 and 6.2 marks the depth position from the top to the bottom of the pothole.

Table 6.1. Measurements of identified potholes within the UG-2 using horizon-based attributes.

Pothole index	X (Easting)	Y (Northing)	Diameter (m)	TWT (ms)	Depth (m)	Area (m^2)
1	45966.38	-2840418.23	176.30	20.29	60.87	24411.50
2	45095.28	-2839894.40	107.20	15.67	47.01	9025.67
3	45422.88	-2840635.14	90.70	11.74	35.22	6461.07
4	45601.24	-2840500.03	98.40	13.16	39.48	7604.66
5	48065.75	-2840997.25	703.30	29.90	89.70	388482.19
6	48190.06	-2839100.23	711.80	16.31	48.93	397929.24
7	47071.30	-2839656.90	1027.50	35.25	105.75	829189.02
8	44417.62	-2839694.74	814.90	22.09	66.27	521553.08
9	45076.99	-2839597.45	164.60	14.61	43.83	21278.92
10	45293.17	-2840116.30	137.80	12.83	38.49	14913.80
11	45433.69	-2841483.67	92.30	7.48	22.44	6691.03
12	45358.03	-2841343.15	88.00	13.16	39.48	6082.12
13	45547.19	-2841435.03	140.70	10.68	32.04	15548.13
14	46006.58	-2841543.12	112.10	9.26	27.78	9869.64
15	46125.49	-2841570.15	51.30	7.83	23.49	2066.92
16	45947.13	-2840981.04	129.90	13.52	40.56	13252.82
17	46336.27	-2841364.77	117.80	20.31	60.93	10898.84
18	46195.75	-2840127.11	86.20	16.02	48.06	5835.85
19	46957.80	-2840975.64	60.50	3.72	11.16	2874.75

20	48952.11	-2841526.91	98.20	7.83	23.49	7573.78
21	49081.82	-2840154.13	520.90	12.09	36.27	213107.43
22	44812.16	-2840224.39	49.90	14.23	42.69	1955.65
23	44752.71	-2840527.05	69.60	11.74	35.22	3804.59
24	45817.42	-2839602.85	54.80	5.68	17.04	2358.58
25	49298.01	-2840121.70	68.90	9.97	29.91	3728.45
26	44968.89	-2841516.10	82.10	11.38	34.14	5293.91
27	49092.02	-2840172.81	56.60	7.83	23.49	2516.07
28	46406.53	-2841526.91	80.40	8.55	25.65	5076.94
29	44466.26	-2840500.03	64.50	7.10	21.30	3267.45
30	44125.77	-2838986.73	97.70	14.23	42.69	7496.85
31	44752.71	-2841672.83	59.20	8.19	24.57	2752.54
32	45903.90	-2841732.29	58.30	5.68	17.04	2669.48
33	46730.81	-2840046.04	68.70	4.97	14.91	3706.84
34	46806.47	-2839165.08	36.70	8.90	26.70	1057.84
35	49303.41	-2840656.76	92.20	10.68	32.04	6676.54

Table 6.2. Measurements of identified potholes within the UG 2 using the difference-of-two-surfaces method. The values highlighted in red are potholes whose depth is below the vertical resolution limit (11 m).

Pothole index	X (Easting)	Y (Northing)	Diameter (m)	TWT (ms)	Depth (m)	Area (m^2)
1	48978.38	-2840282	711.01	3.36	21.84	193032.00
2	44334.03	-2839441	456.48	5.74	37.31	98163.00
3	44143.97	-2838990	123.54	3.63	23.60	8576.29
4	45493.16	-2838927	77.53	1.09	7.09	3032.69

5	46971.30	-2839954	695.40	5.09	33.09	263828.00
6	48207.40	-2840039	626.99	4.46	28.99	180853.00
7	48207.40	-2839044	1069.61	8.02	52.13	219650.00
8	49000.13	-2838936	114.76	1.56	10.14	6187.70
9	49055.82	-2839063	84.68	1.34	8.71	4597.90
10	46424.29	-2839044	322.38	4.32	28.08	62308.80
11	46582.58	-2839471	317.05	3.19	20.74	69980.10
12	49149.12	-2839646	74.19	1.79	11.64	3554.41
13	46417.19	-2839861	465.44	3.61	23.47	90344.80
14	46779.49	-2840764	128.90	2.23	14.50	12318.10
15	47568.04	-2840671	176.93	2.09	13.59	25777.90
16	47887.72	-2840899	771.82	11.02	71.63	253637
17	48027.02	-2841418	64.57	0.92	5.98	3936.82
18	48251.61	-2841453	116.64	1.50	9.75	8845.34
19	45010.59	-2840153	226.22	2.16	14.04	29674.70
20	44659.43	-2840631	295.61	2.30	14.95	31795.70
21	45094.49	-2840466	150.02	2.32	15.08	13262.60
22	44981.00	-2840534	64.42	0.96	6.24	2114.77
23	44783.74	-2840412	64.78	0.98	6.37	2538.51
24	44718.88	-2840361	56.60	0.88	5.72	1711.92
25	44591.88	-2840482	129.26	1.51	9.82	7655.51
26	44454.07	-2840509	46.83	0.87	5.66	1520.08
27	44540.54	-2840774	55.33	1.00	6.50	2094.24
28	44578.37	-2841020	266.31	1.77	11.51	41723.50
29	44610.79	-2841452	195.26	1.30	8.45	13319.80

30	44467.58	-2841328	75.68	1.04	6.76	3241.45
31	45043.15	-2841693	126.44	1.89	12.29	10714.30
32	45456.59	-2841012	162.96	2.15	13.98	15106.60
33	45942.99	-2840990	143.13	2.56	16.64	11448.70
34	46107.82	-2840939	140.59	2.53	16.45	16994.70
35	45797.07	-2841498	164.50	2.7	17.55	19816.90
36	45534.95	-2841414	219.61	4.42	28.73	21435.30
37	45359.31	-2841309	68.56	1.02	6.63	3053.50
38	45118.81	-2840923	289.97	1.91	12.42	35563.30
39	45470.32	-2841728	26.57	0.93	6.05	415.47
40	45656.37	-2841862	255.79	3.19	20.74	22580.20
41	46116.61	-2841774	70.09	0.82	5.33	1785.02
42	45956.49	-2841712	98.77	1.45	9.43	3762.13
43	45779.06	-2841671	78.05	1	6.50	2519.40
44	47185.41	-2841396	103.90	1.44	9.36	4940.38
45	46994.61	-2841508	26.20	1.03	6.70	281.81
46	46911.86	-2841480	80.67	1.04	6.76	3070.05
47	47196.91	-2840784	241.71	3.18	20.67	31334.30
48	47061.28	-2840584	53.12	0.94	6.11	1192.73
49	46778.54	-2841478	170.16	2.32	15.08	15503.80
50	47116.45	-2841163	176.72	1.06	6.89	11572.70
51	46495.80	-2840816	331.07	3.04	19.76	71808.80
52	46394.65	-2841384	488.83	5.23	34.00	108422
53	45424.59	-2841471	50.86	1.38	8.97	1664.93
54	46263.63	-2841074	121.51	1.73	11.25	8636.65

55	45663.66	-2841634	83.66	1	6.50	3102.48
56	46003.87	-2841519	78.44	2.14	13.91	3673.13
57	44849.92	-2840814	137.88	1.61	10.47	9684.48
58	45282.07	-2840846	74.50	1	6.50	3870.44
59	45390.40	-2840106	52.72	0.75	4.88	1957.66
60	46139.50	-2840795	118.43	1.69	10.99	8475.50
61	45521.14	-2840740	84.38	1.5	9.75	3941.79
62	45445.28	-2840628	65.61	1.76	11.44	2669.85
63	46068.24	-2846660	55.59	1.25	8.13	2422.17
64	45624.58	-2840549	135.43	2.75	17.88	6292.62
65	45488.96	-2840439	43.16	1.22	7.93	780.796
66	45971.69	-2840372	236.74	4.95	32.18	38267.80

Figure 6.1 shows a map of the identified potholes within the UG-2 horizon using horizon-based attributes and the major fault that crosscuts the horizon. Two groups of potholes were identified: (i) the larger potholes with diameters ≥ 300 m and the smaller potholes with diameters ≤ 300 m. The larger potholes are found near the edge of the studied portion of the horizon and near the major fault, while the smaller potholes are located in the central region of the studied portion of the horizon. The smaller potholes appear to be clustered and randomly distributed with a greater frequency of occurrence within the horizon. The larger potholes are not visually clustered and occur less frequently within the horizon. The larger potholes are more circular in shape while the smaller potholes are elliptical.

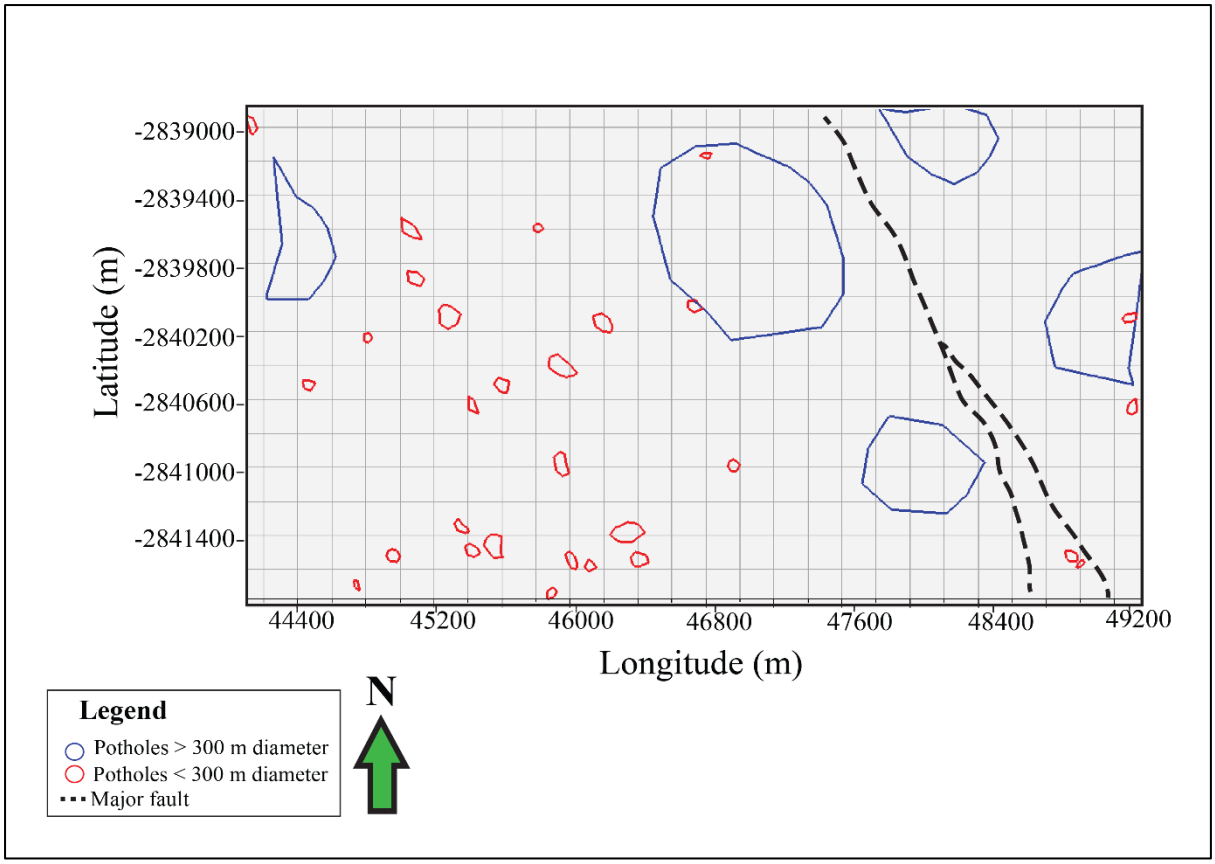

***Figure 6.1**. A map illustrating the identified potholes within the picked horizon using horizon-based attributes. The blue potholes have diameters greater than 300 m and the red potholes have diameters less than 300 m. The larger potholes (blue) are found mostly near the edge of the study area as well as around the major fault (dashed line) while the red potholes are found in the central region of the study area.*

Figure 6.2 shows a map of the identified potholes within the UG-2 using the difference-of-two-surfaces method, and the major fault that crosscuts and offsets the UG-2 horizon. In addition to the observations made on the potholes identified by the seismic attributes, larger potholes identified using this method are mostly irregular and tend to be more oval in shape, with the elongation axis roughly in the direction of the major fault, and the smaller potholes are more circular.

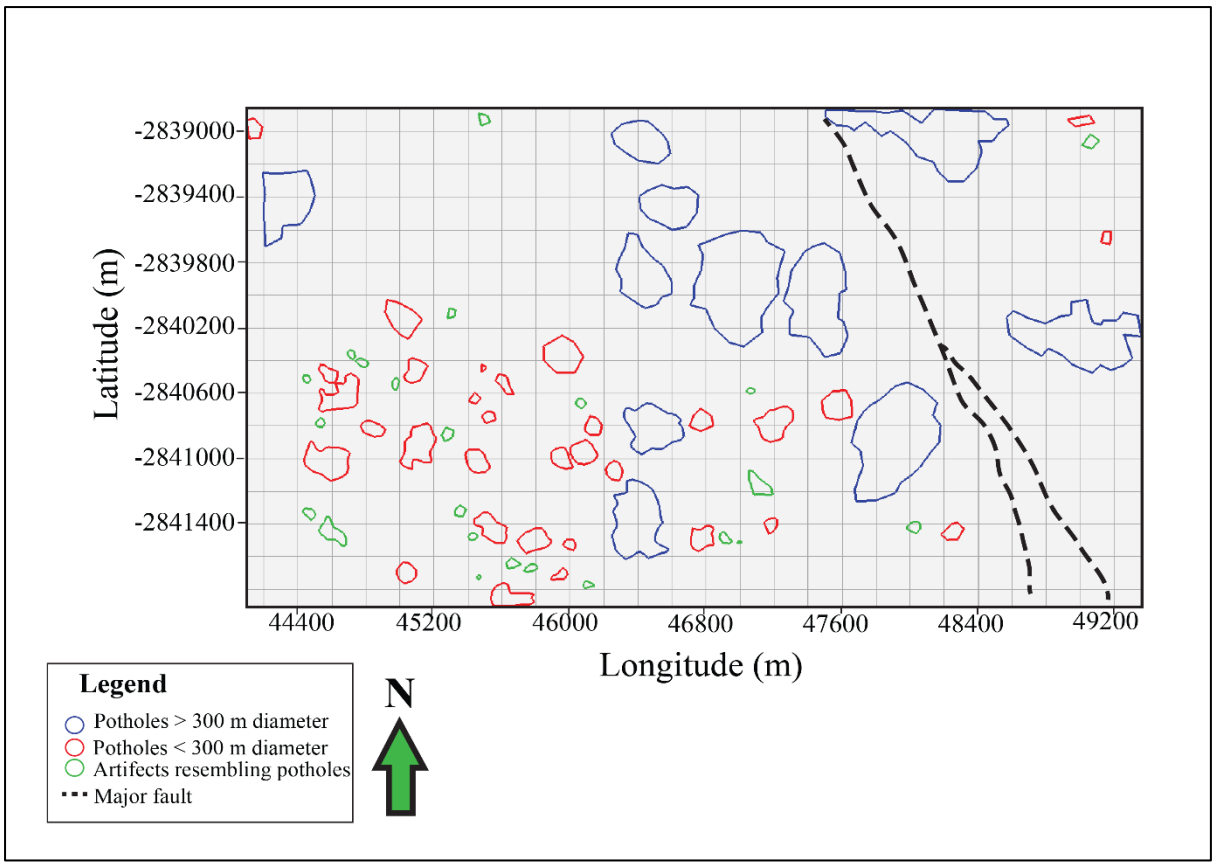

***Figure 6.2**. A map illustrating the identified potholes within the picked horizon using the difference-of-two-surfaces method. The blue potholes have diameters greater than 300 m, the red potholes have diameters less than 300 m and the green "potholes" below the seismic resolution limit. The larger potholes (blue) are found mostly near the edge of the study area as well as around the major fault (dashed line) while the red potholes are found in the central region of the study area. The blue potholes are more irregular in shape while the red potholes are more circular.*

Both the horizon-based attributes and the difference-of-two-surfaces method were able to identify potholes. However, the identified quantities are different. As shown in Table 6.2 31 of the identified potholes are below the resolution limit of the seismic volume (vertical resolution of ~11 m) and thus cannot be confidently classified as potholes. Furthermore, when comparing Figures 6.1 and 6.2, it is possible that the larger potholes seen in Figure 6.1 may actually be a combination of smaller potholes. The purpose of the study was no means to resolve the discrepancy between the two identification methods, but to increase the confidence of pothole

identification. Therefore, only potholes that were identified by both methods were used for further analyses. A total of 43 potholes were co-identified by both methods (see Figure 6.3).

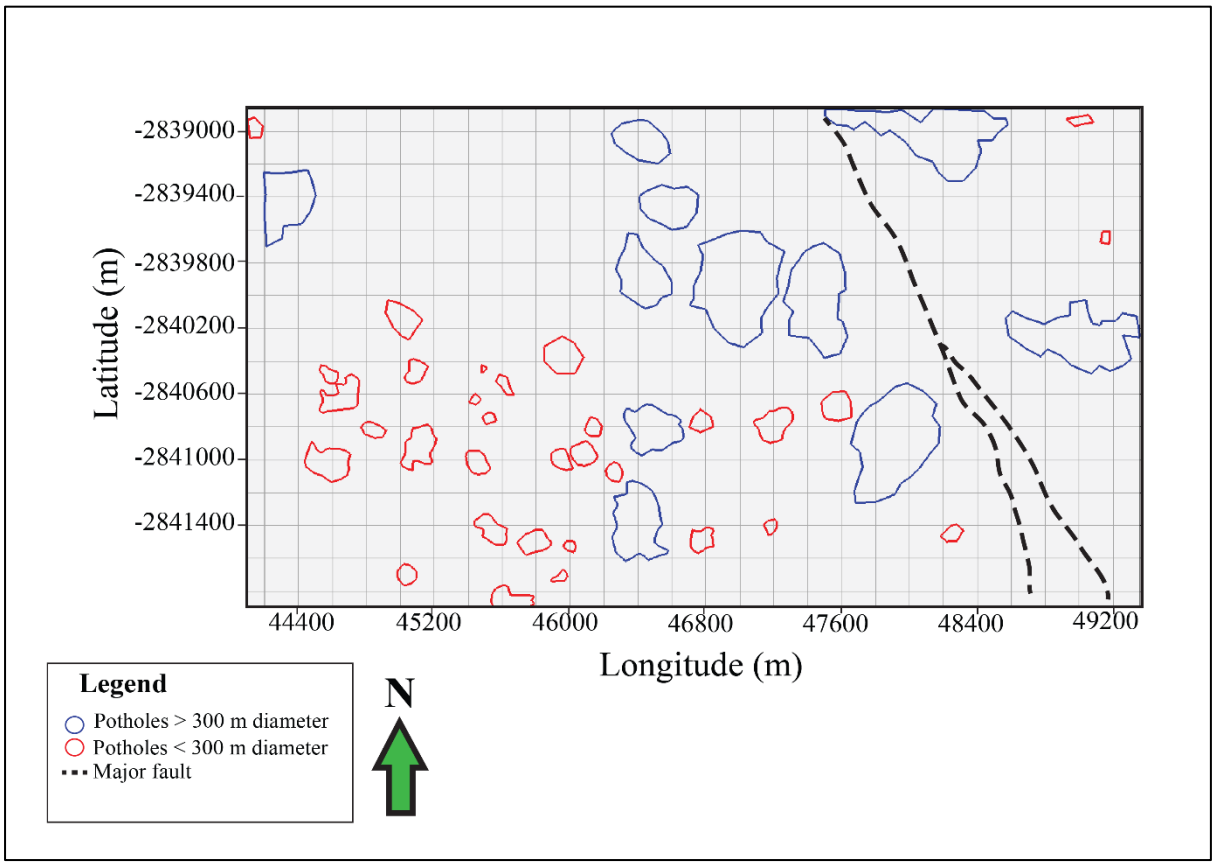

***Figure 6.3**. Potholes co-identified by both attributes-based and surface-difference-based methods, using shapes and coordinates identified by the surface-difference-based method. The blue potholes are those with diameters greater than 300 m and the red potholes are those with diameters less than 300 m.*

6.3 STATISTICAL ANALYSIS

There appears to be a positive and possibly linear relationship between the depths and the diameters of the potholes (Figure 6.4). However, the majority of potholes have diameters that range from greater than 50 m to less than 300 m and only a few are greater than 300 m. About 97% of the potholes exhibit depths less than 40 m and only two potholes were deeper than 40 m.

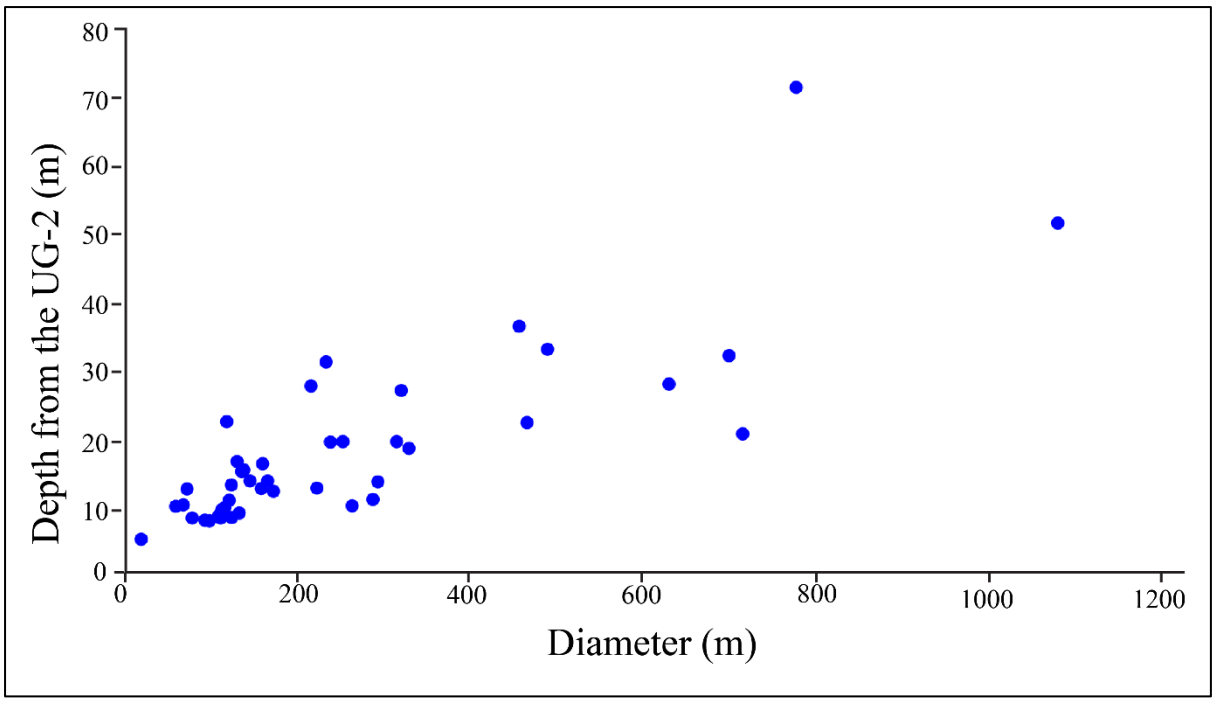

Figure 6.4. *A graph showing the depth from the UG-2 versus the diameter of the potholes. The graph shows a linear relationship between the depths and the diameters of the potholes. 97% of potholes have depths of 40 m or less and only two potholes have diameters greater than 40 m. Most of the potholes have diameters less than 300 m while only a few have potholes greater than 300 m.*

The data suggest that there are two classes of areal sizes of potholes in the vicinity (Figure 6.5), separated by ~1.5 x 10^5 m^2 in area. Figure 6.5 indicates that potholes with larger areas (> 1.5 × 10^5 m^2) (and thus diameters) are deeper than those with small areas (< 1.5 × 10^5 m^2). However, there are few potholes with larger areas which exhibit shallower depths than those with small areas. In general, potholes have varying aspect ratios and flatten with increasing size. Summarily, the study area is a characterized by a greater abundance of small to medium potholes compared to the larger potholes.

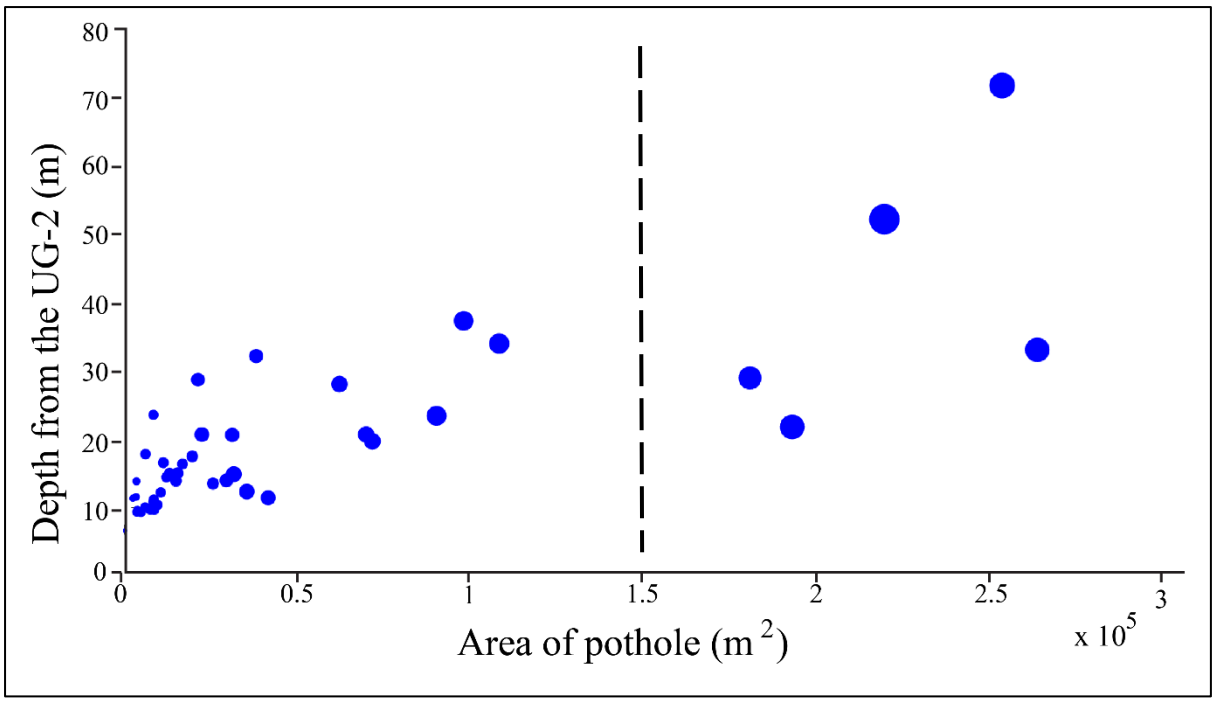

***Figure 6.5**. A bubble plot of the potholes where the x-axis is the area of the pothole, the y-axis the depth from the UG-2 and the bubble size the diameter of the pothole. The bubble plot shows two main classes of pothole (separated by the dashed line).*

Figure 6.6 shows a scatterplot of the potholes' locations and highlights their diameters. Near the fault, the potholes grow in volume. Furthermore, the histogram of the volume of potholes in Figure 6.7 suggests that their volumetric distribution is positively skewed. A log-transform of the data, shown in Figure 6.8, indicates a possibly normal volumetric distribution. To quantify the normality of this distribution, a quantile-quantile plot (Q-Q plot in Figure 6.9) and a Shapiro-Wilk normality test were performed. The Q-Q plot indicates that the distribution of the logarithm of the volumes of the potholes is only insignificantly deviated from normality, while the Shapiro-Wilk test provides a test statistic of 0.9856 with a p-value of 0.8597. Since this p-value is much greater than 0.05 and much closer to unity, the data can be said to have been significantly drawn from a normal distribution (Silverman, 1986). Therefore, both normality tests suggest that the logarithm of the volumes is significantly normal. Hence the volume of the potholes is most probably log-normally distributed.

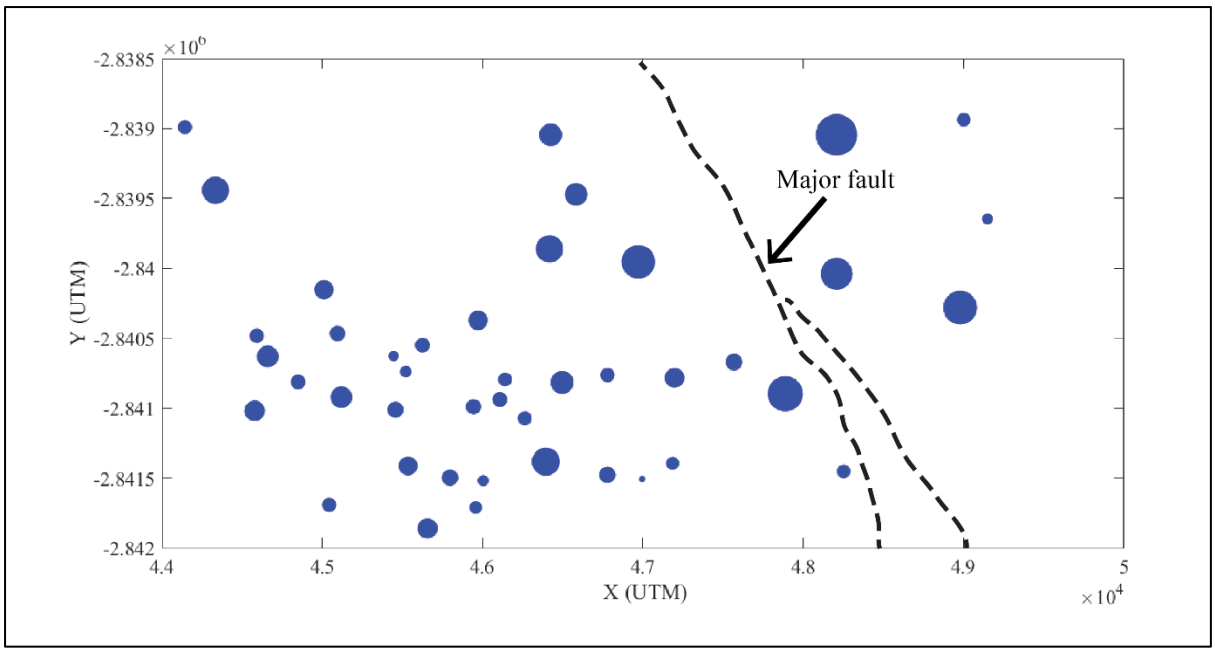

***Figure 6.6**. Spatial distribution of the potholes. The size of the circle represents the area of the potholes. The potholes located near the fault grow in volume as compared to those located a distance away from the pothole.*

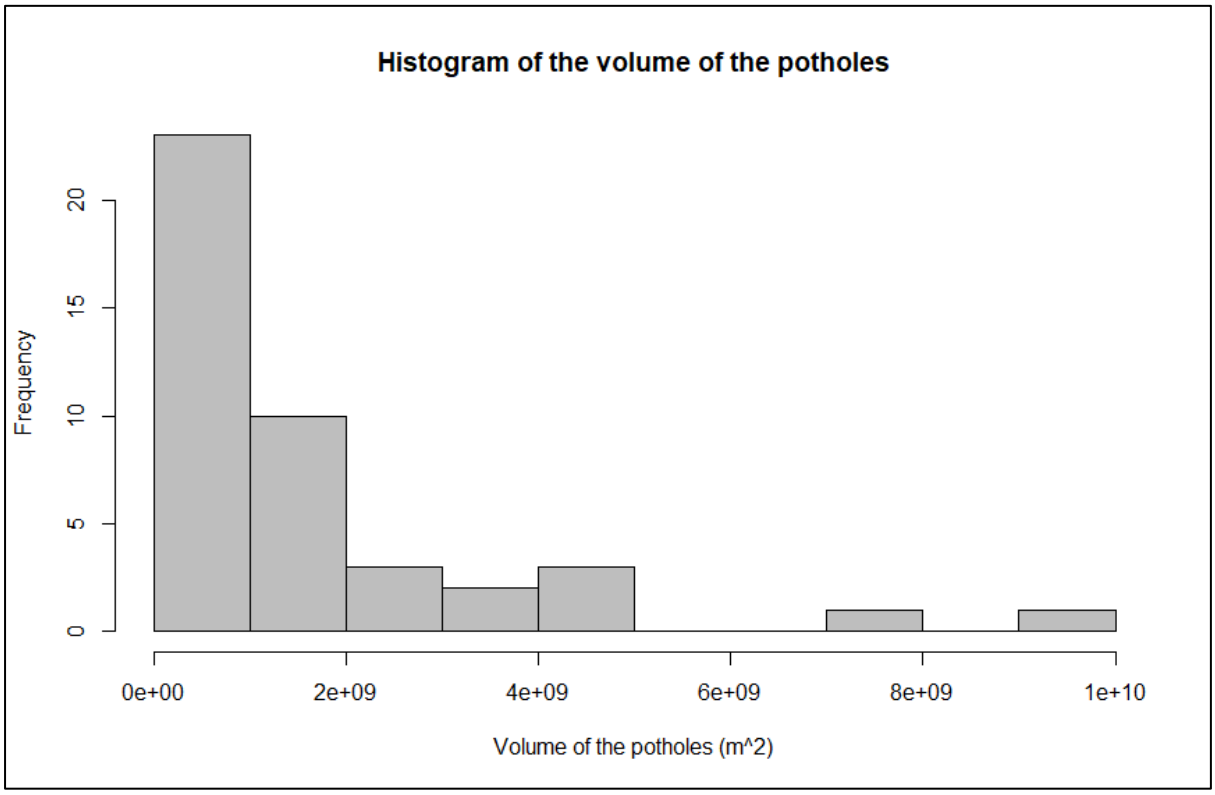

***Figure 6.7**. A histogram showing the frequency distribution of the volume of the potholes. The volumetric distribution of the potholes is positively skewed.*

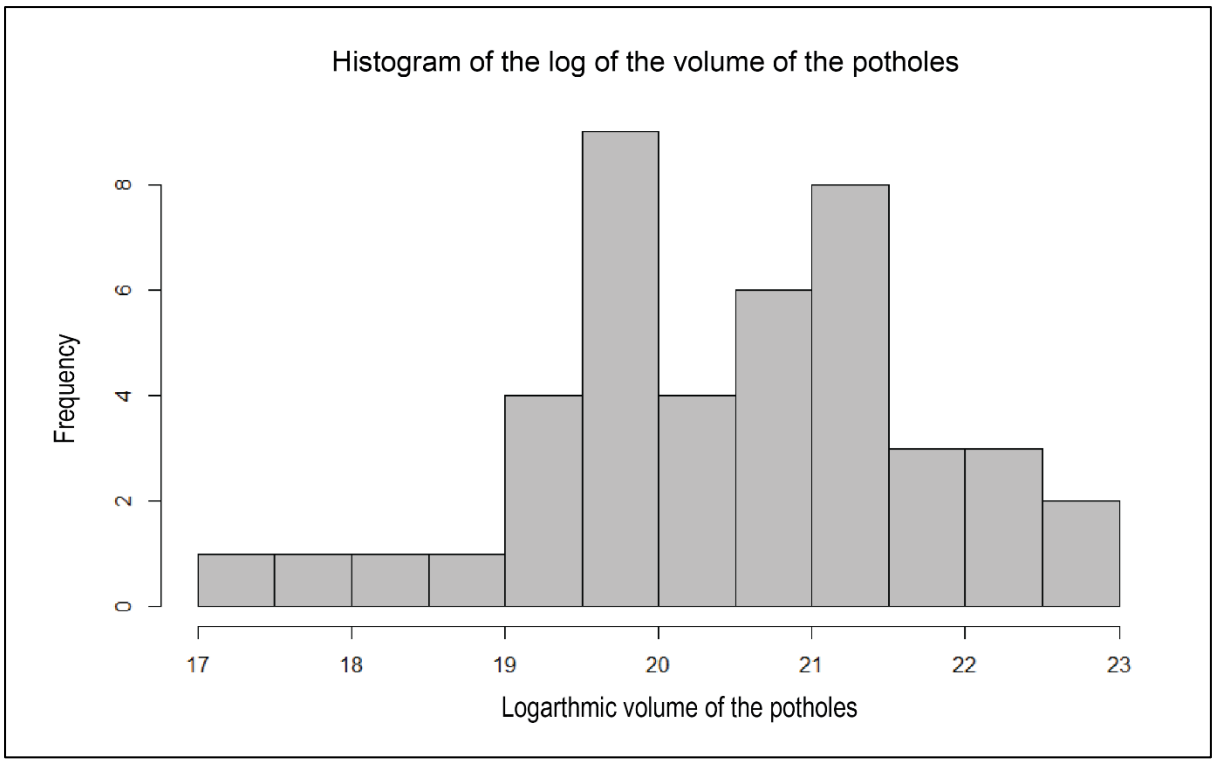

***Figure 6.8**. A histogram of the potholes' volumes after log-transformation. A normal distribution is identified in the data after transforming it.*

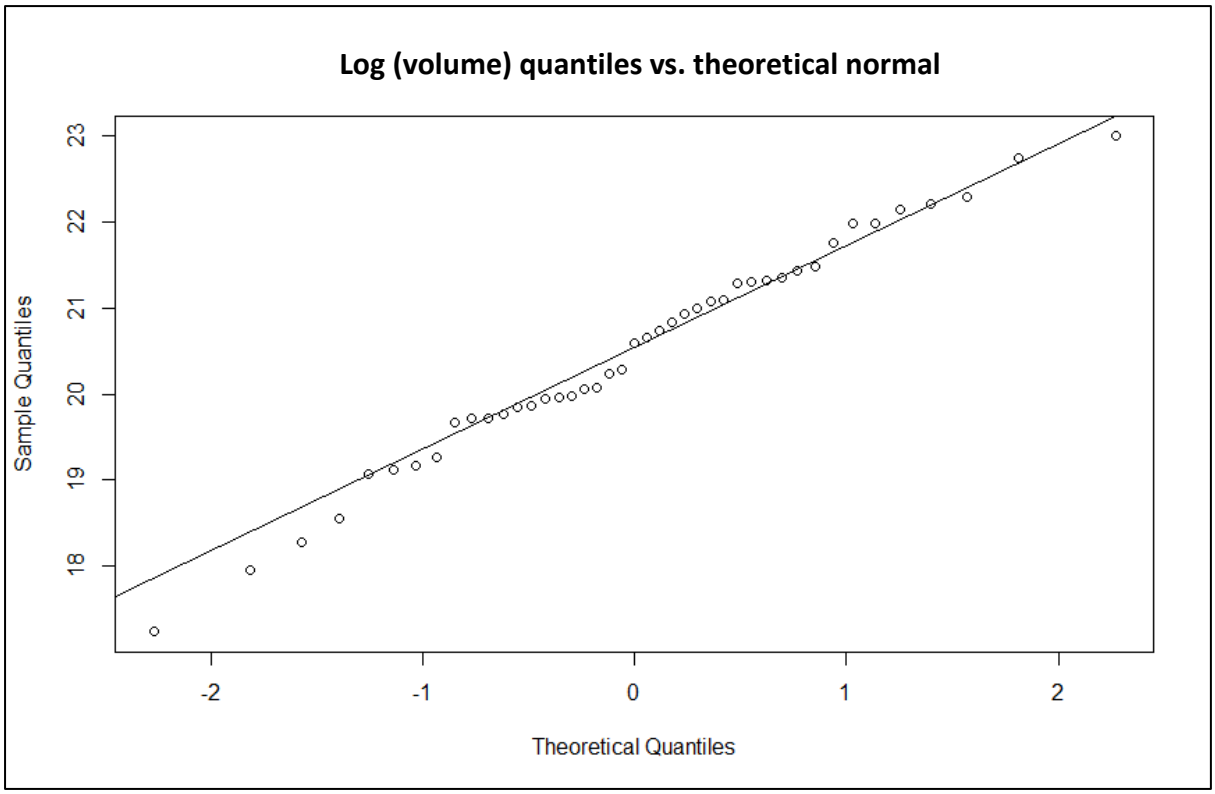

***Figure 6.9**. Q-Q plot of the logarithmic of the volume of potholes. The solid line represents ideal normality and the circles are the data points. The data points lie closely onto the normality line suggesting the data are normal.*

6.4 SPATIAL ANALYSIS

In order to understand the distribution of the potholes, a histogram (Figure 6.10) and a box-plot (Figure 6.11) are constructed from the inter-pothole pairwise-distances calculated from x- and y-coordinates of the potholes. Both the histogram and the box-plot indicate that the data are positively skewed to the right and the mean (1863.5 m) is larger than the median (1676.3 m). The skewness and kurtosis are 0.6974 and 2.8515, respectively. The skewness suggests that the distribution is asymmetric while the kurtosis constrains the flatness or "peakness" of the distribution. Therefore, the distribution is platykurtic since the computed kurtosis value is less than 3. The box-plot further shows that the maximum and minimum distances are 5048.0 m and 135.8 m, respectively.

A Shapiro-Wilk normality test conducted on the pairwise-distances between the different potholes from their central positions yielded a test statistic of 0.9525 and a p-value of less than 2.2×10^{-16}, which suggests that the inter-pothole distances are not normally-distributed. This is confirmed by a Q-Q plot (Figure 6.12), which shows that an appreciable amount of data departs significantly from normality and further demonstrates that the data are skewed and exhibit tails (shown in Figure 6.12).

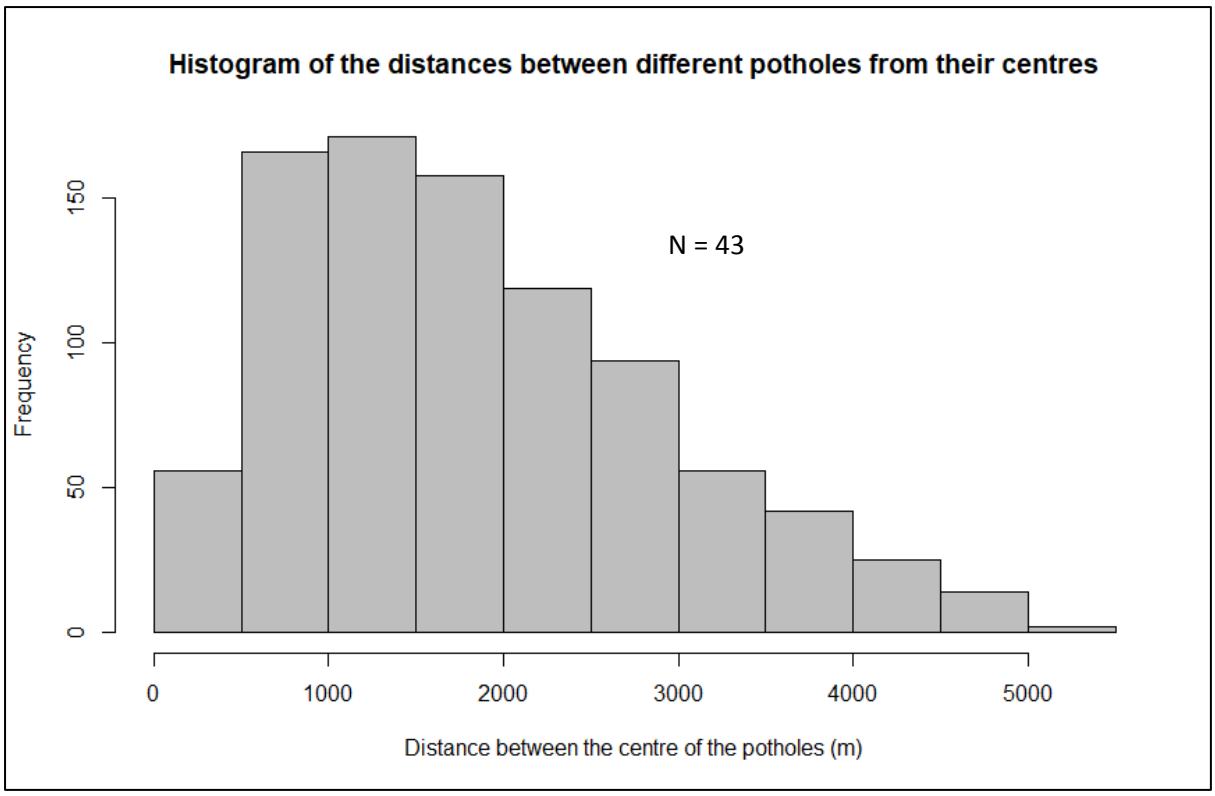

Figure 6.10. *A histogram showing the frequency distribution of the inter-pothole distances of the 43 identified potholes. The data are positively skewed to the right.*

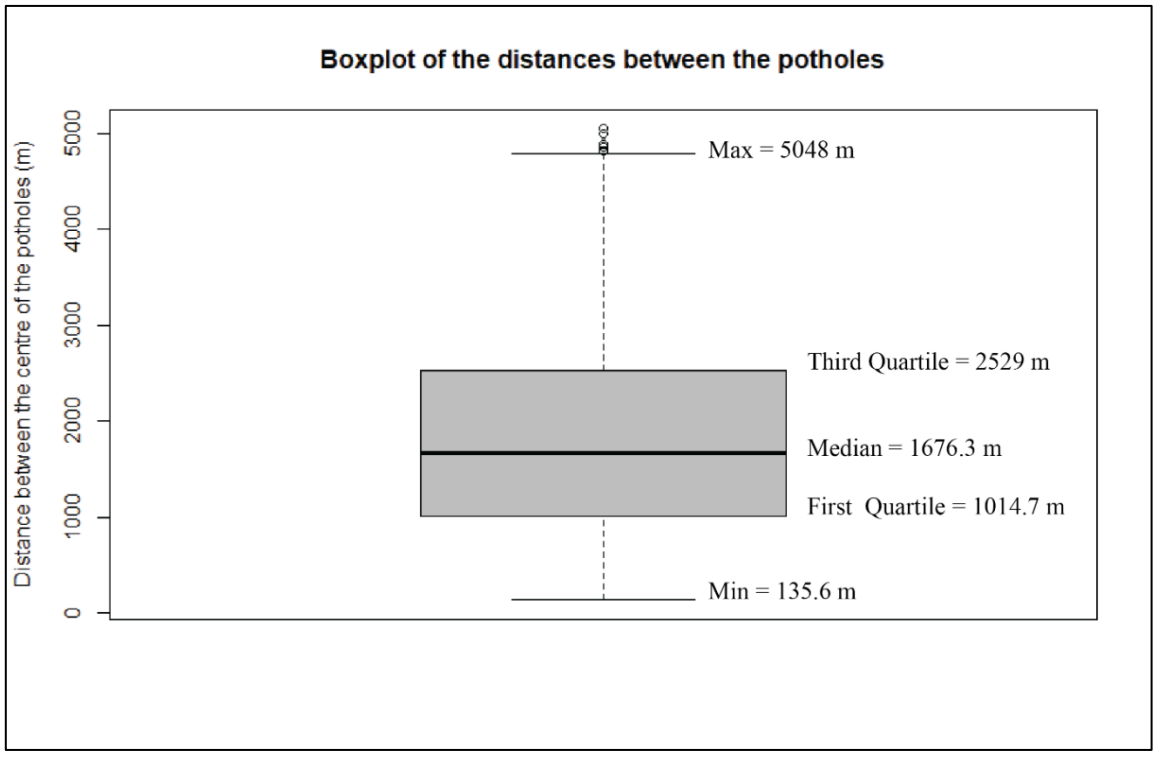

Figure 6.11. *A box plot of the distances between the identified potholes. The box plot revealed the minimum distance (135.6 m), first quartile (1014.7 m), median (1676.3 m), third quartile (2529 m) and maximum distance (5048 m).*

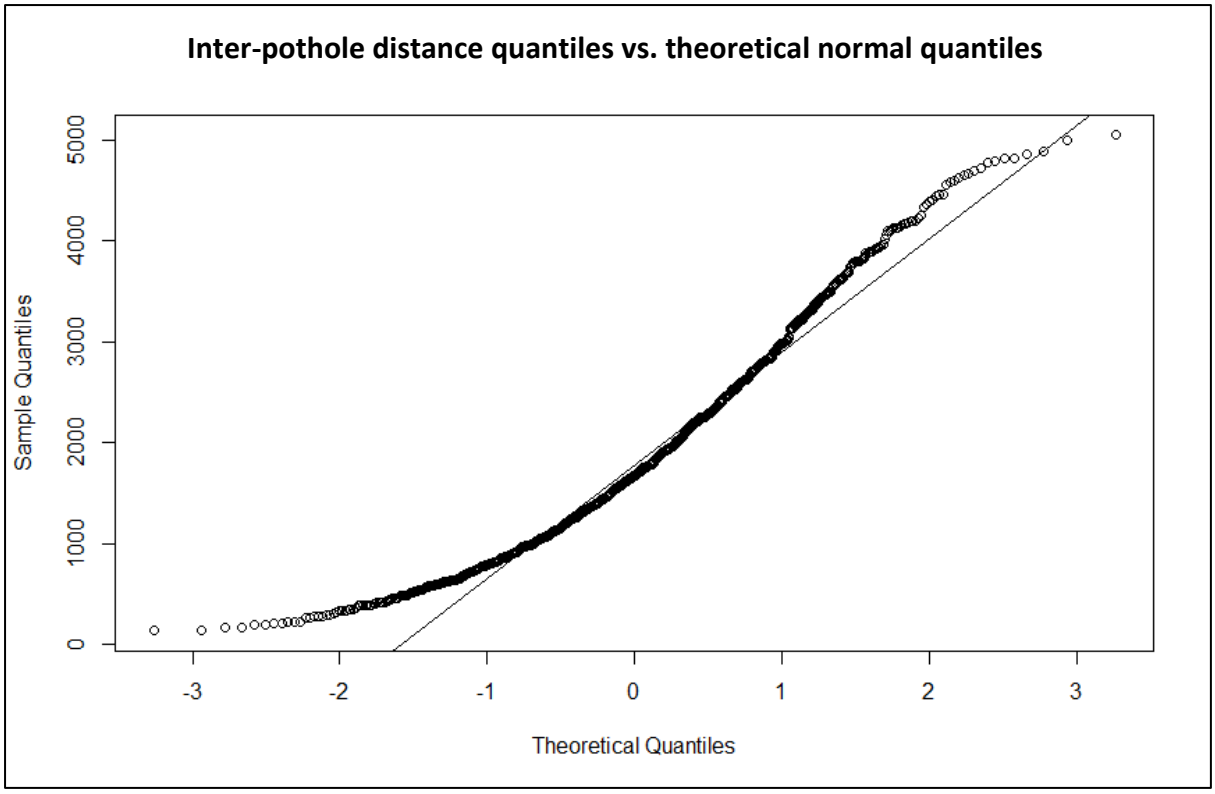

***Figure 6.12**. Q-Q plot of the distances between the potholes. The solid line represents the quantiles of a normal distribution; the data curve away from the straight line at the two ends suggesting indicating clear tails in the data.*

6.4.1 Quadrant analysis

To study the distribution pattern of potholes in study area, a quadrant analysis for a Poisson distribution model was performed (Davis, 2003). Table 6.3 shows the calculation of the expected number of quadrants containing a certain number of potholes when a Poisson distribution is assumed (which will be used in the χ^2 test). When the parameters are known or estimated, the expected frequency in each quadrant of the observed frequency distribution can be calculated (Stoodley, 1974). A χ^2 test is performed to see how closely related the observed potholes (per quadrant) are with the calculated potholes according to the Poisson model.

Table 6.3. Calculation of expected numbers of quadrants containing r potholes, assuming a Poisson distribution.

Number of potholes per quadrant (r)	Poisson model prediction	P(r) of potholes	Number of quadrants	
			Expected	Observed
0	$P(0) = e^{(-0.72)} \frac{(0.72)^0}{0!}$	0.4866	29.2	33
1	$P(0) = e^{(-0.72)} \frac{(0.72)^1}{1!}$	0.3505	21.0	16
2	$P(0) = e^{(-0.72)} \frac{(0.72)^2}{2!}$	0.1262	7.6	8
3	$P(0) = e^{(-0.72)} \frac{(0.72)^3}{3!}$	0.0303	1.8	3
TOTAL		**0.9936**	**59.6**	**60**

$$\chi^2 = \sum \frac{(Observed - Expected)^2}{Expected} \quad (27)$$

$$= \frac{(33-29.2)^2}{29.2} + \frac{(16-21.0)^2}{21.0} + \frac{(8-7.6)^2}{7.6} + \frac{(3-1.8)^2}{1.8}$$

$$= 2.5060$$

The χ^2 test statistic has v = c - 2 degrees of freedom, where c is the number of groups (one degree of freedom is lost because the expected frequencies are restricted to a sum of 60 and a second degree of freedom is required for estimation of the density of the potholes). The critical value of χ^2 test for v = 2 (v is the degree of freedom) and mean distance (α) = 0.05 is 5.991 (taken from the chi-squared distribution table found in Stoodley, 1974) as there are 4 groups (e.g. c = 4).

Since the test statistic is less than the critical value, the hypothesis of equality between the observed and expected distributions can be rejected. Thus, it can be concluded that the Poisson

model is appropriate. This suggests that the potholes could be randomly distributed within the study area in two-dimensions. The variance in number of potholes per quadrant is given by:

$$s^2 = \frac{\sum_{i=1}^{Q}(r_i - \frac{m}{T})^2}{T-1} \quad (28)$$

$$= 33\left(\frac{(0-0.72)^2}{59}\right) + 16\left(\frac{(1-0.72)^2}{59}\right) + 8\left(\frac{(2-0.72)^2}{59}\right) + 3(\frac{(3-0.72)^2}{59})$$

$$= 0.7977$$

where r_i is the number of potholes in the i^{th} quadrant, Q is the number of quadrants, m is the total number of potholes. Since the variance is greater than the mean, it must be concluded that potholes are more clustered than random (Davis, 2003).

6.4.2 Cluster analysis

The possibility of spatial clustering of the potholes was examined by k-means cluster analysis. By visual inspection, it is possible that larger potholes and smaller potholes are individually clustered. Following the visual intuition, K-means cluster analysis was able to identify two cluster centres that are indeed roughly classifiable by the size of potholes (see Figures 6.13 and 6.14). Clustering results of more than 2 initialized seeds featured no distinct or consistent trends with regards to the physical attributes of the potholes. Furthermore, from Figure 6.13, it can be seen that cluster 2's members are smaller than cluster 1's members, which are predominately large potholes. The distribution of the pothole clusters is such that cluster 1's members are located around the major faults (Figure 6.3) as the cluster centre is located approximately where the faults are. For cluster 2, there is no clear associated feature that is identified in this study.

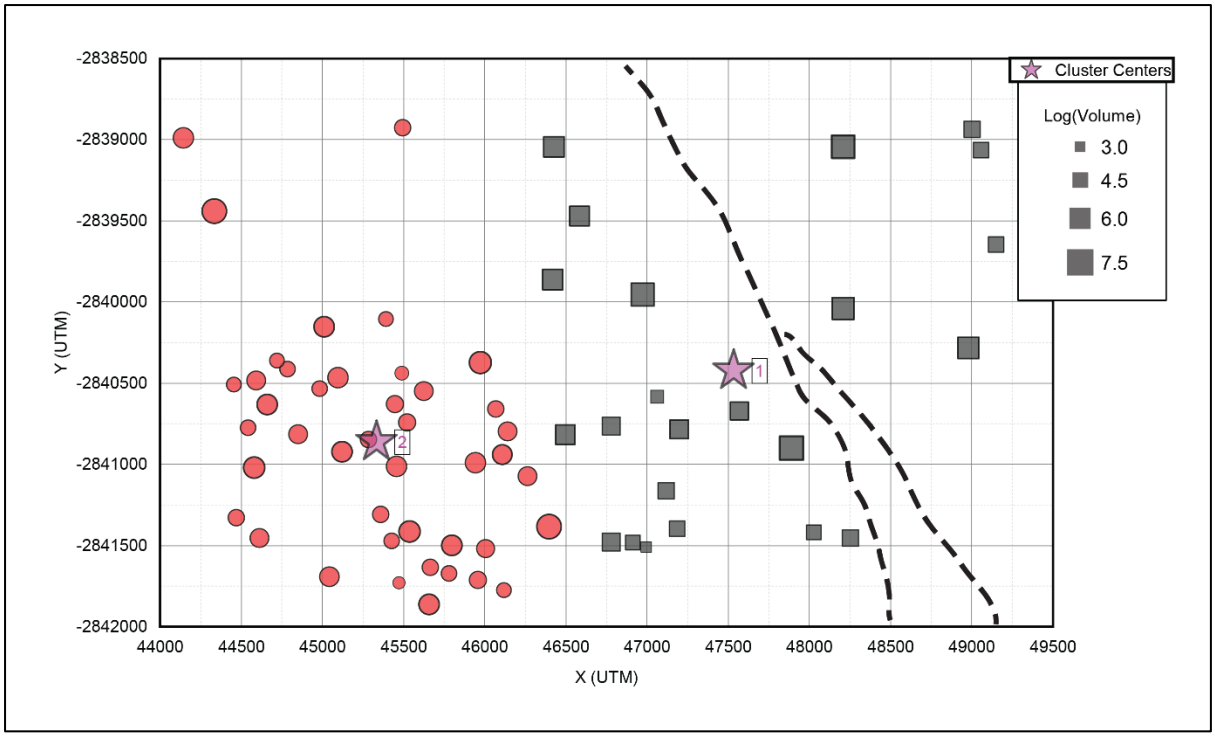

***Figure 6.13**. Distribution of the pothole clusters. The grey squares show members of cluster 1 and the cluster centre for member 1 is shown with the pink star labelled "1". The red circles show members of cluster 2 and the cluster centre for member 2 is shown with the pink star labelled "2". The black dashed line shows the location of the fault. Cluster 2's members are smaller than cluster 1's members. Also, the distribution of the pothole clusters suggests cluster 1's members are located around the major faults as the cluster centre is located approximately where the faults are and in case of cluster 2 there is no associated feature identified.*

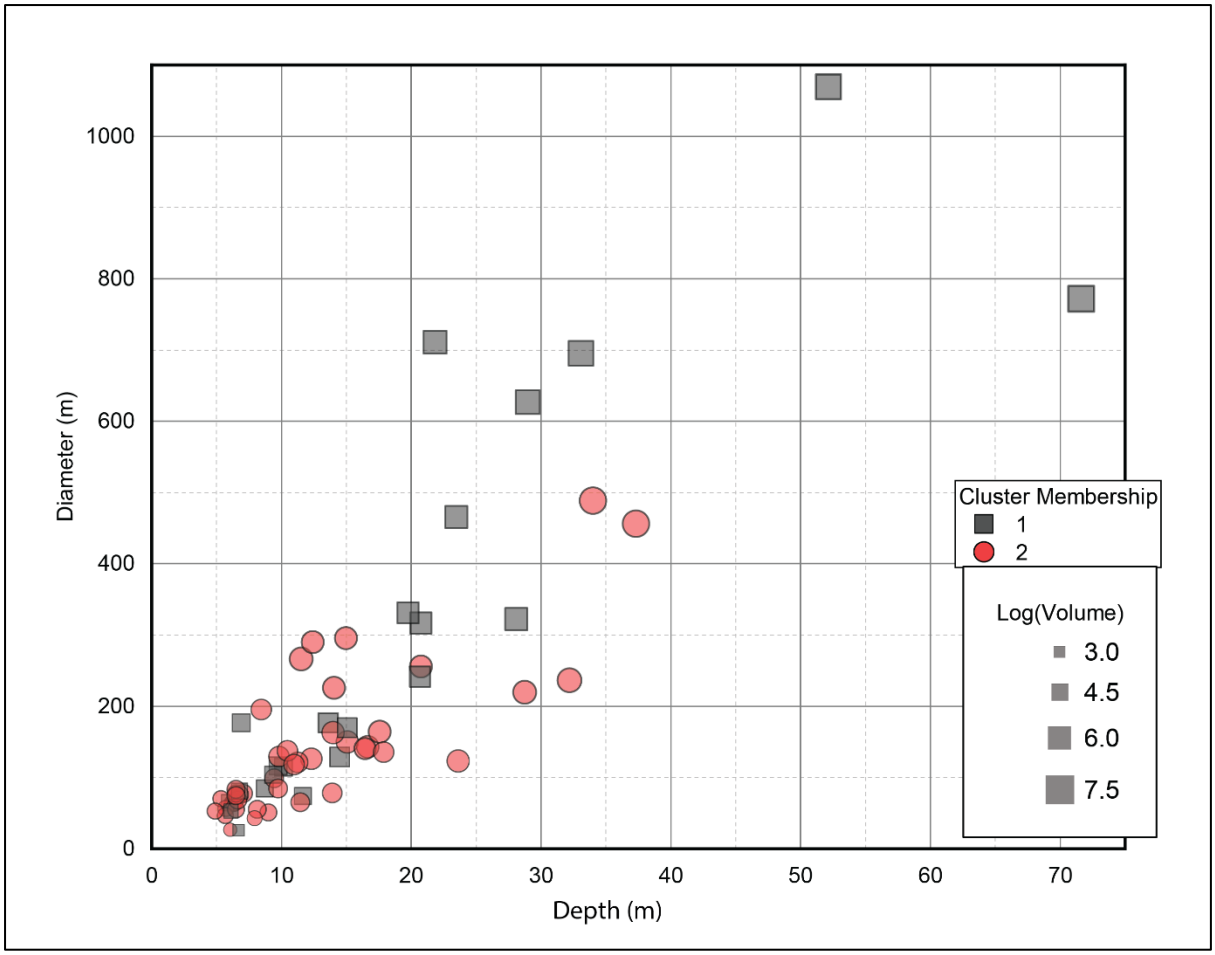

***Figure 6.14**. A graph showing the diameter vs. depth and the size of the data points represents the log of the volume of the potholes. The grey squares show potholes belonging to cluster 1 and the red circles show those of cluster 2. There is a positive correlation between the depth and the diameter of the potholes.*

6.4.3 Nearest neighbour analysis

An alternative method to the quadrant analysis is the nearest neighbour analysis. This analysis considers distances between the closest pairs of points within the data set (Davis, 2003). The analysis compares the characteristics of the observed nearest neighbours with the expected nearest neighbours, if the data were randomly distributed according to some theoretical pattern, such as a random pattern derived from the Poisson distribution. Using a numerical simulation by Donnelly (1978), the expected mean nearest neighbour distance ($\overline{\delta}$) is given by:

$$\bar{\delta} \approx \frac{1}{2}\sqrt{\frac{A}{n}} + \left(0.514 + \frac{0.412}{\sqrt{n}}\right)\frac{p}{n} \tag{28}$$

$$\approx \frac{1}{2}\sqrt{\frac{15}{43}} + \left(0.514 + \frac{0.412}{\sqrt{43}}\right)\frac{16}{43}$$

$$\approx 509.95\ m.$$

where A is the area of the study area, n is the number of potholes and p the perimeter of the rectangular study area. From the expected mean nearest neighbour distance, as well as the observed mean nearest neighbour distance (calculated as ~350.3 m from the box plot), the R-value for the nearest neighbour statistic could calculated. The R-value is given by:

$$R = \frac{\bar{d}}{\bar{\delta}}, \tag{29}$$

where $\bar{d}$ is the mean observed nearest neighbour distance and $\bar{\delta}$ is the mean expected nearest neighbour distance. The R-value is calculated to be 0.6869 ± 0.002. Since this value is close to unity, the spatial distribution of the potholes is comparable to predictions made by the Poisson model. Additionally, since this value is smaller than unity, it is probable that the potholes exhibit some clustering (Davis, 2003).

6.4.4 Kernel density distribution analysis

The kernel density estimation calculates the density of features within a predetermined neighbourhood for point data (Silverman, 1986). From the kernel distribution (Figure 6.15), it is observed that there are two main clusters of potholes; one of the clusters is situated at the bottom left of the map (values ranging from 2.370 to 3.640), while the other cluster is located slightly north of the previous cluster (values ranging from 1.420 to 2.370). The right-hand side of the map shows that there are less potholes in this region. However, the potholes on the right-hand side were much larger than those that are clustered (see Figure 6.1). The size of potholes is not considered in the classic kernel density distribution analysis.

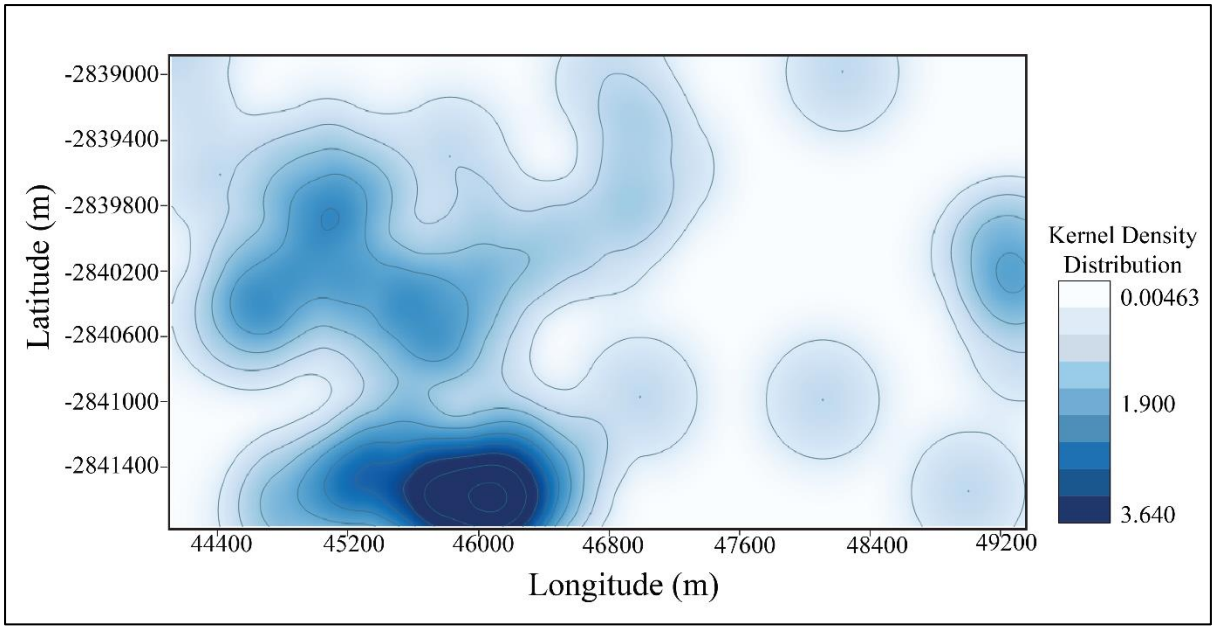

***Figure 6.15**. Kernel density distribution of the potholes showing two main clusters in the data. The one cluster has a distribution of 3.640 while the other ranges from 1.900 to 2.500.*

6.5 SUMMARY

In summary, a majority of the potholes that affect the Merensky Reef are also the same potholes found at the UG-2 level. That is, the same potholes appear to have propagated between the UG-2 and MR levels. This is a significant finding, since the vertical extent of the potholes is not in general, a geologically-constrainable measurement and any genetic models of the potholes clearly needs to accommodate for the stratigraphically-extended nature of the potholes in the Bushveld Complex. The shapes of the potholes vary, with the larger potholes having more irregular or oval shapes and the smaller potholes being more circular.

From the statistical analysis, two classes of potholes by size have been defined. Potholes with an area greater than ~1.5×10^5 m^2 or diameters greater than ~400 m were centred around the major fault. This suggests that the fault might have played a role during the formation of the

larger potholes. However, there were no identified faults in the vicinity of the smaller potholes, which could give more conclusive and general insights into the relationship between potholes and faults. The present data only support the association of large potholes and faults in the vicinity of the study area.

There is a possibly linear correlation between the depth and the diameter of the potholes as well as the depth and the area of the potholes. The smaller potholes are clustered into two main regions, suggesting that the potholes are not entirely randomly distributed. The arrangement of the large potholes suggests that they preferentially exist near or along the major fault and are elongated roughly in the direction of the fault.

The Shapiro-Wilk test and the Q-Q plots reveal that the logarithm of the potholes' volumes is substantially normal, which could mean that the potholes grew incrementally from smaller sizes, since this process naturally results in a log-normal distribution of sizes.

The quadrant analysis shows that the potholes are randomly distributed according to the Poisson model with some clustering. This clustering idea is additionally supported by a k-means cluster analysis and a kernel distribution analysis on the potholes. The k-means cluster analysis shows that there are probably two clusters of potholes, one cluster consists of larger potholes that are located predominately on the eastern portion of the map, and the other cluster consists of smaller potholes that are located predominately on the western portion of the map (Figure 6.13).

7 DISCUSSION

7.1 INTRODUCTION

Understanding the distribution and occurrence of potholes is of great value to both the academic and platinum mining industries. Mining companies, in particular, can use this information to evaluate or estimate resources and for future mine planning and design. In this study, several novel 3D seismic techniques were used to enhance detection of pothole structures that affect the platinum-bearing horizons. Furthermore, this study applied statistical methods to quantify the differences in pothole size, examine the relationship between potholes and other geological features (faults), as well as to understand the distribution of the potholes. The results clearly demonstrate the benefits of using multi-seismic and -statistical techniques in the identification of potholes in 3D reflection seismic data and revealing fascinating spatial characteristics of potholes. In this study small potholes referred to potholes with diameters below 300 m and large potholes referred to potholes with diameters greater than 300 m. Faults with throws above 25 m were referred to as large faults, while faults with throws less than 25 m were referred to as small faults.

7.2 COMPARISON OF VARIOUS SEISMIC ATTRIBUTES FOR THE DETECTION OF POTHOLES

In the past decade, seismic attributes have improved the quality of the seismic interpretation in both hard rock and soft rock settings (Manzi et al., 2012b). Previously the interpreter only made use of the amplitude map and attempted to manipulate the colour palette such that geological features could be highlighted (Herron, 2011). However, seismic interpretation derived from amplitude maps were not always successful, particularly in the structurally complex hard rock setting. Thus, to identify small potholes and small throw faults, conventional methods were augmented with seismic attributes.

Initially complex-trace attributes were applied to the 3D seismic data; which provided better mapping of the stratigraphy and faults in the area. The envelope and the instantaneous bandwidth attributes were the most optimal at revealing the major sequence boundaries. The envelope attribute is highly beneficial as it is able to detect major and small lithological changes that were difficult to see in the original seismic data. This is probably because phase is amplitude independent and it is thus not a good indicator of lithological changes. These complex-trace attributes allowed for more accurate picking of the horizons of interests. The enhanced understanding of the horizons provided by these attributes allowed for better tracking of the continuities of the horizons, which reduced errors caused by incorrect horizon picks.

Volumetric attributes were applied to the seismic volume to better understand the structural complexity of the area. In particular, areas that exhibited chaos in structure were identified using the chaos attribute. High chaos regions highlighted by this attribute corresponded to reflector disruptions, which allowed for the identification of the major fault zone and other geological features. Within the seismic volume, chaotic regions were located below larger potholes and near faults (Figure 5.33). These could be indicative of pegmatoids or other magmatic intrusions that flowed upwards into the Bushveld Complex (Viljoen et al., 1986a; Campbell, 2006)

In comparison, there was insignificant additional information provided by either the chaos attribute or the variance attribute over the other. However, together these attributes validated features that were present in the data. These attributes were also used as input during the computation of the ant-tracking attribute. With the ant-tracking attribute, a difference between features revealed by the chaos attribute and the variance attribute was observed.

The horizon attributes were crucial in the identification of the potholes. Due to the anticipated shape of the potholes, the dip and dip azimuth attributes were the first attributes computed for the seismic horizons. The dip attribute was good at highlighting the change in dip in the vicinity of potholes. The dip azimuth attribute struggled to highlight the smaller potholes. This is probably because the dip direction of the smaller potholes might be too small to be detected by the dip azimuth attribute. Edge detection attribute, which is a combination of the dip azimuth and dip attributes, succeeded in the detection and quantification of the size and shape of both small and large potholes. The curvature attribute was used to investigate the synclinal nature of the potholes. The potholes are known to be associated with a heap of adjacent material; however, this was not seen in the curvature attribute map. Hence, various horizon attributes worked together provided both an overlapping and exclusive seismic characteristic of the potholes.

7.3 SEISMIC ATTRIBUTES VS. SURFACES-BASED METHODS FOR POTHOLE IDENTIFICATION

Seismic attributes are a highly effective visual tool to identify potholes (Trickett et al., 2004; Campbell, 2006; Scheiber-Enslin and Manzi, 2018). However, exact sizes of potholes were not deducible from attribute-mapped sections, as adjacent potholes were merged into overlapping bright spots. The difference-of-two-surfaces method allowed for the clear identification of the shape and size of the potholes, however this method also introduced artefacts that were caused by Horizon manual and auto-picking.

In Chapter 6 it was shown that the shapes and sizes of the potholes were variable (e.g. the larger potholes were irregular or oval in shape and the smaller potholes were circular). This pattern was successfully identified by the difference-of-two-surfaces method. A similar relation was suggested by Hoffmann (2010), where the potholes' shape differed in relation to the size of the

potholes. Hoffmann (2010) also showed that potholes with diameters greater than 100 m tended towards an oval elongated shape in an approximate direction sub-parallel to the reef strike.

The difference-of-two-surfaces method also identified nearly twice the number of potential potholes present in the study area compared to those identified by the attributes-based method. However, a few of the potential potholes were below the spatial resolution of the seismic data; these were not confidently interpreted and were considered unusable for statistical analyses. Using the combination of these methods was beneficial, as it allowed for the verification and validation of the existence and shape of the potholes. In retrospect, it is recommended that the difference-of-two-surfaces method be implemented first, then followed by the application of the attributes-based method to the resulting surface.

7.4 POTHOLE AND FAULT ASSOCIATION AS HIGHLIGHTED BY THE SPATIAL AND CLUSTER ANALYSIS

There is a spatial relationship between the faults and the potholes, and particularly between the larger fault and the larger potholes. Inspection of the larger potholes revealed strong reflections that either crosscut the pothole or are visible beneath the pothole, which may be indicative of faults or pegmatoids or both (see Figure 5.33). Campbell (2011) noted that the potholes were often spatially associated with magmatic replacement of iron-rich ultramafic pegmatoids (IRUPs). Further to this, the data show that the cluster centre for the large potholes was essentially located on the major fault (Figure 6.13). These potholes with lineaments beneath do not occur only within the stratigraphy spanned by the Merensky and UG-2 reefs but can be traced down to lower regions, possibly through the floor of the Bushveld Complex (i.e. Transvaal Basin; Campbell, 2011). The termination of these potholes at depths in the seismic volume might be an indication of the base of the Bushveld Complex. Ballhaus (1988) used the

mine plan of the Brakspruit mine and found a coincidental relationship between the pothole distribution and the orientation of fractures, fault zone and dykes. However, further details about the nature of the relationship were not addressed.

Interestingly, the results from this study show that the smaller potholes have no relationship with crosscutting or underlying faults. Furthermore, it was observed that small potholes found at Merensky Reef propagated through to the UG-2 reef, although some reflections disturbances remain below both reefs (Figure 5.34). This observation is not in agreement with previous studies that suggested that there is no correlation between the potholes found in the Merensky and the UG-2 reefs (Chitiyo et al., 2008). Hoffmann (2010) noted that the larger potholes appear to superimpose onto both the Merensky and UG-2 reefs. However, the largest pothole in the study by Hoffmann (2010) was ~200 m in diameter and is considered a small pothole in this study. Hence, this would also support our analysis of the small potholes being located within the two reef horizons. This could suggest that the larger potholes formed as a result of a bigger phenomenon that was regional and made use of the faults as conduits. In this context, the smaller potholes formed from a more localised phenomenon, perhaps different to, although not entirely independent from that of the larger potholes. However, there may be smaller faults and extended structures beneath the small potholes that were not mapped as their throws fall below the resolution limit.

Inspection of the depth vs. diameter graph (Figure 6.4) and the distribution maps (Figure 6.6 and 6.13) suggest that the potholes nearest to the fault are deeper and become shallower away from the fault. Hoffmann (2010) identified a fault zone in his study area that separated the abundance of potholes (one side of the fault had many potholes the other had less potholes). The same separation may exist in this study area; however, the study area here is much smaller,

and the fault is not located in the middle. Hence, one is unable to validate the asymmetrical nature of the abundance of potholes around fault zones.

7.5 POTHOLE POPULATION

There is a possible linear correlation between the depth and the diameter of the potholes as well as the depth and the area of the potholes (see Figure 6.4 and 6.5). This may suggest that there was a single event, or single causal process that may have formed all the potholes, and that this process or event directly and simultaneously controlled the depth, area and diameter of each pothole, such that a larger area/diameter implies a greater depth of the potholes at a highly-consistent aspect ratio. To further examine this hypothesis, the physical data of the potholes could be fitted to a set of models for various anticipated magma chamber processes and their expected results. For example, if the potholes were the result of a surficial process such as scouring, then the process should produce aspect ratios that are different to those produced from a volumetric process, such as phase transformations or slumping.

Chitiyo et al. (2008) defined three pothole populations or classes (populations where small potholes are those with diameters less than 20 m; medium-sized potholes are those with diameters from 20 m to 500 m and; large potholes are those with diameters greater than 500 m). Spatial data from this study correlate with the work done by Chitiyo et al. (2008), in that the potholes can also be grouped roughly into diametrical classes. However, unlike Chitiyo et al. (2008), and possibly due to the limited number of potholes, only two classes were observed (Figures 6.4 and 6.5).

7.6 FORMATION OF POTHOLES AND THE IMPLICATION ON THE STATISTICAL ANALYSIS

Many researchers (e.g. Schmidt, 1952; King and MacLean, 1970; Ulmer et al., 1981; Elliott et al., 1982; Butin et al., 1985; Harrington, 1985; Boudreau, 1992; Kelley et al., 1994) have investigated how potholes formed within the Bushveld Complex. Here five hypotheses will be examined on the formation of potholes as well as to eliminate any of the hypothesis that contradicts the results in this study and to determine the possible mechanism(s) for the formation of the potholes.

7.6.1 Scouring structures due to convection currents

Schmidt (1952) proposed that during the formation of the crystal pile, currents flowing near the top caused wide swirling eddies. Schmidt (1952) also stated that during this time the viscosity of the magma was assumed to be low, as there were sulphides in the preserved rocks. The eddies picked up pyroxene crystals and cut through the underling rock which had not been completely consolidated. This swirling motion of the current resulted in cutting into the sides of the depressions horizontally rather than downwards.

7.6.2 Scars of fumaroles

Ulmer et al. (1981) and Elliott et al. (1982) proposed that potholes are the remaining scars of plutonic fumaroles. These fumaroles added fluid-rich volatile material (SO_2, H_2O, CO_2) that altered the fugacity ratio of the cumulate and caused depressions (Butin et al., 1985). In this hypothesis, the plutonic fumaroles occurred prior to the time of the economic horizons but continued to have formed the potholes within the economic horizons. These potholes were subsequently deepened by fluid mechanisms (Butin et al., 1985).

7.6.3 Volatile fluid overpressure

Boudreau (1992) proposed that as a fluid separates from the intercumulus liquid faster than it can escape from the crystal pile, the fluid experiences an increase in pressure, resulting in a

fluid overpressure. This leads to an increase in pore pressure that forces the fluids up through the crystal pile creating doming structures (Boudreau, 1992). Following the doming structures, continuous overpressure results in a rupture in the dome causing an explosion and the escape of fluids. The potholes result from the explosive nature of the fluid escapes and the melting is caused by a reaction of the crystal pile with the volatiles.

Boudreau (1992) also compared potholes to pockmarks. Pockmarks are defined as concaved, crater-like depressions that generally have diameters that are 30 – 40 m across and reach 2 – 3 m depth (King and MacLean, 1970; Harrington, 1985; Kelley et al., 1994). However, Forwick et al. (2009) suggested that pockmarks were "generally hundreds of meters in diameter and tens of meters in relief". Mega pockmarks are defined as pockmarks with diameters greater than 1.5 km and depths greater than 150 m (Pilcher and Argent, 2007; Forwick et al., 2009). Pockmarks are commonly found on continental shelves, slopes and deep-sea beds (King and MacLean, 1970; Josenhans et al., 1978; Fader, 1991; Piper et al., 1999, Paull et al., 2002; Loncke et al., 2004; Hovland, 2005; Gay et al., 2007; Forwick et al., 2009). They are associated with silty clay and material with large water contents (Harrington, 1985). The formation of pockmarks has been associated with seepage of thermogenic and biogenic gases from the marine subsurface to the seafloor (Rogers, et al., 2006; Forwick et al., 2009; Mahiques et al., 2017) and the release of pore water (Harrington, 1985; Forwick et al., 2009).

7.6.4 Fluid dynamic model

Campbell (1986) and Irvine et al., (1983) proposed that potholes formed through thermochemical erosion. Campbell (1986) suggested that new pulses of magma entered the magma chamber during crystallization of some pre-existing magma. However, the new magma was hot and of different chemical composition to the pre-existing magma. The mixture of the

new magma and the cumulate pile produced a hybrid magma (Lomberrg et al., 1999). This hybrid magma melted the cumulate floor. Where the density contrast is such that the melted floor material is lighter than the surrounding magma, the lighter magma is swept away by compositional convection and replaced by hot uncontaminated melt. This process forms a positive-feedback thermochemical erosion loop (Campbell, 1986).

7.6.5 Sites of non-deposition of cumulus crystals

Ballhaus (1988) proposed that potholes formed where dissolved volatiles (SO_2, H_2O, CO_2) locally lowered the liquidus temperature of plagioclase, preventing cumulate materials from crystallizing (Ballhaus, 1988; Boudreau, 1992). This caused part of the footwall cumulates to not form. Hence, the economic horizons within the magma chamber would have had to crystallize at a lower stratigraphy.

7.6.6 Summary

Based on the results from this study, immediately two pothole formation hypotheses are considered as improbable, namely the scouring due to convention currents and the fluid dynamic hypotheses. This is because 3D seismic analyses conclusively determined that the potholes found on the Merensky and the UG-2 reefs are identical, and even small potholes feature vertically-extended structures below the reefs. It would seem greatly unlikely that the convection currents were undisturbed between the Merensky and the UG-2 reefs. Instead, one would have expected that the potholes were randomly distributed in depth and vertically-restricted to individual units in the stratigraphy in an uncorrelated manner.

Furthermore, the larger potholes are centrally clustered around the major fault, which seems to be a feature of total irrelevance in either hypothesis. These faults could have only occurred

during the post-magmatic stage, when the crystal cumulates are almost completely solid. Hence, if the formation of the potholes is related to the fault, then the fluid dynamic and scouring mechanisms could not have been be contemporaneous with this unknown formation mechanism. However, the nature of the potholes' spatial correlation with the fault is not known and whether or not all potholes are spatially related to faults is not deducible from the results of this study.

The non-deposition of cumulus minerals hypothesis is difficult to assess. In particular, the reflectors are curved in the vicinity of the potholes, but not absent. This could imply that the stratigraphic units are locally depressed, but the material is not always removed in the vicinity of the potholes. However, this seismic evidence cannot support nor reject this hypothesis.

The fumarole model can explain the clusters found in the cluster analysis, the affinity of potholes to certain seismic sections, and the vertically-extended nature of potholes across the stratigraphy and particularly crossing both the Merensky and UG-2 reefs, and possibly the chaotic reflectors below some of the potholes. This is because the chaotic regions identified in the seismic sections could be pegmatites or magmatic intrusions, which released the volatiles. Also, the magmatic intrusions would have been located at a specific place at depth and thus limited the pathways of the volatiles. The fumarole hypothesis suggests that the footwall sediments were locally uplifted as the volatiles rose and resulted in anticlines near the potholes. However, in the seismic sections (e.g. Figure 5.27), there is either no evidence of any uplift near the potholes to within resolution-limit of the data. Additionally, one would not expect erosion or transport to have taken place to account for the lack of sediments. A similar argument can be applied to the volatile overpressure hypothesis as it also does not directly address the

transport of sediments. However, the lack of a mechanism of transport does not eliminate either hypothesis conclusively, as more than one mechanism could have operated during the formation of the potholes.

Given the findings, either multiple mechanisms or some undiscovered mechanism(s) is the most probable cause of the formation of the potholes. For example, volatiles released from below the last-deposited cumulate layer may have occurred prior to magma recharge, which drove convection in the magma chamber and scoured away some of the loosely-redeposited surface material (Campbell, 1986). Alternatively, the release of volatiles was slow and sustained through some period inside the magma chamber, and this sustained release of volatiles drove highly-localized convection cells that slowly scoured the vicinity of the cumulate-magma interface (Ballhaus, 1988). Part of the fault may have occurred in the vicinity of a previously-weakened zone, due to either magmatic or volatile movements.

The statistical data for the potholes suggests several major findings that may be important to conclusively understand the formation mechanism(s) of the potholes. The first finding is the linear relationship between the diameter and the depth of the potholes. This finding seems to suggest that the potholes grew simultaneously both in width and depth. Hence, any probable formation mechanism needs to take into account the three-dimensional growth of the potholes. The second finding is that the volume of the potholes is highly probably log-normally distributed. Log-normally-distributed object sizes result from many natural growth processes where small percentage changes are additive on a log-scale. This finding suggests that potholes grew at a rate that is linearly proportional to their three-dimensional sizes. Furthermore, this

suggests that all the identified potholes experienced a similar growth rate and strongly hints at the possibility that a single set of mechanisms formed all potholes.

The third finding is the random distribution of the potholes in the study area, and in particular, the two-dimensional distribution of the potholes can be adequately modelled by a Poisson distribution. If the fault is related to the formation of the potholes, then no statistical support can be inferred from our data and another approach is probably warranted to examine this link further. If the clustering of smaller potholes is representative of potholes in general, then it suggests that there may still be some order within their seemingly-random distribution. With a large enough dataset, it may be possible to conclusively link the fault and the larger potholes and identify the spatial relationship between the smaller potholes.

8 CONCLUSIONS

The aim of the project was to identify potholes within the Western Limb of the Bushveld Complex, investigate the spatial distribution, and development of potholes using 3D reflection seismic data sourced from Lonmin Platinum. Two main seismic techniques were used to identify the potholes namely: (i) the seismic attribute and (ii) the difference-of-two-surfaces. The use of seismic attributes was of vital importance in the interpretation of this study area and the understanding of seismic and geological characteristics of the potholes. Subsequently, the physical properties of the potholes were examined with several statistical methods. Lastly, the feasibility of various hypotheses for the formation of the potholes and constrained necessary conditions from the findings of the combined seismic-statistical analyses for any successful hypothesis was examined. From this project it can be concluded that there are many benefits to applying a variety of seismic attributes for a given problem as they all have their strengths and weaknesses (e.g. the ant-tracking was good at mapping fractures around the fault zone).

Furthermore, the potholes were found to be asymmetrical in shape on the cross-section and sometimes have association with faulting. In this study it was determined that, a majority of the potholes that affect the Merensky Reef are also the same potholes found at the UG-2 level. These identified potholes were found to be randomly distributed according to the Poisson model with some clustering (2 clusters were identified one was located in the centre while one was located within the major fault).

Although there are many proposed hypotheses regarding the formation of potholes, given the findings of both the seismic data and the statistical analysis either multiple mechanisms or some undiscovered mechanism(s) is the most probable cause of the formation of the potholes.

The statistical data for the potholes provided an understanding for the formation mechanism(s) of the potholes. The first finding is the linear relationship between the diameter and the depth of the potholes. This seems to suggest that the potholes grew simultaneously both in width and depth. The second finding is that the volume of the potholes is highly probably log-normally distributed. This finding suggests that potholes grew at a rate that is linearly proportional to their three-dimensional sizes. The third finding is that the random distribution of the potholes in the study area can be adequately modelled by a Poisson distribution. From the data presented in this study, there is no statistical support that can relate the fault to the formation of the potholes.

Even though this project looked at many different aspects, further work is still needed. A larger study area is required, perhaps one with more faults in order to investigate the relationship between the fault and the potholes statistically. This project was limited by the lack of borehole data and mine map data. This would be an integral part in the validation of the work that was done.

References

Azevedo, L and Pereira, G.R. (2009). Seismic Attributes in Hydrocarbon Reservoir Characterization. University of Aveiro, Department of Geoscience, 54 – 119.

Ballhaus, C.G. (1988). Potholes of the Merensky Reef at the Brakspruit Shaft, Rustenburg Platinum Mines; primary disturbances in the magmatic stratigraphy. *Economic. Geology*, **83**(6), 1140 – 1158.

Barnes, A.E. (1999). Seismic attributes past, present, and future. *Society of Exploration Geophysicists Technical Program Expanded Abstracts*, 892 – 895.

Barnes, A.E. (1991). Instantaneous frequency and amplitude at the envelope peak of a constant phase wavelet. *Geophysics*, **56**(7), 1058–1060.

Barnes, A.E. & Laughlin, K. (2002). Investigation of methods for unsupervised classification of seismic data. Proceedings from *72th Annual International Meeting. Society of Exploration Geophysicists Expanded Abstracts*, 2221 – 2224.

Barnes, A.E. (2007). Redundant and useless seismic attributes. *Geophysics*, **72**(3), 33 – 38.

Barnes, A.E. (2016). Handbook of Poststack Seismic Attributes. U.S.A: *Society of Exploration Geophysicists*, 2 – 183.

Brabham, P.J., Thomas, J., & McDonald, R.J. (2005). The terrestrial shallow seismic reflection techniques applied to the characterization and assessment of shallow sedimentary environments. *Journal of Engineering Geology and Hydrogeology*, **38**, 23 – 38.

Brown, A.R. (2001). Understanding seismic attributes. *Geophysics*, **66**(1), 47 – 48.

Buntin, T.J., Grandstaff, D.E., Ulmer, E.G., & Gold, D.P. (1985). A pilot study of geochemical and redox relationships between potholes and adjacent normal Merensky Reef of the Bushveld Complex. *Economic Geology*, **80**(4), 975 – 987.

Burger, H.R. (1992). Exploration Geophysics of Shallow Subsurface. Eaglewood Cliffs: Prentice-Hall, 489.

Campbell, G., & Crotty, J.H. (1990). 3-D seismic mapping for mine planning purposes at the South Deep Prospect. In: Ross-Watt, D. A. J., & Robinson, P. D. K., (Eds.), *Proc. Internat. Deep Mining Conf.: Southern African Institute of Mining and Metallurgy Symposium Series S10*, **2**, 569 – 597.

Campbell, G. (1994). Geophysical contributions to mine-development planning: A risk reduction approach. In: Anhaeusser, C.R. (Ed.), *Proc. XVth CMMI Congress: Southern African Institute of Mining and Metallurgy Symposium Series* S14, **3**, 283 – 325.

Campbell, G. (2006). High resolution aeromagnetic mapping of 'loss-of-ground' features at platinum and coal mines in South Africa: *South African Journal of Geology*, **109**, 439–458.

Campbell, G. (2011). Exploration geophysics of the Bushveld Complex in South Africa: The Leading Edge Special Section. Africa: *Society of Exploration Geophysicists*, **30**(6), 622 – 638.

Campbell, I.H. (1986). A fluid dynamic model for the potholes of the Merensky Reef. *Economic Geology*, **81**(5), 1118 – 1125.

Carr, H.W., Groves, D.I., & Cawthorn, R.G. (1994). Controls on the distribution of Merensky Reef potholes at the Western Platinum Mine, Bushveld Complex, South

Africa: implications for disruptions of the layering and pothole formation in the Complex. *South African Journal of Geology,* **97**(4), 431 – 441.

Cawthorn, R.G., Merkle, R.K.W., & Viljoen, M.J. (2002). Platinum-Group element deposits in the Bushveld Complex, South Africa. In: L.J. Cabri. (Ed.), The Geology, Geochemistry, Mineralogy and Mineral Beneficiation of Platinum-Group elements, CIM Special Volume **54**. *Canadian Institute of Mining, Metallurgy and Petroleum*, 54.

Cawthorn, G. (2010). The Platinum Group Element Deposits of the Bushveld Complex in South Africa. *Platinum Metals Review*, **54**(4), 205 – 215.

Cheney, E.S., & Twist, D. (1991). The comfortable emplacement of the Bushveld mafic rocks along a regional unconformity in the Transvaal succession of South Africa. *Precambrian Research,* **52**(1-2), 115 – 132.

Chitiyo, G., Schweitzer, J., de Waal, S., Lambert, P., & Olgilvie, P. (2008). Predictability of pothole characteristics and their spatial distribution at Rustenburg Platinum Mine. *Journal of Southern African Institute of Mining and Metallurgy*, **108**(12), 733 – 740.

Chun, J.H and Jacewitz, C.A. (1981). Fundamentals of frequency domain migration *Geophysics*, **46**(5), 717 – 733.

Chopra, S., Castagna, J., & Portniaguine, O. (2006). Seismic resolution and thin-bed reflectivity inversion. *CSEG Recorder*, 19 – 25.

Chopra, S., & Marfurt, K.J. (2007). Seismic Attribute for Prospect Identification and Reservoir Characterization: Geophysical Developments Series. U.S.A: *Society of Exploration Geophysicist*, 1 – 22.

Cox, T., & Seitz, K. (2007). Ant Tracking Seismic Volumes for Automated Fault Interpretation. Calgary, Alberta, Canada: *CSPG/CSPE GeoConvention*.

Dalley, R.M., Gevers, E.C.A., Stampfli, G.M., Davies, D.J., Gastaldi, C.N., Ruijtenberg, P.A., & Vermeer, G.J.O. (1989). Dip and azimuth displays for 3D seismic interpretation. *First Break*, **7**(3), 1 – 10.

Davis, J.C. (2002). Statistics and data analysis in geology (3rd ed.). New York: John Wiley & Sons, 229 – 313.

Davison, G.E., & Chunnett, G.K. (1999). Seismic exploration for Merensky Reef: The way ahead. *Transactions – Geological Society of South Africa*, **102**(3), 261 – 267.

Durrheim, R.J., & Maccelari, M.J. (1991). Seismic exploration for precious metals in the hard rock environment: 61st Annual International Meeting. *Society of Exploration Geophysicists Technical Program Expanded Abstracts*, 159 – 162.

Durrheim, R.J., & Linzer, L.A. (2014). The use of seismic and magnetotelluric methods to investigate the crust and upper mantle. Course presented in Rio de Janerio, 24 – 32.

Elliot, W.C., Grandstaff, D.E., Ulmer, G.C., Buntin, T., & Gold, D.P. (1982). An intrinsic oxygen fugacity study of platinum- carbon associations in layered intrusions. *Economic Geology*, **77**(6), 1493 – 1510.

Farquhar. J. (1986). The Western Platinum Mine. In Anhaeusser. C.R. and Maske, S. (Eds), Mineral Deposits of Southern Africa. Johannesburg. *Geological Society of South Africa*, 1135 – 1142.

Fehmers, G.C., & Hocker, C.F. (2003). Fast structural interpretation with structure-oriented filtering. *Geophysics*, **68**(4), 1286 – 1293.

Free, M.L. (2001). Platinum Group Metals: Past and Present. *Platinum-Group Metals. Commentary*, 10.

Gardner, G.H.F. (Ed.). (1985). Migration of Seismic Data. Tulsa, Oklahoma: *Society of Exploration Geophysicists Monograph Series*, 462.

Gazdag, J., & Squazzero, P. (1984). Migration of Seismic Data: Invited Paper. *Proceedings of the Institute of Electrical and Electronics Engineers*, **72**(10), 1302 – 1307.

Hale, D. (1992). Migration by the Kirchhoff, slant stack, and Gaussian beam methods. United States: *Project Review*, 1 – 18.

Harmer, R.E., & Armstrong, R.A. (2000). New precise dates on the acid phase of the Bushveld and their implications. Abstract. Burgersfort: University of the Witwatersrand, Johannesburg.

Herron, D.A. (2011). First Steps in Seismic Interpretation. U.S.A: *Society of Exploration Geophysicists*, 27 – 81.

Hoffmann, D. (2010). Statistical size analysis of potholes: an attempt to estimate geological losses ahead of mining at Lonmin's Marikana mining district. Proceedings from the 4th International Platinum Conference: Platinum in transition 'Boom or Bust'. *The Southern African Institute of Mining and Metallurgy*, 97 – 104.

Hunt, J.P. (2006). Geological Characteristics of Iron Oxide-Copper-Gold (IOCG) Type Mineralisation in the Western Bushveld Complex (Master's by dissertation). University of the Witwatersrand, Johannesburg.

Hunter, D.R., & Hamilton, P.J. (1978). The Bushveld Complex. In: D.H. Tarling (Ed.), Evolution of the Earth's crust. London: *Academic Press*, 107 – 173.

Huysamen, G.K. (1981). Introductory statistics and research design for the Behavioural Sciences (7th ed.). Cape Town: National book printers, Goodwood, **2**, 22 – 60.

Irvine, T.N., Keith, D.W., & Todd, S.G. (1983). The J-M platinum-palladium reef of the Stillwater Complex, Montana: II. Origin by double-diffusive convective magma mixing and implications for the Bushveld Complex. *Economic Geology*, **78**(7), 1287 – 1334.

Kearey, P., Brooks, M., & Hill, I. (2002). An Introduction to Geophysical Exploration. London: Blackwell Science, 21 – 85.

Khair, H.A., Cooke, D., Backé, G., King, R., Hand, M., Tingay, M., & Holford, S., (2012). Subsurface mapping of natural fracture networks; a major challenge to be solved. Case study from the shale intervals in the cooper basin, south Australia. Proceedings from *the thirty-seventh Workshop on geothermal reservoir engineering*. Stanford, California: Stanford University.

Kinloch, E.D. (1982). Regional trends in the platinum-group mineralogy of the critical zone of the Bushveld Complex, South Africa. *Economic Geology*, **77(6)**, 1328 – 1347.

Kinnaird, J. (1982). The Bushveld Large Igneous Province. Johannesburg: University of the Witwatersrand. Retrieved from: [WWW]. http://www.largeigneousprovinces.org/sites/default/files/BushveldLIP.pdf.

Koson, S., Chenrai, P., & Choowong, M. (2014). Seismic Attributes and Their Applications in Seismic Geomorphology. *Bulletin of Earth Sciences of Thailand*, **6**(1), 1 – 9.

Larroque, M., Postel, J.J.P., Slabbert, M., and Duweke, W. (2002). How 3D seismic can help enhance mining. *First Break*, **20**(7), 472-475.

Lenhardt, N., & Eriksson, P.G. (2012). Volcanism of the Palaeoproterozoic Bushveld Large Igneous Provinces: the Rooiberg Group, Kaapvaal Craton, South Africa. *Precambrian Research special volume for Wulf Mueller*, 3 – 11.

Li, J., & Heap, A.D. (2014). Spatial interpolation methods applied in the environmental sciences: A review. *Environmental Modelling & Software*, **53**, 173 – 189.

Lloyd, S. P., (1982). Least squares quantization in PCM. *Institute of Electrical and Electronics Engineers Transactions on Information's Theory*, **28** (2), 129 – 137.

Lomberg, K.G., Martin, E.S., Patterson, M.A., & Venter, J.E. (1999). The morphology of potholes in the UG-2 Chromitite layer and Merensky Reef (pothole reef facies) at Union Section, Rustenburg Platinum Mines. *South African Journal of Geology*, **102**(3), 209 – 220.

Malehmir, A., & Bellefleu, G. (2009). 3D seismic reflection imaging of volcanic-hosted massive sulfide deposits: Insights from reprocessing Halfmile Lake data, New Brunswick, Canada. *Geophysics*, **74**(6), 209 – 219.

Malehmir, A., Durrheim, R.J., Bellefeur, G., Urosevic, M., Juhlin, C., White, D.J., & Campbell, G. (2012). Seismic methods in mineral exploration and mine planning: A general overview of past and present case histories and a look into the future. *Geophysics*, **77**(5), 173 – 190.

Manzi, M.S.D., Gibson, M.A.S., Hein, K.A.A., King, N. & Durrheim, R.J. (2012a). Application of 3D seismic techniques to evaluate ore resources in the West Wits Line goldfield and portions of the West Rand goldfield, South Africa. *Geophysics*, **77**(5), 163 – 171.

Manzi, M.S.D., Durrheim, R.J., Hein, K.A.A., & King, N. (2012b). 3D edge detection seismic attributes used to map potential conduits for water and methane in deep gold mines in the Witwatersrand basin, South Africa. *Geophysics*, **77**(5), 133 – 147.

Manzi, M.S.D., Hein, K.A.A., Durrheim, R.J., King, N. (2013). Seismic attribute analysis to enhance detection of thin gold-bearing reefs: South Deep gold mine, Witwatersrand basin, South Africa. *Journal of Applied Geophysics*, **98**, 212 – 228.

Manzi, M.S.D., Hein, K.A.A., Durrheim, R.J., & King, N. (2014). The Vendersdorp Contact Reef model in the Kloof Gold Mine as derived from 3D seismics, geological mapping and exploration borehole datasets. *International Journal of Rock Mechanics and Mining Science*, **66**, 97 – 113.

Manzi, M.S.D., Durrheim, R.J., & Webb, S. (2017). 3D seismic attributes for platinum exploration and mine planning in the Bushveld Complex (South Africa). CGS/SEG International Geophysical Conference. Qingdao, China: *Society of Exploration Geophysicists and Chinese Petroleum Society*, 665 – 668.

Marfurt, K.J. (2015). Techniques and best practices in multiattribute display. *Interpretation*, **3**, 1 – 23.

McCarthy, T., & Rubidge, B. (2005). The story of Earth and Life. Struik Nature, Cape Town, 121 – 128.

Michell, A.A., & Scoon, R.N. (2007). The Merensky Reef at Winnaarshoek, Eastern Bushveld Complex: A Primary Magmatic Hypothesis Based on a Wide Reef Facies. *Economic Geology*, **102**(5), 971 – 1009.

Milkereit, B., Eaton, D., Wu, J., Perron, G, Salisbury, M.H., Berrer, E.K., & Morrison, B.G. (1996). Seismic imaging of massive sulphide deposits; Part II, Reflection seismic profiling. *Economic Geology*, **91**(5), 829 – 834.

Milkereit, B., Berrer. E.K., King, A.R., Watts, A.H., Roberts, B., Adams E., & Salisbury, M.H. (2000). Development of 3-D seismic exploration technology for deep nickel-copper

deposits — A case history from the Sudbury basin. Special Section. Canada: Mining Geophysics, *Geophysics*, **65**, 1890 – 1899.

Miller, R.D., Anderson, N.L., Feldman, H.R., & Franseen, E.K. (1995). Vertical resolution of a seismic survey in stratigraphic sequences less than 100 m deep in southeastern Kansas. *Geophysics*, **60**(2) 423 – 430.

Miningtek, C.S.I.R. (1997). Evaluate the potential of various high-resolution geophysical techniques to map out disruptions to platinum reefs; Project GE9604. Confidential report commissioned by Amplats, Gold Fields South Africa and Implats.

Moraleda, L.A.R., Escalona, A., Schulte, L., & Sayghe, S.A. (2015). Interpretation, modelling, and halokinetic evolution of salt diapirs in the Nordkapp Basin (Master's by dissertation). University of Stavanger, 23 – 46.

Ngeri, A.P., Tamunobereton-ari, I. & Amakiri, A.R.C. (2015). Ant-Tracking Attributes: An Effective Approach to Enhancing Faultidentification and Interpretation. *IOSR Journal of VLSI and Signal Processing*, **5**(6), 67 – 73.

Odgers, A.T.R., Hinds, R.C., & Von Gruenewaldt, G. (1993). Interpretation of a seismic reflection survey across the southern Bushveld Complex. *South African Journal of Geology*, **96**(4), 205 – 212.

Paradigm. (2013). Subsalt Imaging using 3D Pre-Stack Depth Migration Aided by Gravity Modeling in Onshore Germany. Retrieved from: [www] https://www.pdgm.com/products/migrations/

Pedersen, S.I., Randen, T., Sonneland, L., & Steen, O. (2002). Automatic fault extraction using artificial ants. In: 72nd Annual International Meeting of the Society of Exploration

Geophysicists Expanded Technical Program Abstracts with Biographies. Tulsa: *Society of Exploration Geophysicists*, 512 – 515.

Pereira, L.A.R. (2009). Seismic Attributes in Hydrocarbons Reservoirs Characterization (Masters by dissertation). University of Aveiro.

Pigott, J.D., Kang, M.H., & Han, H.C. (2013). First order seismic attributes for clastic seismic facies interpretation: Examples from the East China Sea. *Journal of Asian Earth Sciences*, **66**, 34 – 54.

Pretorius, C.C., Trewick W.F., Fourie, A., & C. Irons. (2000). Application of 3-D seismics to mine planning at Vaal Reefs gold mine, number 10 shaft, Republic of South Africa. *Special Section - Mining Geophysics*. *Geophysics*, **65**, 1862 – 1870.

Randen, T., Pedersen, S.I., & Sønneland, L. (2001). Automatic Extraction of Fault Surfaces from Three-Dimensional Seismic Data. *SEG Technical Program Expanded Abstracts*, 551 – 554.

Randen, T., & Sønneland, L. (2005). Atlas of 3D Seismic Attributes. In: Iske, A. and Randen, T.(Eds.). Mathematical Methods and Modelling in Hydrocarbon Exploration and Production. Berlin: Springer, 23 – 46.

Rijks, E.J.H. & Jauffred, J.C.E.M. (1991). Attribute extraction: An important application in any detailed 3D interpretation study. *The Leading Edge of Exploration*, **10**(9), 11 – 19.

Robertson, J.D., & Fisher, D.A. (1988). Complex seismic trace attributes. *Geophysics*, **7**(6), 22 – 26.

Rene, R.M., Fittert, J.L., Forsyth, P.M., Kim, K.Y., Murray, D.J., Walters, J.K., & Westerman, J.D. (1986). Multicomponent seismic studies using complex trace analysis. *Geophysics*, **51**(6), 1235 – 1251.

Quora. (2018). Which seismic wave is the most dangerous? Why?. [ONLINE] Available at: https://www.quora.com/Which-seismic-wave-is-the-most-dangerous-Why. [Accessed 10 May 2019].

Scheiber-Enslin, S.E. and Manzi, M.S.D. (2018). Integration of 3D reflection seismics and magnetic data for deep platinum mine planning and risk mitigation: a case study from Bushveld Complex, South Africa, *Exploration Geophysics*, **49**(6), 928 – 939.

Schlumberger. (2015). The Oilfield Glossary: Where the oil field meets the dictionary. Retrieved from: [WWW]. http://www.glossary.oilfield.slb.com/Terms/v/velocity_analysis.aspx.

Schmidt, E.R. (1952). The structure and composition of the Merensky Reef and associated rocks in the Rustenburg platinum mine. *Geological Society of South Africa Transactions*, **55**, 234 – 270.

Schouwstra, R.P. & Kinloch, E.D. (2000). A short Geological Review of the Bushveld Complex. *Platinum Metals Special Section - Mining Geophysics*, **44**, 33 – 39.

Schuster, G.T. (2007). Basics of Seismic Wave Theory, University of Utah.

Shearer, P.M. (2009). Introduction to Seismology. New York, U.S.A: Cambridge University Press, 2 – 5.

Shearer, P.M. (2010). Introduction to Seismology: The wave equation and body waves. San Diego: University of California, 1 – 13.

Sheriff, R.E. (2002). Encyclopedic Dictionary of Applied Geophysics. U.S.A: *Society of Exploration Geophysicists*, 25 – 400.

Silverman, B.W. (1986). Density Estimation for Statistics and Data Analysis. New York: Chapman and Hall.

Skov, T., Perdensen, T., Valen, T., Fayemendy, P., Gronlie, A., Hansen, J., Hetlelid, A., Inversen, T., Randen, T., & Sonneland, L. (2003). Fault Systems Analysis Using a New Interpretation Paradigm. Proceeding from *EAGE 65th Conference & Exhibition*, Stavanger, Norway.

South African Committee for Stratigraphy (SACS) (1980). Stratigraphy of South Africa. Part 1. In: L.E. Kent (Compiler), *Lithostratigraphy of the Republic of South Africa*. *Handbook Geological Survey of South Africa*, **8**, 690.

Stevenson, F., Higgs, R.M.A. & Durrheim, R.J. (2003). Seismic Imaging of Precious and Base-Metal Deposits in Southern Africa. In: Eaton D., Milkereit B. and Salisbury M.H. (Eds.), *Hardrock Seismic Exploration*. U.S.A*: Society of Exploration Geophysicists*, 141 – 156.

Stewart, S. (1999). Migration in practice. Retrieved from: [WWW]. http://www.xsgeo.com/course/mig.htm#prestack.

Stoodley, K.D.C. (1974). Basic Statistical Techniques for Engineering and Science Students. Great Britain, The Pitman Press, 108 – 115.

Taner, M.T., Koehler, F., & Sheriff, R.E. (1979). Complex seismic trace analysis. *Geophysics*, **44**(6) 1041 – 1063.

Taner, M.T., & Sheriff, R.E. (1977). Application of amplitude, frequency, and other attributes to stratigraphic and hydrocarbon determination: section 2. Application of seismic reflection configuration to stratigraphic interpretation. *American Association of Petroleum Geologists Memoir*, **26**, 301 – 327.

Taner, M.T., Koehler, F., & Sheriff, R.E. (1979). Complex seismic trace analysis. *Geophysics*, **44**(6), 1041 – 1063.

Taner, M.T. (2001). Seismic Attributes. *Canadian Society of Exploration Geophysicists Recorder*, **26**(7), 48 – 56.

Taylor, S. (2012). Introduction to Faults. Retrieved from: [WWW]. https://www.wou.edu/las/physci/taylor/es406_structure/TM_chap4_Faults.pdf.

Trickett, J.C., Düweke, W.A., & Kock, S. (2004). Three-dimensional reflection seismics: worth its weight in platinum: International Platinum Conference 'Platinum Adding Value', *The South African Institute of Mining and Metallurgy*, 257 – 64.

Trickett, J., Düweke, W., Linzer, L., Kock, S., & Tootal, K. (2009). From aspirin to "the bin" in a mere 85 years. Proceedings from the *11th SAGA Biennial Technical Meeting and Exhibition*, 303 – 310.

Uken, R. (1998). The geology and structure of the Bushveld Complex metamorphic aureole in the Olifants River area (Unpublished PhD thesis). Durban: University of Natal.

Van der Kurk, J. (2005). Reflection Seismic. Institute of Geophysics, Germany, 18 – 51.

Van Schoor, M. (2005). The application of in-mine electrical resistance tomography (ERT) for mapping potholes and other disruptive features ahead of mining. *Journal of the Southern African Institute of Mining and Metallurgy*, **105**(6), 447 – 452.

Viljoen, M.J., & Hieber, R. (1986). The Rustenburg Section of Rustenburg Platinum Mines Limited, with reference to the Merensky Reef. In: C. R. Annhaeuser and S. Maske, (Eds.). *Mineral Deposits of South Africa Volume II*. Geological Society of South Africa, 1107 – 1134.

Viljoen, M.J. (1994). A review of regional variations in facies and grade distribution of the Merensky Reef, Western Bushveld Complex, with some mining implications. In:

Anhaeusser, C.R. (Ed.). *Proc. XVth CMMI Congress Southern African Institute of Mining and Metallurgy Symposium Series* 14, **3**, 183 – 194.

Von Gruenewaldt, G., Sharpe, M.R., & Hatton, C.J. (1985). The Bushveld Complex: Introduction and Review. *Economic Geology,* **80**, 803 – 812.

Walraven, F. (1982). *Textural geochemical and genetical aspects of the granophyric rocks of the Bushveld Complex.* (Unpublished PhD Thesis). University of Pretoria, 251.

Walraven, F. (1987). Textural, geochemical and genetic aspects of the granophyric rocks of the Bushveld Complex. Memoir 72, *Geological Survey South Africa*, 145.

Walters, J.K., & Westerman, J.D. (1986). Multicomponent seismic studies using complex trace analysis. *Geophysics*. **51**(6), 1235 – 1251.

Widess, M.B. (1973). How thin is a thin bed? *Geophysics*, **38**(6), 1176 – 1180.

Yilmas, O. (2008). Seismic Data Analysis Processing, Inversion and Interpretation of Seismic data. U.S.A: *Society of Exploration Geophysicists*, 5 – 1801

Appendix A

R studio code

Statistical analysis

Author: Lebogang Sehoole

```
### Creating a histogram, boxplot and Normal Q-Q plot in order to determine if data are normal.

distancepotholes3 <- read_csv("distancepotholes3.csv", header = T)

##magic_result_as_dataframe()

summary(distancepotholes3)

X= hist(distancepotholes3$Distances, breaks = 12, main = "Histogram of the distances between different potholes from their centres",xlab = "Distance between the centre of the potholes (m)", col = "grey")

boxplot(distancepotholes3$Distances,main = "Boxplot of the distances between the potholes", ylab = "Distance between the centre of the potholes (m)", col = "grey")

shapiro.test(distancepotholes3$Distances) #(test for normality)

z=log(Datanew2$`Volume (m^3)`)

y=sqrt(x)#transform the data

hist(z, breaks = 12)

qqnorm(log(Datanew2$`Volume (m^3)`));qqline(log(Datanew2$`Volume (m^3)`))

shapiro.test(y)

skewness(distancepotholes3$Distances)

kurtosis(distancepotholes3$Distances)

summary(x)

y= hist(z,breaks = 10, main = "Histogram of the log of the volume of the potholes",xlab = "logarithmic volume of the potholes", col = "grey")

za= hist(Datanew2$`Volume (m^3)` ,breaks = 10, main = "Histogram  of the volume of the potholes",xlab = "volume of the potholes (m^3)", col = "grey")

shapiro.test(log(Datanew2$`Volume (m^3)`))

ggplot(Datanew2, aes(x= Datanew2$Y, y = Datanew2$X, size = Datanew2$`Volume (m^3)`, colors='paired'))+geom_point(alpha=1)+

  labs(size = "Diameter of potholes")+
```

```
  ylab("Depth from the UG-2 (m)")+
  theme_bw()+
  theme(panel.background = element_blank(),panel.grid = element_blank())
```

Appendix B

MATLAB code

Statistical analysis: Lebogang Sehoole

```
%***** Plotting a bubble graph from the loaded excel spreadsheet
filename = 'Datanew2.xlsx' ; % name of file that we reading from excel
A = xlsread(filename);
Diameter = A(:, 4);
Depth = A(:,6);
Area = A(:,7);
X= A(:,2);
Y= A(:,3);
Volume = A(:,8);
Log_Vol= log(Volume);
%c= linspace(1,10, length(Diameter));
%d= 5.*Diameter;
%if Diameter <= 80
      % B=  scatter(X,Y,Diameter,'b','filled');
       C = scatter(Diameter,Depth,200,'b','filled');
%end
      %elseif Diameter >= 100
        %  scatter(Area,Depth,Diameter,'g','filled')
    % else
         %scatter(Area,Depth,Diameter,'b','filled')
%colormap autumn;
%xlabel(' X (UTM)')
%ylabel('Y (UTM)')
```

Appendix C

MATLAB code

Nearest neighbour analysis

Author: Lebogang Sehoole

```
%***** finding the distances between different potholes
filename = 'Newpotholes2.xlsx' ; % name of file that we reading from excel
 A = xlsread(filename);
pothole = A(:,1);
x= A(:,2);
y= A(:,3);
% n=0;
% d=[];

% metr = [x,y];
% dist = pdist(metr);
% distance = dist';

for i=1:length(x)
   n=n+1;
   for j = 1:length(y)
   dnj=sqrt((x(n)-x(j)).^2+(y(n)-y(j)).^2);
   d= [d,dnj];
   end
end

for z = 2:45
   a = 1 + (z-1)*42;
```